



Universidade do Estado do Rio de Janeiro
Centro de Tecnologia e Ciências
Instituto de Física Armando Dias Tavares

Miguel Alves Gallo Pereira

**Study of lepton pair production by photon-photon fusion with
tagged protons with the CMS experiment**

Rio de Janeiro

2020

Miguel Alves Gallo Pereira

**Study of lepton pair production by photon-photon fusion with tagged
protons with the CMS experiment**



Dissertação apresentada, como requisito parcial para obtenção do título de Mestre, ao Programa de Pós-Graduação em Física, da Universidade do Estado do Rio de Janeiro.

Orientador: Prof. Dr. Antonio Vilela Pereira

Rio de Janeiro

2020

CATALOGAÇÃO NA FONTE
UERJ/ REDE SIRIUS / BIBLIOTECA CTC/D

P436 Pereira, Miguel Alves Gallo.
Study of lepton pair production by photon-photon fusion
with tagged protons with the CMS experiment / Miguel Alves
Gallo Pereira. - 2020.
91 f.: il.

Orientador: Antonio Vilela Pereira.
Dissertação (mestrado) - Universidade do Estado do
Rio de Janeiro, Instituto de Física Armando Dias Tavares.

1. Fusão nuclear - Teses. 2. Grande colisor de hádrons
(França e Suíça) - Teses. 3. Solenóide de múon compacto -
Teses. I. Pereira, Antonio Vilela. II. Universidade do Estado
do Rio de Janeiro. Instituto de Física Armando Dias Tavares.
III. Título.

CDU 539.12

Bibliotecária: Denise da Silva Gayer CRB7/5069

Autorizo, apenas para fins acadêmicos e científicos, a reprodução total ou
parcial desta dissertação, desde que citada a fonte.

Assinatura

Data

Miguel Alves Gallo Pereira

**Study of lepton pair production by photon-photon fusion with tagged
protons with the CMS experiment**

Dissertação apresentada, como requisito parcial para obtenção do título de Mestre, ao Programa de Pós-Graduação em Física, da Universidade do Estado do Rio de Janeiro.

Aprovada em 2 de Março de 2020.

Banca Examinadora:

Prof. Dr. Antonio Vilela Pereira (Orientador)
Instituto de Física Armando Dias Tavares – UERJ

Prof. Dr. Helena Brandão Malbouisson
Instituto de Física Armando Dias Tavares – UERJ

Profa. Dra. Irina Nasteva
Universidade Federal do Rio de Janeiro

Dr. Mauricio Thiel
Instituto de Física Armando Dias Tavares – UERJ

Prof. Dr. Murilo Santana Rangel
Universidade Federal do Rio de Janeiro

Rio de Janeiro

2020

ABSTRACT

PEREIRA, M. A. G. **Study of lepton pair production by photon-photon fusion with tagged protons with the CMS experiment.** 2020. 91 f. Dissertação (Mestrado em Física) – Instituto de Física Armando Dias Tavares, Universidade do Estado do Rio de Janeiro, Rio de Janeiro, 2020.

At the Large Hadron Collider (LHC), located at CERN (Geneva-Switzerland), proton beams collide at a center-of-mass energy of 13 TeV. There are four collision points where large experiments were built to study the products of these collisions. In this dissertation, we are going to focus only on the CMS (Compact Muon Solenoid) experiment. The PPS (Precision Proton Spectrometer) sub-detector system consists of a silicon tracking system to measure the position and direction of protons scattered at small angles, and a set of timing counters to measure their time of flight with high precision. One of the purposes of the PPS detector is to study central exclusive and semi-exclusive production in proton-proton collisions with high levels of pileup. These processes are characterized by the reaction $p + p \rightarrow p^{(*)} \oplus X \oplus p^{(*)}$, where \oplus represents rapidity gaps, X is the high-mass central system and $p^{(*)}$ the final state protons, which may dissociate into a low-mass state (p^*), for the semi-exclusive case. A study of the production of muon pair via photon fusion process using CMS data collected during 2017 is presented in this dissertation, with the purpose of reproducing the analysis of the article (CMS AND TOTEM COLLABORATIONS, 2018) with updated data and detector, studying and using the PPS detector information as the main tool to discriminate signal and background events and prepare the methodology that will be used in future analyses of measurements of high-mass states and searches for anomalous couplings and new physics.

Keywords: Photon fusion. PPS. CMS. LHC.

RESUMO

PEREIRA, M. A. G. **Study of lepton pair production by photon-photon fusion with tagged protons with the CMS experiment.** 2020. 91 f. Dissertação (Mestrado em Física) – Instituto de Física Armando Dias Tavares, Universidade do Estado do Rio de Janeiro, Rio de Janeiro, 2020.

No Grande Colisor de Hádrõs (LHC, sigla em inglês para *Large Hadron Collider*), localizado no CERN (Genebra-Suíça), feixes de prótons colidem a energia de centro de massa de 13 TeV. Existem quatro pontos de colisão, onde os grandes experimentos foram colocados para estudar o produto dessas colisões. Nesta dissertação, iremos focar apenas no experimento Solenoide Compacto de Múons (CMS, sigla em inglês para *Compact Muon Solenoid*). O subdetector Espectrômetro de Prótons de Precisão (PPS, sigla em inglês para *Precision Proton Spectrometer*), do CMS, consiste em um sistema de trajetografia de silício para medir a posição e direção de prótons espalhados em pequenos ângulos e contadores de tempo para medir seus tempos de voo com alta precisão. O PPS está localizado a cerca de 200 m do ponto de interação, numa região bastante frontal nos dois lados do CMS. Um dos propósitos do subdetector PPS é estudar as produções central exclusiva e semi-exclusiva em colisões com alto nível de empilhamento, incluindo a produção de pares de bósons W e Z por fusão de fótons. Tal processo é caracterizado pela reação $p + p \rightarrow p^{(*)} \oplus X \oplus p^{(*)}$, onde \oplus representa lacunas de rapidez, X é o sistema central e $p^{(*)}$ são os prótons de estado final, que podem dissociar em um estado de baixa massa (p^*), no caso semi-exclusivo. Nesta dissertação, é apresentado um estudo de produção de pares de múons via fusão de fótons para os dados do CMS coletados durante o ano de 2017, com o objetivo de reproduzir a análise do artigo (CMS AND TOTEM COLLABORATIONS, 2018) com dados e detector atualizados, estudar e utilizar a informação do PPS como principal ferramenta de discriminação entre eventos de sinal e ruído e preparar a metodologia, que será usada em análises futuras de medições de estados de alta massa e procura por acoplamentos anômalos e nova física.

Palavras-chave: Fusão de fótons. PPS. CMS. LHC.

LIST OF FIGURES

Figure 1	- Production of lepton pairs by $\gamma\gamma$ fusion.	14
Figure 2	- Correlation between $\xi(\ell^+\ell^-)$ and $\xi(\text{RP})$	21
Figure 3	- The LHC scheme.	23
Figure 4	- The luminosity delivered to CMS.	24
Figure 5	- The CMS schematic representation.	26
Figure 6	- The CMS particle reconstruction schematic representation.	27
Figure 7	- The CMS Tracking System layout.	28
Figure 8	- The CMS ECAL schematic representation.	29
Figure 9	- The CMS HCAL schematic representation.	30
Figure 10	- The CMS Muon system schematic representation.	32
Figure 11	- d_{xy} and d_z illustration.	35
Figure 12	- Layout of PPS in LHC sector 56.	37
Figure 13	- Layout of PPS silicon strip sensors.	38
Figure 14	- PPS silicon 3D pixel sensors.	39
Figure 15	- Residual distributions for the RP relative alignment procedure.	39
Figure 16	- Alignment procedure for physics fills.	41
Figure 17	- Track impact point distribution.	42
Figure 18	- Radiation damage evolution.	44
Figure 19	- Signal diagrams.	48
Figure 20	- Background diagrams.	50
Figure 21	- “Cutflow” of the muon selections.	54
Figure 22	- Muon pair kinematic distributions for data and MC.	57
Figure 23	- Fill 5864 instantaneous luminosity.	58
Figure 24	- Muon pair kinematic distributions for data and MC and different cross- crossing angles.	59
Figure 25	- Extra track multiplicity distribution for tracks selected in category 2.	62
Figure 26	- Extra track multiplicity distribution for tracks selected in category 3.	63
Figure 27	- Data and MC extra track distributions.	64
Figure 28	- Extra track reweighting correction factors.	65
Figure 29	- Resampling effect in the mixing of DY events and pileup protons.	66
Figure 30	- Proton ξ resolution.	67
Figure 31	- Muon pair ξ resolution.	68
Figure 32	- ξ_{RP} resolution.	69
Figure 33	- $\xi_{\ell^+\ell^-}$ resolution.	70
Figure 34	- $\xi_{\ell^+\ell^-}$ versus ξ_{RP} correlation (single-RP) in events with only one proton.	71

Figure 35 - $\xi_{\ell^+\ell^-}$ versus ξ_{RP} correlation (single-RP) when no selection is applied on the number of protons.	72
Figure 36 - $\xi_{\ell^+\ell^-}$ versus ξ_{RP} correlation (multi-RP).	73
Figure 37 - Muon pair kinematic distributions in signal region for data and MC, for protons detected in sector 45 (220F).	76
Figure 38 - Muon pair kinematic distributions in signal region for data and MC, for protons detected in sector 56 (220F).	77
Figure 39 - ξ distributions in signal region for single-RP protons, in events with a single proton detected.	78
Figure 40 - ξ distributions in signal region for single-RP protons, in events without restrictions on the number of protons.	79
Figure 41 - ξ distributions in signal region for multi-RP protons.	80
Figure 42 - Horizontal component of the scattering angle in signal region for multi-RP protons.	81
Figure 43 - Vertical component of the scattering angle in signal region for multi-RP protons.	82

LIST OF TABLES

Table 1	- The Standard Model particles and some properties.	13
Table 2	- LHC technical parameters.	24
Table 3	- Properties for the CMS muon subsystems.	31
Table 4	- List of signal samples.	49
Table 5	- List of background sample.	51
Table 6	- 2017 data samples used in the analysis.	52
Table 7	- Muon selection criteria list and number of events.	55
Table 8	- Contributions of different crossing angles.	56
Table 9	- Fiducial cuts.	75
Table 10	- Number of events in signal region for the single-RP case, in events with a single proton detected.	83
Table 11	- Number of events in signal region for the single-RP case, in events without restrictions on the number of protons.	84
Table 12	- Number of events in signal region for multi-RP.	85

CONTENTS

	INTRODUCTION	10
1	THE STANDARD MODEL AND CENTRAL EXCLUSIVE PRODUCTION	12
1.1	Standard Model of particle physics	12
1.1.1	<u>Elementary particles</u>	12
1.2	Proton-proton collision and Central (Semi)Exclusive Production	14
1.3	Review of selected measurements of photon-photon fusion	15
1.3.1	$\gamma\gamma \rightarrow W^+W^-$	15
1.3.2	$\gamma\gamma \rightarrow \mu^+\mu^-$	17
2	EXPERIMENTAL SETUP	22
2.1	The Large Hadron Collider	22
2.1.1	<u>LHC main experiments</u>	25
2.2	Compact Muon Solenoid	25
2.2.1	<u>Sub-detectors</u>	25
2.2.1.1	Tracking System	27
2.2.1.2	ECAL	28
2.2.1.3	HCAL	29
2.2.1.4	Muon System	29
2.2.2	<u>Trigger System</u>	30
2.2.3	<u>Physics event reconstruction</u>	33
2.2.3.1	Particle Flow	33
2.2.3.2	Muon reconstruction	34
2.3	Precision Proton Spectrometer	34
2.3.1	<u>Alignment procedure</u>	36
2.3.2	<u>Proton reconstruction</u>	40
2.3.2.1	Track reconstruction in the Roman Pots	40
2.3.2.2	LHC beam optics	44
2.3.2.3	Determination of ξ	45
3	DATASETS AND SIMULATED SAMPLES	46
3.1	Datasets	46
3.2	Simulated samples	47
3.2.1	<u>Event generators</u>	47
3.2.2	<u>The Detector simulation</u>	47
3.3	The signal and background processes	48
3.3.1	<u>The Signal</u>	48
3.3.2	<u>The Background</u>	48

4	DATA ANALYSIS	52
4.1	Trigger	52
4.2	Muons	53
4.3	Protons	53
4.4	Baseline Event Selection	54
4.5	Data and MC Comparison	56
4.5.1	<u>Crossing Angle</u>	56
4.5.2	<u>Pileup reweighting</u>	56
4.5.3	<u>Drell-Yan resampling</u>	60
4.6	Central (Semi)Exclusive Production	60
4.6.1	<u>Track Multiplicity</u>	60
4.6.2	<u>The fractional momentum loss of the scattered protons</u>	61
4.6.3	<u>Inefficiencies and scale factors</u>	65
4.6.4	<u>Distributions in signal region</u>	74
4.7	Results	74
	CONCLUSION	87
	REFERENCES	88

INTRODUCTION

*Nothing in life is to be feared, it
is only to be understood. Now is the time to
understand more, so that we may fear less.
Marie Curie*

The Large Hadron Collider (LHC) and its detectors are a remarkable technologic achievement for science, which were built in collaboration with more than 100 countries and thousands of scientists. With the center-of-mass energy (\sqrt{s}) of about 13 TeV that LHC can reach, it is possible to verify aspects of the Standard Model — the theory that describes the elementary particles and interactions — and to formulate new theories beyond that. The ATLAS and CMS experiments at the LHC have notably discovered a new particle consistent with the Standard Model Higgs Boson (ATLAS COLLABORATION, 2012); (CMS COLLABORATION, 2012).

The Compact Muon Solenoid (CMS) is a general-purpose detector, built around a huge solenoid magnet at the LHC interaction point 5 (IP5). This takes the form of a cylindrical coil of superconducting cable that generates a magnetic field of 4 Tesla. The complete detector is 21 m long, 15 m wide and 15 m high. The main CMS subsystems are: the muon chambers, with their high precision characterization of muons, the electronic and hadronic calorimeters, that allows seeing a large range of particles and the tracking system, that combined with a high magnetic field, performs an accurate momentum measurement.

To add precision proton tracking and timing detectors in the very forward region on both sides of CMS, the Precision Proton Spectrometer (PPS) sub-detector was built and started to collect data in 2016. It is composed of three Roman Pots on each side of the central detector which allows the insertion of sensors close to the beam, allowing the measurement with high precision of protons scattered at very small angles. The LHC, CMS and the PPS system are discussed in more detail in chapter 2.

The PPS detector has brought the capability of investigating processes like Central Exclusive Production (CEP), where the protons remain intact after the collision and produce a central final system, X . The correlation of the information of the protons and X information is the main discriminator between exclusive events and the inclusive ones. More details on the Standard Model and CEP are presented in chapter 1.

In this dissertation, we consider the case where X consists of a muon pair ($\mu^+\mu^-$), coming from $\gamma\gamma$ fusion. Using the paper (CMS AND TOTEM COLLABORATIONS, 2018) as the main reference, we reproduced the presented analysis with updated data.

The CMS 2017 data were analyzed. Signal and background Monte Carlo samples were simulated as explained in chapter 3. The methodology applied to this analysis and the results are presented in chapter 4. In chapter 5, the conclusion and perspectives for

this and future analyses using a similar methodology are presented.

1 THE STANDARD MODEL AND CENTRAL EXCLUSIVE PRODUCTION

1.1 Standard Model of particle physics

The fundamental particle properties that we know currently are mostly explained by the Standard Model. The Standard Model is a relativistic quantum field theory that gathers the fundamental particles interactions (except for gravity), that are:

- **Strong Interaction:** Responsible for binding the protons and neutrons constituents - the quarks - and for keeping the nucleons bonded. Mediated by the gluons, acts at very short distances and is described by the Quantum Chromodynamics Theory (QCD) (HALZEN; MARTIN, 1984).
- **Weak Interaction:** Responsible for the neutron decay to proton by beta-decay. Mediated by the W^\pm e Z^0 bosons, also acts at very short distances and is described by the Electroweak Theory (SALAM, 1968).
- **Electromagnetic Interaction:** Responsible for the electron and nuclei attraction. Mediated by the photon, acts at infinite distances and is described by the Quantum Electrodynamics Theory (QED) (GREINER; REINHARDT, 2008).

1.1.1 Elementary particles

We can classify all particles into two groups: fermions and bosons. Fermions have half-integer spin, while bosons have integer spin.

The theories cited above describe the interactions between elementary particles that are classified into quarks, leptons — both are fermions and the constituents of the matter — and the gauge bosons, which mediate the interactions.

These elementary particles are summarized in Table 1.

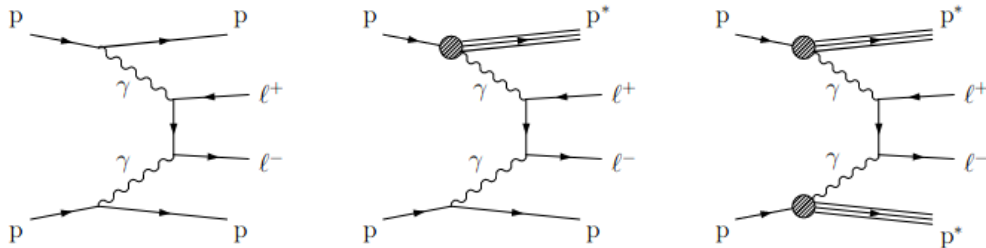
The Standard Model Higgs boson explains the generation of some Standard Model particle masses. A particle consistent with the Higgs boson has been discovered by the ATLAS and CMS experiments at the LHC (ATLAS COLLABORATION, 2012); (CMS COLLABORATION, 2012).

Table 1 - The Standard Model particles and some properties.

Particle	Mass (GeV/c²)	Charge (e)	Spin
Leptons			
<i>e</i>	5.11×10^{-4}	-1	1/2
ν_e	$< 1.1 \times 10^{-9}$	0	1/2
μ	0.106	-1	1/2
ν_μ	$< 1.1 \times 10^{-9}$	0	1/2
τ	1.777	-1	1/2
ν_τ	$< 1.1 \times 10^{-9}$	0	1/2
Quarks			
<i>u</i>	2.2×10^{-3}	+2/3	1/2
<i>d</i>	4.7×10^{-3}	-1/3	1/2
<i>s</i>	95.0×10^{-3}	-1/3	1/2
<i>c</i>	1.275	+2/3	1/2
<i>b</i>	4.18	-1/3	1/2
<i>t</i>	172.9	+2/3	1/2
Gauge Bosons			
γ	0	0	1
<i>Z</i>	91.188	0	1
W^\pm	80.379	± 1	1
<i>g</i>	0	0	1
Scalar Bosons			
<i>H</i>	125.10	0	0

Legend: The Standard Model particles and their respective mass, charge and spin. The values were extracted from (TANABASHI et al., 2018). For the neutrinos, upper limit was extracted from (AKER et al., 2019).

Source: The author, 2020.

Figure 1 - Production of lepton pairs by $\gamma\gamma$ fusion.

Legend: The exclusive (left), single proton dissociation or semi-exclusive (middle), and double proton dissociation (right) topologies are shown. The left and middle processes result in at least one intact final-state proton, and are considered signal in this analysis. The rightmost diagram is considered to be a background process.

Source: CMS AND TOTEM COLLABORATIONS, 2018, p.1.

1.2 Proton-proton collision and Central (Semi)Exclusive Production

The LHC accelerates protons with $\sqrt{s} = 13$ TeV and collides them at the location of the experiments, also called interaction points (IP). A collision consists of the interaction of two bunch of protons.

In some of these collisions, both protons remain intact after losing a fraction of their energy. This process is called central exclusive production (CEP).

For this dissertation, the case where only one proton survives is equally important, called central semi-exclusive production. The other proton that does not survive, dissociates into a low-mass state. That process can also be called single dissociation.

The processes where at least one proton survives are considered signal events, while the process where the two protons do not survive, called double dissociation, is considered background for this analysis (Figure 1).

The use of central (semi)exclusive production, with the muon pair as the central final system, is interesting because it is a clean channel, easy to discriminate signal events from background ones and helps in the PPS validation. Also, it has a well-known theoretical cross section, so any deviation from this value may be an indication of new physics.

The fractional momentum loss of the proton (ξ_p) is defined by,

$$\xi_p = 1 - \frac{|\mathbf{p}'|}{|\mathbf{p}|}, \quad (1)$$

where \mathbf{p} (\mathbf{p}') denotes the four-momentum of the proton before (after) the collision.

For each event, the value of the fractional momentum loss of the scattered proton can be estimated from the kinematics of the centrally produced lepton pair, obtained with the CMS detector. The fractional momentum loss of the central system ($\xi_{\ell^+\ell^-}$) is defined by,

$$\xi_{\ell^+\ell^-} = \frac{1}{\sqrt{s}} [p_T(\ell^+)e^{\pm\eta(\ell^+)} + p_T(\ell^-)e^{\pm\eta(\ell^-)}], \quad (2)$$

where p_T and η denote the lepton transverse momentum and pseudorapidity, respectively.

The transverse momentum p_T is given by the magnitude of the momentum parallel to the z-axis — plane transverse to the beam direction. Basically, it is the magnitude of the momentum components pointing along the x and y axes:

$$p_T = \sqrt{p_x^2 + p_y^2}. \quad (3)$$

The rapidity y is given by,

$$y = \frac{1}{2} \ln \left(\frac{E + p_z}{E - p_z} \right). \quad (4)$$

For massless particles, y is reduced to pseudorapidity η , that is given by,

$$\eta = -\ln \left(\tan \frac{\theta}{2} \right). \quad (5)$$

Equation 2 is exact for exclusive events and it is a good approximation for semi-exclusive ones.

The comparison of this indirect measurement of ξ with the direct one obtained with the PPS sub-detector can be used to suppress background events.

1.3 Review of selected measurements of photon-photon fusion

In the following, we review previous measurements of photon-photon fusion processes in different final states, that we consider relevant for the present analysis.

1.3.1 $\gamma\gamma \rightarrow W^+W^-$

- **Evidence for exclusive $\gamma\gamma \rightarrow W^+W^-$ production and constraints on anomalous quartic gauge couplings in pp collisions at $\sqrt{s} = 7$ and 8 TeV (CMS COLLABORATION, 2016).**

A search for (semi)exclusive $\gamma\gamma \rightarrow W^+W^-$ production, via $p+p \rightarrow p^{(*)}W^+W^-p^{(*)} \rightarrow p^{(*)}\mu^\pm e^\mp p^{(*)}$ at $\sqrt{s} = 7$ TeV with an integrated luminosity of 19.7 fb^{-1} . Events are selected by requiring the presence of an electron-muon pair with transverse momentum $p_T(\mu^\pm e^\mp) > 30 \text{ GeV}/c$, and no associated charged particles detected from the same vertex.

The $W^+W^- \rightarrow \mu^\pm e^\mp$ (plus undetected neutrinos) channel is the final state used to search for a signal, as the backgrounds due to Drell–Yan (DY) — lepton pair production by quark-antiquark annihilation, via a virtual Z/γ decay — and $\gamma\gamma \rightarrow \ell^+\ell^-$ production are smaller than in the same-flavor final states. Events in which one or both of the W bosons decay into a tau lepton, with a subsequent decay of the tau to a muon or electron and neutrinos, are also included in the signal.

Control samples of $\gamma\gamma \rightarrow \mu^+\mu^-$ and $\gamma\gamma \rightarrow e^+e^-$ events are used to study the efficiency and the “rescattering” corrections, from additional parton interactions between the protons. Control regions in the lepton pair p_T and charged-particle multiplicity distributions are used to study the main background contributions to the signal. Finally the $p_T(\mu^\pm e^\mp)$ distribution is used as the discriminating variable to measure the standard model $\gamma\gamma \rightarrow W^+W^-$ cross section, and to search for evidence of anomalous quartic gauge couplings (AQGC) (TELES, 2013).

The background due to DY $\tau^+\tau^-$ production is heavily suppressed by the requirement of no additional tracks associated with the $\mu^\pm e^\mp$ vertex. The requirement that $p_T(\mu^\pm e^\mp) > 30 \text{ GeV}/c$ combined with the $20 \text{ GeV}/c$ single-lepton thresholds, reduces the $\gamma\gamma \rightarrow \tau^+\tau^-$ background to approximately one event in the signal region.

The 8 TeV results are combined with the previous 7 TeV results (obtained for 5.05 fb^{-1} of data). In the signal region, 13 (2) events are observed over an expected background of 3.9 ± 0.6 (0.84 ± 0.15) events for 8 (7) TeV, resulting in a combined excess of 3.4 over the background-only hypothesis. The results are compatible with the Standard Model prediction for (semi)exclusive $\gamma\gamma \rightarrow W^+W^-$ production. Upper limits on the anomalous quartic gauge coupling operators $a_{0,C}^W$ (dimension-6) and $f_{M0,1,2,3}$ (dimension-8), are derived from the measured lepton pair transverse momentum spectrum.

- **Measurement of exclusive $\gamma\gamma \rightarrow W^+W^-$ production and search for exclusive Higgs boson production in pp collisions at $\sqrt{s} = 8$ TeV using the ATLAS detector** (ATLAS COLLABORATION, 2016).

A search for exclusively produced W boson pairs in the process $pp(\gamma\gamma) \rightarrow pW^+W^-p$ and exclusively produced Higgs boson in the process $pp(gg) \rightarrow pHp$ have been performed using $e^\pm\mu^\mp$ final states. These measurements use 20.2 fb^{-1} of pp collisions collected by the ATLAS experiment at $\sqrt{s} = 8$ TeV at the LHC in 2012.

Electrons are required to have $p_T > 10$ GeV/c, and be within $|\eta| < 2.47$, excluding the region $1.37 \leq |\eta| \leq 1.52$. Also, they satisfy certain shower shape and track selection criteria. Electrons are required to be isolated based on tracking and calorimeter information.

Jets with $|\eta| < 4.5$ are reconstructed from energy clusters in the calorimeter using the anti-kt algorithm with a radius parameter of 0.4. To suppress jets from pileup — number of protons coming from different interactions in the same bunch crossing —, only jets with $p_T > 25$ GeV/c are considered. Charged particle tracks having $p_T > 0.4$ GeV/c and $|\eta| < 2.5$ reconstructed by the inner detector are used to reject nonexclusive production. They are required to leave at least one hit in the pixel detector and at least four hits in the silicon microstrip detector.

The full phase space cross-section predicted by Herwig++ (BAHR et al., 2008) is $\sigma_{\gamma\gamma \rightarrow W^+W^-}^{\text{Herwig++}} = 41.6$ fb. The branching ratio of the W^+W^- pair decaying to $e^\pm\mu^\mp X$ is $\text{BR}(W^+W^- \rightarrow e^\pm\mu^\mp X) = 3.23\%$ (including the leptonic decays of τ leptons). Therefore, the predicted cross-section corrected for $\text{BR}(W^+W^- \rightarrow e^\pm\mu^\mp X)$ and including the dissociative contributions through the normalization $f_\gamma = 3.30 \pm 0.23$ becomes:

$$\sigma_{\gamma\gamma \rightarrow W^+W^- \rightarrow e^\pm\mu^\mp X}^{\text{Predicted}} = f_\gamma \cdot \sigma_{\gamma\gamma \rightarrow W^+W^-}^{\text{Herwig++}} \cdot \text{BR}(W^+W^- \rightarrow e^\pm\mu^\mp X) = 4.4 \pm 0.4 \text{ fb.}$$

The measured cross-section is determined in the exclusive W^+W^- region and extrapolated to the full $W^+W^- \rightarrow e^\pm\mu^\mp + X$ phase space:

$$\sigma_{\gamma\gamma \rightarrow W^+W^- \rightarrow e^\pm\mu^\mp X}^{\text{Measured}} = (N_{\text{Data}} - N_{\text{Background}})/(L\epsilon A) = 6.9 \pm 2.2(\text{stat.}) \pm 1.4(\text{sys.}) \text{ fb,}$$

where $L = 20.2 \pm 0.4 \text{ fb}^{-1}$.

Exclusive production of W^+W^- consistent with the Standard Model prediction is found with 3.0σ significance. Limits on anomalous quartic gauge couplings are set at 95% confidence-level as $-1.7106 < a_0^W/\Lambda^2 < 1.7 \times 10^{-6} \text{ GeV}^{-2}$ and $-6.4 \times 10^{-6} < a_C^W/\Lambda^2 < 6.3 \times 10^{-6} \text{ GeV}^{-2}$. A 95% confidence-level upper limit on the total production cross-section for exclusive Higgs boson is set to 1.2 pb.

1.3.2 $\gamma\gamma \rightarrow \mu^+\mu^-$

- **Exclusive $\gamma\gamma \rightarrow \mu^+\mu^-$ production in proton-proton collisions at $\sqrt{s} = 7$ TeV.** (CMS COLLABORATION, 2012).

A measurement of the exclusive photon-photon production of muon pairs in proton-proton collisions at $\sqrt{s} = 7$ TeV, $pp \rightarrow p\mu^+\mu^-p$, is reported using data collected during 2010 at the LHC, corresponding to an integrated luminosity of 40 pb^{-1} .

Events are selected online by triggers requiring the presence of two reconstructed

muons with a minimum p_T of 3 GeV/c. No requirement on the charge of the muons is applied at the trigger level. Muons are reconstructed offline by combining information from the muon system with that on charged-particle tracks reconstructed in the silicon tracker, and events with a pair of oppositely charged muons are selected. The exclusivity selection is performed to keep only events with a vertex having no tracks other than those from the two muons. Finally, the signal muons are required to satisfy identification criteria, and kinematic constraints are imposed using their four-momentum.

The trigger, tracking, and offline muon selection efficiencies are each obtained from the tag-and-probe method by using samples of inclusive $J/\psi \rightarrow \mu^+\mu^-$ and $Z \rightarrow \mu^+\mu^-$ events from data and Monte Carlo simulation. These control samples are triggered on one muon such that the other muon is unbiased with respect to the efficiency to be measured.

For muon pairs with invariant mass greater than 11.5 GeV/c², $p_T(\mu) > 4$ GeV/c, and $|\eta(\mu)| < 2.1$, 148 events pass all selections. Approximately half of these are ascribed to fully exclusive production. The number of events expected from Monte Carlo simulation of signal, proton dissociation, and DY backgrounds for an integrated luminosity of 40 fb⁻¹ is 184.

A fit to the muon pair $p_T(\mu^+\mu^-)$ distribution results in a measured cross section of $\sigma(pp \rightarrow p\mu^+\mu^-p) = 3.38_{-0.55}^{+0.58}(\text{stat.}) \pm 0.16(\text{syst.}) \pm 0.14(\text{lumi.})$ pb, consistent with the theoretical prediction evaluated with the event generator LPAIR (BARANOV et al., 1991). The ratio to the predicted cross section is $0.83_{-0.13}^{+0.14}(\text{stat.}) \pm 0.04(\text{syst.}) \pm 0.03(\text{lumi.})$, where the statistical uncertainties are strongly correlated with the single-proton dissociation background. The characteristic distributions of the muon pairs produced via $\gamma\gamma$ fusion, such as the muon acoplanarity, the muon pair invariant mass and transverse momentum agree with those from the theory. Acoplanarity stands for $a = 1 - |\Delta\phi(\mu^+\mu^-)|/\pi$, where ϕ is the azimuthal angle in respect to the beam line.

- **Measurement of the exclusive $\gamma\gamma \rightarrow \mu^+\mu^-$ process in proton–proton collisions at $\sqrt{s} = 13$ TeV with the ATLAS detector.** (ATLAS COLLABORATION, 2018).

The production of exclusive $\gamma\gamma \rightarrow \mu^+\mu^-$ events in proton–proton collisions at $\sqrt{s} = 13$ TeV is measured with the ATLAS detector at the LHC, using data collected during 2015 at the LHC and corresponding to an integrated luminosity of 3.2 fb⁻¹.

Events were selected online by a set of muon pair triggers with a muon p_T threshold of 6 GeV/c or 10 GeV, and muon pair invariant mass $10 < m_{\mu^+\mu^-} < 30$ GeV/c² or $m_{\mu^+\mu^-} < 30$ GeV/c², respectively. Triggers with the lower transverse momentum requirement were enabled for data-taking with an instantaneous luminosity below

$1.2 \times 10^{34} \text{ cm}^{-2}\text{s}^{-1}$. These triggers were designed to select exclusive muon pair events by employing an additional selection on the transverse momentum of the muon pair system, $p_T^{\mu^+\mu^-} < 2 \text{ GeV}/c$, to reduce contributions from DY and multijet production.

Events are required to have exactly one pair of oppositely-charged muons. The muon pair invariant mass is required to be between $12 < m_{\mu^+\mu^-} < 70 \text{ GeV}/c^2$ with different p_T^μ conditions. Each of the two muons must be matched to one of the muons reconstructed by the trigger.

After these selection requirements, 2.9×10^6 muon pair candidates are found in the data.

The background to the exclusive signal includes mainly contributions from single dissociation and double dissociation $\gamma\gamma \rightarrow \mu^+\mu^-$ production.

The systematic uncertainties are related to: muon-related sources, vertex isolation efficiency, pileup description, background, template shape, LHC beam effects, unfolding method, luminosity and other cross-checks.

The integrated cross-section is determined within a fiducial acceptance region of the ATLAS detector and differential cross-sections are measured as a function of the muon pair invariant mass. The results are compared to theoretical predictions both with and without corrections for absorptive effects. The fiducial cross-section is measured to be $\sigma_{\gamma\gamma \rightarrow \mu^+\mu^-}^{excl.fid.} = 3.12 \pm 0.07(\text{stat.}) \pm 0.14(\text{syst.}) \text{ pb}$. This value can be compared to the bare EPA predictions from Herwig, $\sigma_{\gamma\gamma \rightarrow \mu^+\mu^-}^{EPA} = 3.56 \pm 0.05 \text{ pb}$, to the EPA predictions corrected for absorptive effects using the finite-size parameterisation, $\sigma_{\gamma\gamma \rightarrow \mu^+\mu^-}^{EPA,corr.} = 3.06 \pm 0.05 \text{ pb}$, or to the SuperChic2 predictions, $\sigma_{\gamma\gamma \rightarrow \mu^+\mu^-}^{SC2} = 3.45 \pm 0.05 \text{ pb}$.

- **Observation of proton-tagged, central (semi)exclusive production of high-mass lepton pairs in pp collisions at 13 TeV with the CMS–TOTEM precision proton spectrometer.** CMS AND TOTEM COLLABORATIONS.

The PPS data analyzed here were collected during the period May–September 2016, corresponding to an integrated luminosity of 9.4 fb^{-1} . In the same period, CMS collected a total of 15.6 fb^{-1} . For the present data, the full crossing angle of the beams — i.e. twice the *half* beam crossing angle — was $370 \mu\text{rad}$. The crossing angle is the angle between two opposite colliding beams.

The online selection required at least two muon (electron) candidates of any charge, each with transverse momentum $p_T > 38(33) \text{ GeV}/c$. No requirement on forward protons was imposed online.

Offline, the tracks of the two highest- p_T lepton candidates of the same flavor in the event are fitted to a common vertex. The vertex position from the fit is required

to be consistent with that of a collision ($|z| < 15$ cm), with $\chi^2 < 10$. The lepton candidates are further required to have $p_T > 50$ GeV/ c , and to pass the standard CMS quality criteria. In the final stage of the analysis only leptons with opposite charge are required. The event is accepted if no additional tracks are found in the region within the veto distance around the lepton pair vertex.

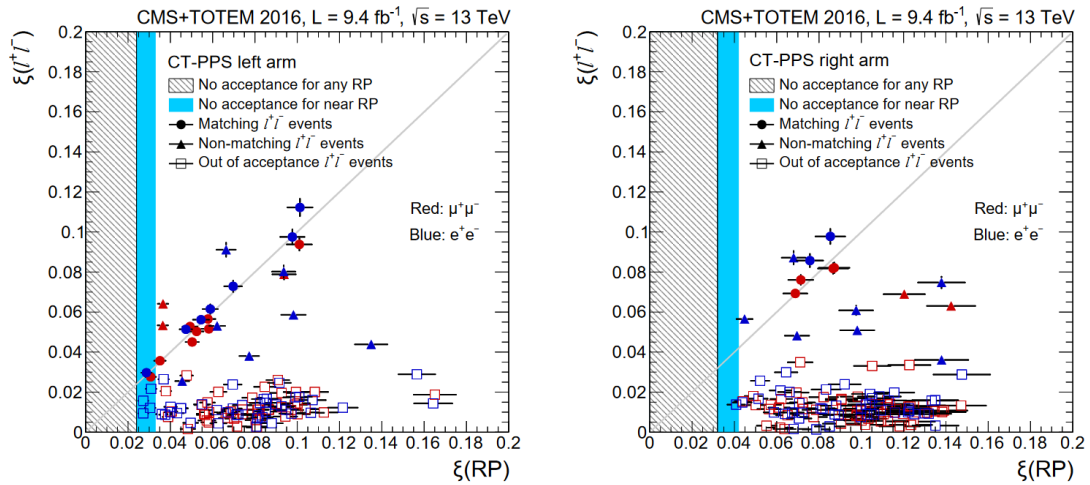
In addition, the lepton pair acoplanarity — $a = 1 - |\Delta\phi(\ell^+\ell^-)|/\pi$ — is required to be consistent with the two leptons being back-to-back in azimuth ϕ . An extra-track veto region distance of at least 0.5 mm around the vertex is required, along with $a < 0.009$ for the muons and $a < 0.006$ for the electrons. The acoplanarity requirements are chosen such that the signal to background ratio predicted by the simulation is above 1 before any matching of the leptons with RP tracks. Because of the high pileup rate, the selection is based on information from reconstructed tracks alone, without using information from the calorimeters. This results in an efficiency of $> 95\%$ for the highest values of pileup and pileup density observed in the 2016 dataset used for the measurement.

Finally, the invariant mass of the leptons is required to be $m(\ell^+\ell^-) > 110$ GeV/ c^2 . This suppresses the region around the Z boson mass, which is expected to be dominated by Drell–Yan production.

After all selection criteria discussed above, the backgrounds are expected to arise mainly from prompt $\ell^+\ell^-$ production combined with proton tracks from unrelated pileup interactions or beam backgrounds in the same bunch crossing. The largest background sources of $\ell^+\ell^-$ production are the Drell–Yan process and double proton dissociation. To estimate both backgrounds, samples of RP tracks from $Z \rightarrow \mu^+\mu^-$ and $Z \rightarrow e^+e^-$ events in data are used.

In the $\mu^+\mu^-$ channel, a total of 17 events are observed with $\xi(\mu^+\mu^-)$ within the CT–PPS acceptance, and at least one track detected in the relevant RPs. Five of those events have a mismatch of $\geq 2\sigma$ between the muon pair and the proton kinematics, compared to 11.0 ± 4.0 (stat+syst) such events expected from background; twelve events have a track in at least one of the two RPs matching $\xi(\mu^+\mu^-)$ within 2σ . The significance of observing 12 events over the background estimate of 1.49 ± 0.07 (stat) ± 0.53 (syst) is 5σ . The invariant masses and rapidities of the $\mu^+\mu^-$ candidate events are consistent with the expected single-arm acceptance, given the LHC optics and the position of the RPs. No events are observed with matching protons in both arms. The correlation distributions are shown in Figure 2.

For 11 candidate muon pair events out of the 12, the vertical component of the scattering angle is compatible with zero within at most 2.5σ , where σ is the width of the vertical component of the scattering angle. For one event, the discrepancy is 3.5σ , in agreement with the background estimate.

Figure 2 - Correlation between $\xi(\ell^+\ell^-)$ and $\xi(\text{RP})$.

Legend: Correlation between the fractional values of the proton momentum loss measured in the central lepton pair system, $\xi(\ell^+\ell^-)$, and in the RPs, $\xi(\text{RP})$, for both RPs in each arm combined. The 45 sections (left) and 56 (right) are shown.

Source: CMS AND TOTEM COLLABORATIONS, 2018, p.17.

This result constitutes the first observation of proton-tagged photon-photon collisions at the electroweak scale. This measurement also demonstrates that CT-PPS performs according to the design specifications.

2 EXPERIMENTAL SETUP

To study central (semi)exclusive production, a dataset from proton-proton collisions at $\sqrt{s} = 13$ TeV, taken in 2017 by the CMS experiment was used. Protons scattered at small angles were measured by the Precision Proton Spectrometer (PPS) detector system. This chapter presents an introduction about CMS and PPS, a more detailed description can be found in (CMS COLLABORATION, 2008) and (CMS AND TOTEM COLLABORATIONS, 2014), respectively.

2.1 The Large Hadron Collider

The European Organization for Nuclear Research (CERN) is an international laboratory at the forefront of experimental particle physics research. Its experiments depend on the existence of powerful accelerators.

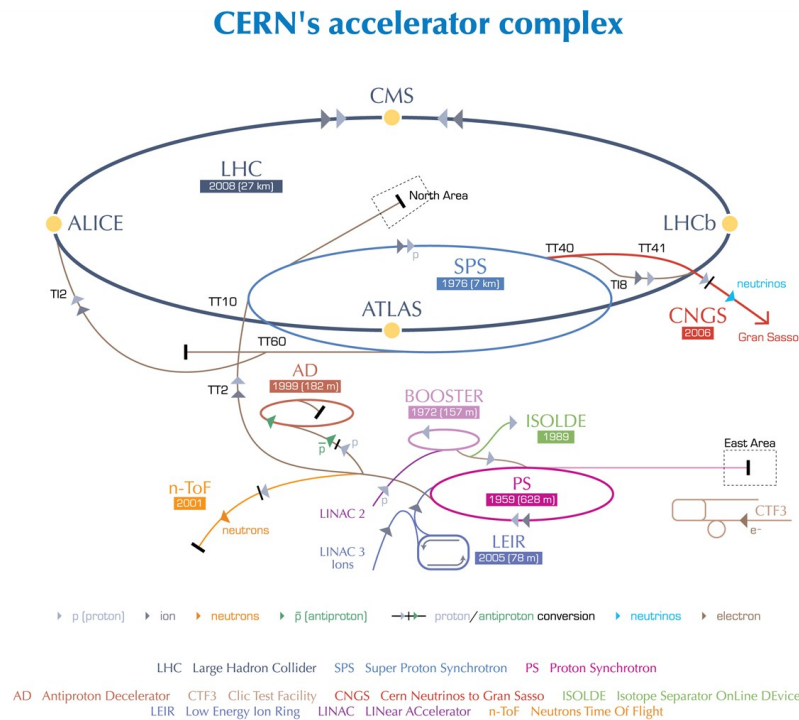
The LHC is the largest and most powerful particle collider in the world and consists of a 27 km long circular accelerator (Figure 3), which is 100 m below ground, located at the French-Swiss border near Geneva. It consists of superconducting magnets to accelerate particles to very high energies.

Before entering the LHC, the protons pass through a set of accelerator stages. The protons come from the ionization of hydrogen atoms. At LINAC2 these protons are accelerated until the energy of 50 MeV with radio frequency quadrupoles (RFQ). The next stage is the Proton Synchrotron Booster (PSB), where there are a set of four synchrotron rings that raise the proton energy to 1.4 GeV. After the PSB, the protons are introduced into a synchrotron with a circumference of 600 m, the Proton Synchrotron (PS), where the energy increases to 25 GeV. The last stage before LHC is the Super Proton Synchrotron (SPS), where the protons are accelerated up to 450 GeV.

Inside the accelerator, two beams of highly energetic particles travel at speeds close to light before colliding. Collisions between beams of protons are studied at center-of-mass energies of up to 13 TeV. The beams travel in opposite directions on separate beam vacuum tubes with the protons separated in up to $N_b = 2808$ bunches with $n_b = 1.15 \times 10^{11}$ protons. Each bunch is separated from the next one by 25 ns. A bunch of one beam collides with a bunch of the other with frequency (f_c) of 40 MHz.

Taking into account the number of protons per bunch (n_b), it means around 1 billion of proton interactions per second. The number of protons coming from different interactions in the same bunch crossing is called pileup. It results in an instantaneous luminosity of $10^{34} \text{ cm}^{-2}\text{s}^{-1}$. The numbers mentioned here are the nominal ones. Because of the many technological challenges, the accelerator could not operate with exactly these

Figure 3 - The LHC scheme.



European Organization for Nuclear Research | Organisation européenne pour la recherche nucléaire

© CERN 2008

Legend: The CERN accelerator and detector complex.

Source: LEFÈVRE, 2008.

parameters. In Table 2, these values are shown for the nominal and 2017 cases, the year of interest for this dissertation.

The proton beams are guided around the ring by the strong field generated by the superconducting electromagnets. To reach such a state of superconductivity, a complex system of magnets that include 1232 dipoles must be cooled to a temperature of 1.85 K to reach a magnetic field of 8.33 T. A set of magnet quadrupoles are used for beam focusing and squeezing.

The first collision in the LHC was in November 2009 with a 900 GeV center-of-mass energy. At the end of the same year, the LHC was colliding protons at an energy of 2.36 TeV and in 2010 started the data taking period called Run I (2010-2012), with 7 TeV center-of-mass energy for proton-proton collisions. After the shutdown in 2013 and 2014, the LHC started another data taking period, called Run II (2015-2018). In the entire period, the proton-proton collisions were performed at 13 TeV. Figure 4 shows the integrated luminosity delivered by the LHC, from 2010 to July 2018, and the CMS recorded luminosity in the 2017 data taking period.

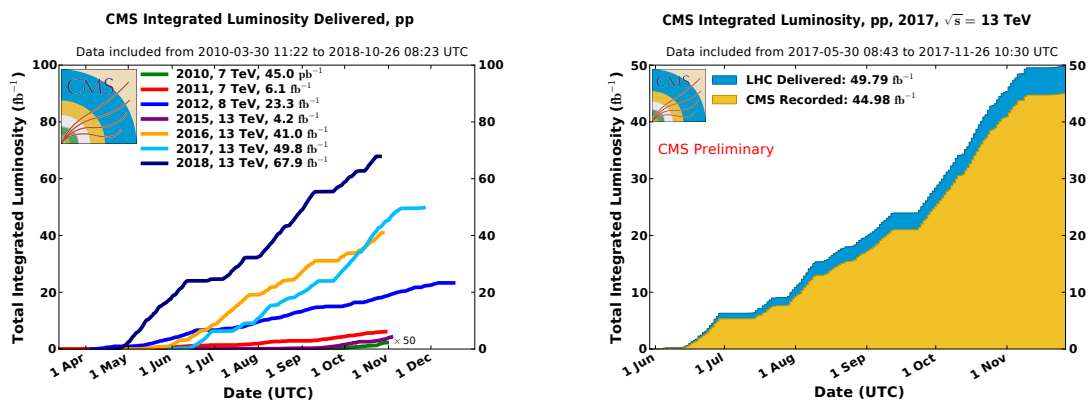
Table 2 - LHC technical parameters.

	Nominal	2017
Center-of-mass energy (TeV)	14	13
Maximum \mathcal{L}_{inst} ($\text{cm}^{-2}\text{s}^{-1}$)	1×10^{34}	2.09×10^{34}
f_c (MHz)	40	40
Maximum n_b	1.15×10^{11}	1.25×10^{11}
Maximum N_b	2808	2556
Bunch spacing (ns)	25	25

Legend: Technical parameters for proton-proton collisions for nominal and 2017 conditions.

Source: The author, 2020.

Figure 4 - The luminosity delivered to CMS.



Legend: The integrated luminosity delivered to CMS by the LHC from 2010 to 2018 (left) and the comparison between the delivered and recorded luminosity for 2017 (right).

Source: CMS COLLABORATION, 2019.

2.1.1 LHC main experiments

The LHC collides particles in interaction points (IP), where the four detectors are located. They detect particles produced in the collisions using different kinds of technologies. The experiments are: A Large Ion Collider Experiment (ALICE) (ALICE COLLABORATION, 2008), A Toroidal LHC ApparatuS (ATLAS) (ATLAS COLLABORATION, 2008), **Compact Muon Solenoid (CMS)** (CMS COLLABORATION, 2008) and LHC-beauty (LHCb) (LHCb COLLABORATION, 2008).

2.2 **Compact Muon Solenoid**

The CMS detector is built around a 13 m long, 5.9 m inner diameter, with a superconducting solenoid that offers a magnetic field of 3.8 T. This takes the form of a cylindrical detector coaxial with the LHC beam direction distributed in a length of 21.5 m and a diameter of 15 m. The total weight of the CMS experiment is approximately 14 kton. It can be divided between the barrel and the endcap region. The general structure of the CMS experiment is shown in Figure 5.

The CMS coordinate system has the z-axis pointing in the direction of the beam, the y-axis in the upward direction and the x-axis points towards the center of the LHC circumference. Because of the geometry of the detector, cylindrical coordinate system is mostly used. The azimuthal angle ϕ is defined from the x-y plane, while the polar angle θ is defined from the z-axis.

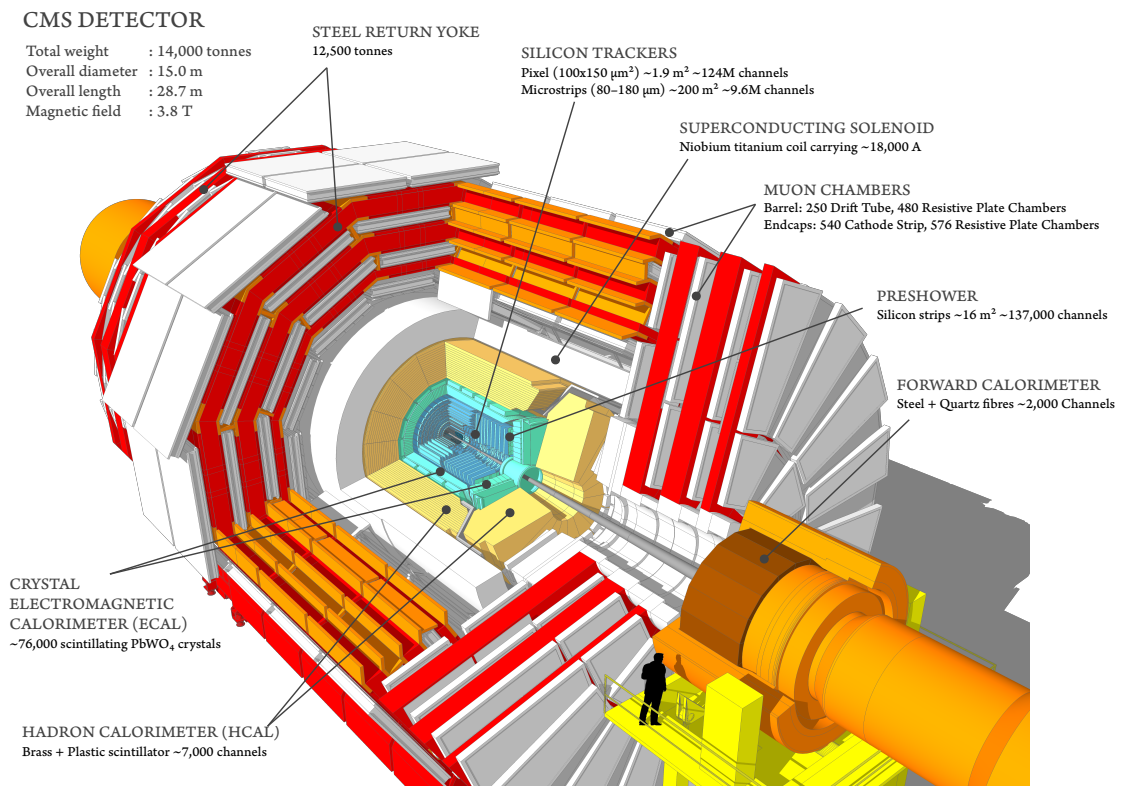
2.2.1 Sub-detectors

The CMS detector comprises several sub-detectors that are specialized in the study and reconstruction of certain physics objects. Figure 6 shows the representation of a slice of the CMS sub-detectors.

The sub-detectors are: the Tracking System, the Electromagnetic Calorimeter (ECAL), the Hadronic Calorimeter (HCAL) and the Muon System.

Furthermore, a new sub-detector started to collect data in 2016, the Precision Proton Spectrometer (PPS). It is situated around 210 m from the CMS IP, close to the beam, in both sides of the central detector, built to detect protons scattered with small angles in the IP.

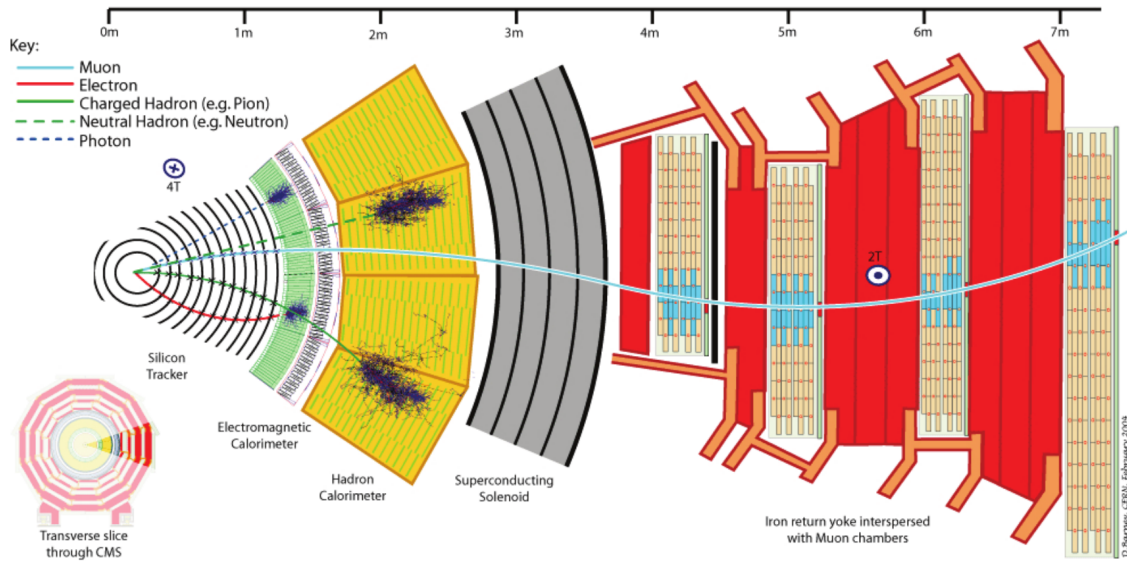
Figure 5 - The CMS schematic representation.



Legend: Illustration of the CMS detector.

Source: SAKUMA, 2019.

Figure 6 - The CMS particle reconstruction schematic representation.



Legend: A representation of a slice of the CMS sub-detectors and the reconstructed particles trajectories.

Source: DAVIS, 2016.

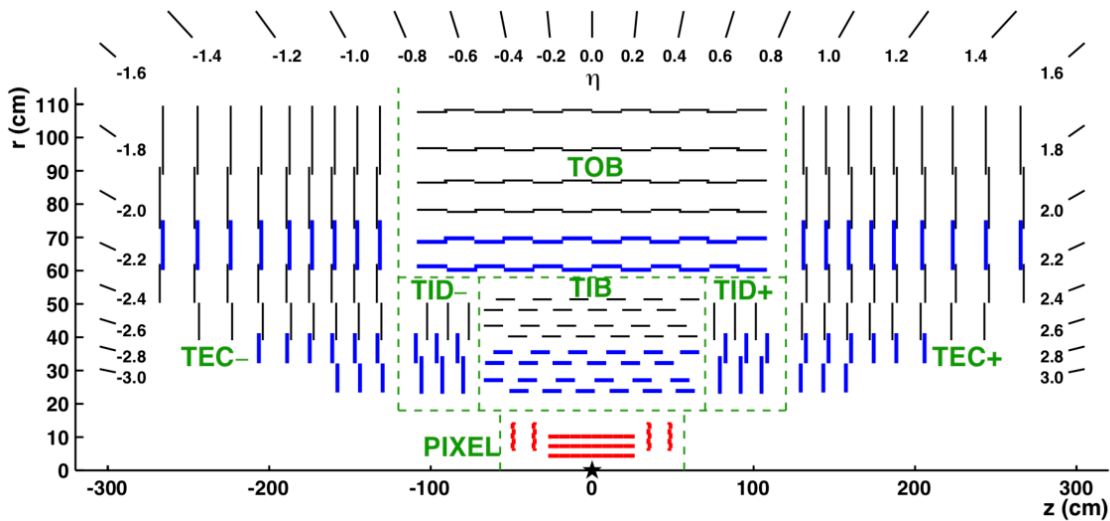
2.2.1.1 Tracking System

The CMS Tracking System is responsible for the measurements of trajectory and momentum of the particles produced in the collision and subsequently, the reconstruction of the position of primary and secondary vertices. The sub-detector covers a sensitive area of 200 m^2 and reaches from the interaction point up to 1.1 m^2 and offers acceptance up to a pseudorapidity of $|\eta| < 2.5$.

The tracker is divided based on two different technologies; a silicon pixel tracker for the innermost region close to the proton-proton interaction region and a silicon strip tracker for the outermost region.

- Silicon Pixel System:** With 66 million $100 \mu\text{m} \times 150 \mu\text{m}$ pixels sensors, it is divided in three cylindrical layers of the detector are placed at 4.3 cm, 7.2 cm, and 11 cm in the barrel region. Besides the 3-layers, two endcaps are located 34 cm and 46.5 cm away from the IP.
- Silicon Strip System:** Located in the radial region between 20 and 116 cm. The strip tracker is composed of three systems: the tracker inner barrel/disks (TIB/TID), the tracker outer barrel (TOB), and tracker endcaps (TECs). The TECs covers a z region between 120 cm and 280 cm.

Figure 7 - The CMS Tracking System layout.



Legend: The layout of the Tracking System with all subsystems. Only the positive side is shown.

Source: CHATRCHYAN et al., 2014, p.3.

Figure 7 shows a schematic cross section of the CMS tracking system with z and η acceptance.

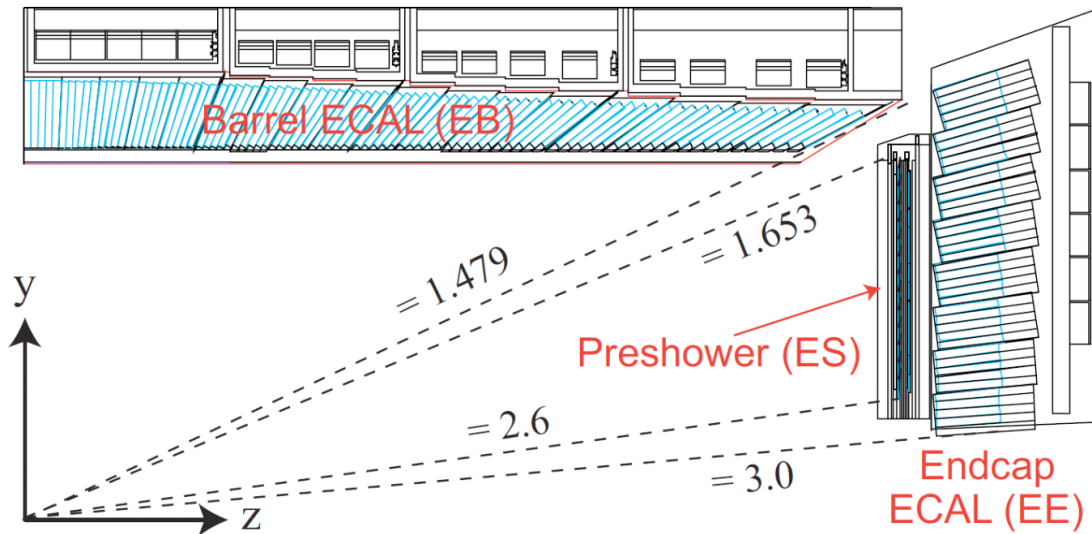
2.2.1.2 ECAL

The ECAL sub-detector is a hermetic, homogeneous lead-tungstate ($PbWO_4$) calorimeter composed of 75848 scintillating crystals divided between two sub-detectors: barrel part of the ECAL (EB), and the endcap ECAL (EE). It is used to measure the energy deposited by electrons, photons, and charged hadrons. The crystals then emit light in proportion to the particle's energy. The light is collected using photo-detectors located in the end of each crystal, which convert it into an electrical signal, that is amplified.

In addition, there are preshower systems (ES) placed in front of the ECAL endcaps, with the objective of identifying neutral pion decays into two photons and separating them from the primary photons.

Figure 8 shows a schematic cross section of the CMS ECAL along with the coverage of EB, EE and ES.

Figure 8 - The CMS ECAL schematic representation.



Legend: The layout of a ECAL cross section.

Source: CMS COLLABORATION, 2006, p.146.

2.2.1.3 HCAL

The Hadron Calorimeter (HCAL) of the CMS experiment is a hermetic sampling calorimeter that measures the energy deposited by hadrons, particles made of quarks and gluons (for example protons, neutrons, pions and kaons), produced in the collisions, and to help in the photon and lepton identification.

The HCAL covers region up to $|\eta| < 5$ with four sub-detectors: hadron calorimeter barrel (HB), hadron calorimeter endcaps (HE), outer hadron calorimeter (HO) and forward hadron calorimeter (HF).

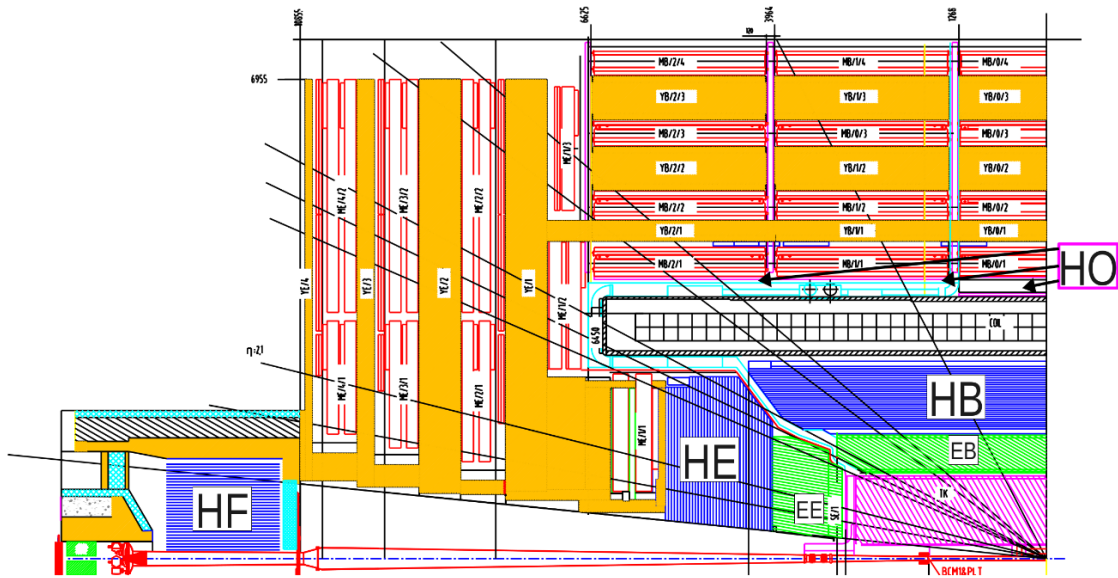
A schematic of the different HCAL subsystems is presented in Figure 9.

2.2.1.4 Muon System

After HCAL, the outermost layer of CMS houses the muon detector system, within the steel flux-return yoke. Since muons can traverse meters of iron without interacting, they are not stopped by the previous layers of the detector and reach these outer layers.

To detect the muons, four stations of gas-ionization detectors are installed outside the solenoid and placed between layers of iron return yoke plates. Muons are then reconstructed by combining the tracking system information with hits on the gas chambers, and fitting a trajectory.

Figure 9 - The CMS HCAL schematic representation.



Legend: Representation of the HCAL layout in addition to the electromagnetic calorimeter.

Source: MANS et al., 2012, p.3.

There are three kinds of muon subsystems in the CMS Muon System, the drift tube chambers (DT), the cathode strip chambers (CSC) and the resistive plate chambers (RPC).

Various properties and parameters of the muon subsystems are listed in Table 3. A longitudinal view of the detector showing the DT, CSC and RPC subsystems is presented in Figure 10.

2.2.2 Trigger System

With the high rate of collisions that occur in the LHC, a system that reduces this huge amount of information is very important. The bunch crossings happen with a frequency of 40 MHz and 1 MB average event size, 40 Tb/s of data has to be processed if every event is to be recorded. However, most of these events are not interesting for physics analyses.

To filter events which are of physics interest, CMS uses a two-tier trigger system: the Level-1 (L1) trigger and the High-Level Trigger (HLT).

- **Level-1 trigger:** The L1 trigger is able to reduce the data taking rate from 40 MHz to 100 kHz. It is based on hardware, collecting information from various sub-detectors as calorimeters and the muon system. L1 is also called online trigger as

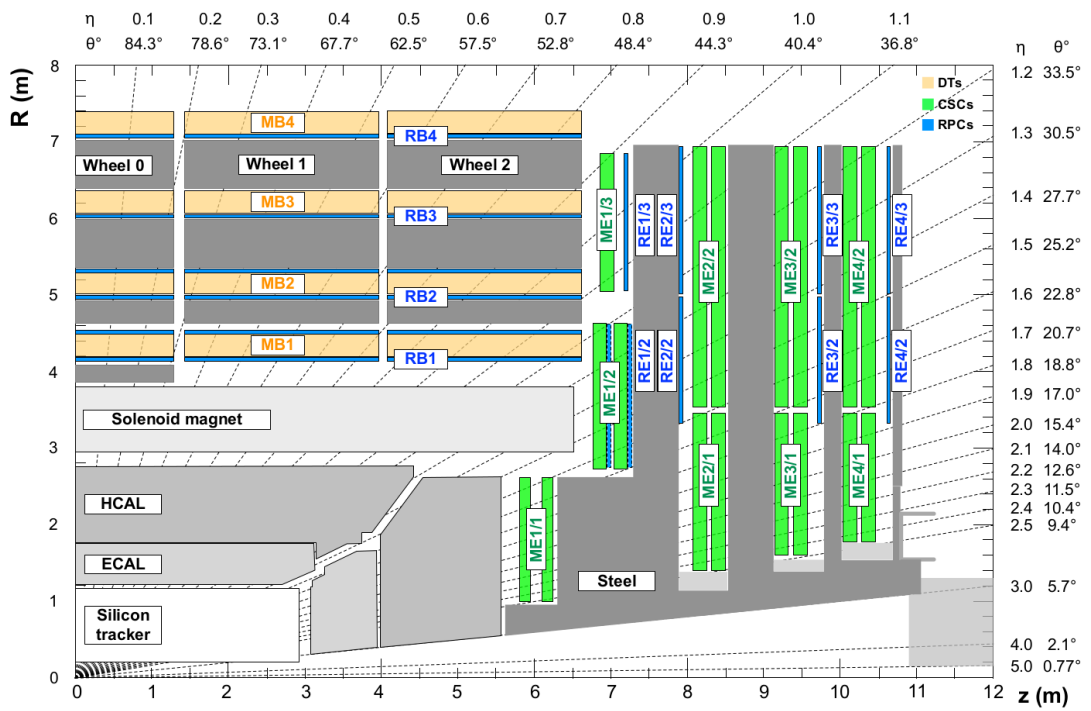
Table 3 - Properties for the CMS muon subsystems.

Muon subsystem	DT	CSC	RPC
$ \eta $ coverage	0.0 – 1.2	0.9 – 2.4	0.0 – 1.9
Number of stations	4	4	4
Number of chambers	250	540	Barrel: 480 Endcap: 576
Number of layers/chamber	R - ϕ : 8; z: 4	6	2 in RB1 and RB2 1 elsewhere
Number of readout channels	172000	Strips: 266112	Barrel: 68136 Endcap: 55296
Percentage of active channels	98.4%	Anode channels: 210816 99.0%	98.3%

Legend: Properties and parameters of the CMS muon subsystems during the 2016 data collection period. The values were extracted from (CMS COLLABORATION, 2018).

Source: The author, 2020.

Figure 10 - The CMS Muon system schematic representation.



Legend: The layout of a cross section of the Muon System.

Source: ABBIENDI, 2015, p.2.

events are triggered during the data taking.

The decision is taken by looking for a signal consistent with a muon in the Muon system, or a signal consistent with hadrons, photons, electrons in the HCAL and ECAL. The L1 system is composed of three subsystems: the L1 muon trigger, the L1 calorimeter trigger, and the L1 global trigger.

- **High-Level Trigger:** The HLT is able to reduce the data taking rate from 100 kHz to 1 kHz. It is a software-based selection system, using all the detector subsystems. Many algorithms process the event in parallel looking for different kinds of physic signatures. The combined set of L1 and HLT criteria for a given signature is referred to as a trigger path.

When the rate of a trigger path is high, one way of controlling its rate is by prescaling it. A prescale is a non-negative integer such that if a trigger has a prescale of N , then on average it records only $1/N$ of the events that pass its selection. For this dissertation, the prescale of all triggers utilized is 1, which means that the trigger records all events that pass its selection.

The HLT software is organized in a layered structure. The first layer uses the calorimetry and muon information, called Level-2. The next layer uses the pixel information, called Level-2.5 and the last one uses all the tracking detectors, Level-3.

2.2.3 Physics event reconstruction

The CMS experiment uses several standard algorithms to perform the reconstruction and identification of physics objects. A physics object is a set of combined information from deposits in different sub-detectors that can be associated with certain particle species. The Particle Flow (PF) algorithm (CMS COLLABORATION, 2017) is used to reconstruct these objects.

2.2.3.1 Particle Flow

The PF reconstruction starts by building PF elements out of deposits within each sub-detector, which are then connected together to form PF objects. These elements represent the signature caused by a single particle traversing the detector. Ergo, the PF algorithm provides the identification and reconstruction of particles using all the CMS sub-detectors.

The idea of the PF algorithm consists in reconstructing the trajectory of a charged

particle traversing the tracker through the calorimeters checking if they can be associated with boundaries of specific calorimeters clusters. The combination of all sub-detectors is then used to determine the four-momentum of the particles.

2.2.3.2 Muon reconstruction

The muons are reconstructed using the Tracking System and the Muon system. Muons are reconstructed if they have $p_T > 0.5$ GeV/c and $p > 2.5$ GeV/c in the tracker, and if the track can be extrapolated to a cluster in the Muon system. A fit is used to build the muon trajectory from a seed (DT or CSC clusters). The trajectory is determined using all Muon systems components (DT, CSC, and RPC).

An important quality selection for the muons produced is the muon identification. In this dissertation, the *tight* flag of the muon identification (ID) is considered. More details on the other muon-quality requirements can be found in (CMS COLLABORATION, 2018).

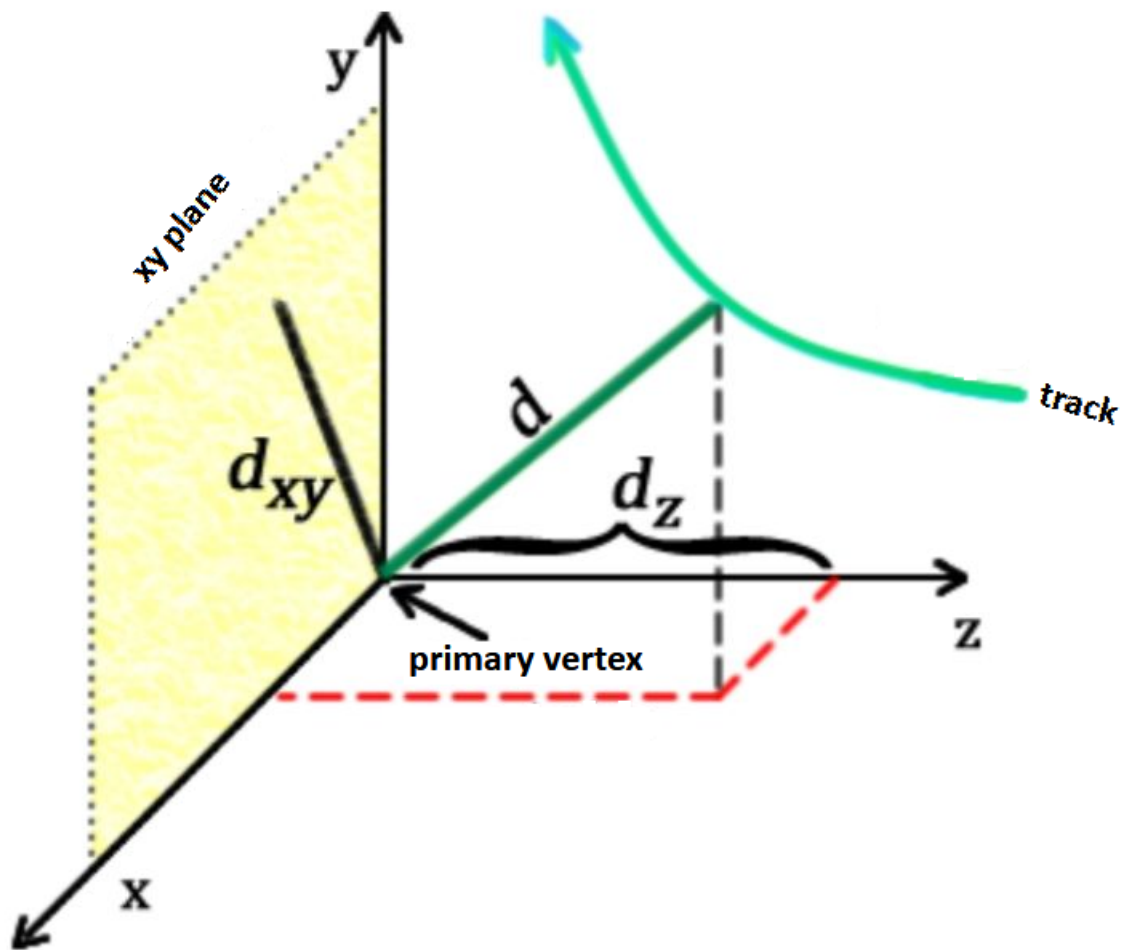
- **Tight Muon ID:** Aims to suppress muons from decay in flight and from hadronic punch-through — remnants of hadronic showers that can reach the muon system. A *tight muon* is a muon that passes the *loose* criteria with a track that has hits from at least six layers of the inner tracker including at least one pixel hit. The muon must be reconstructed as both a *tracker muon* and a *global muon*. The *tracker muon* must have segment matching in at least two of the muon stations. The *global muon* fit must have $\chi^2/\text{dof} < 10$ and include at least one hit from the muon system. A *tight muon* must be compatible with the primary vertex, having a transverse impact parameter $|d_{xy}| < 0.2$ cm and a longitudinal impact parameter $|d_z| < 0.5$ cm. Figure 11 shows how d_{xy} and d_z are obtained.

2.3 Precision Proton Spectrometer

The Precision Proton Spectrometer (CMS AND TOTEM COLLABORATIONS, 2014) — previously named CMS-TOTEM Precision Proton Spectrometer (CT-PPS) — adds precision proton tracking and timing detectors in the very forward region on both sides of CMS at about 200 m from the interaction point 5 (IP5), to measure the scattered protons that remain intact after the collision and correlate their kinematic information with the measurements in the central CMS sub-detectors.

With the increasingly number of interactions per bunch, the PPS helps improving the usual strategy to study Central (Semi)Exclusive Production, where the rapidity gaps in the central detector are used. It is designed to measure protons scattered at IP5 at

Figure 11 - d_{xy} and d_z illustration.



Legend: Illustration of how d_{xy} and d_z are obtained, where d is the impact parameter.

Source: The author, 2020.

small angles and fractional momentum loss (ξ) between ~ 0.02 and ~ 0.15 .

It started collecting data for analysis in 2016. It has two arms, located on both sides of CMS, at LHC sectors 45 (left arm, positive z direction) and 56 (right arm, negative z direction). During the 2017 data taking, each side of PPS was composed of two tracking stations, called “210 far” (210F) and “220 far” (220F). These tracking detectors are complemented by timing counters to measure the proton arrival time. They are placed at 214 m and 220 m away from the IP, respectively.

The detector planes are inserted horizontally into the beam pipe by means of “Roman Pots” (RPs), devices that allow the insertion of the sensors to a distance of a few millimeters from the beam, without effecting the vacuum, the beam stability, or other aspects of the accelerator operation.

In the 2017 configuration, the 210F stations were composed by 10 planes of silicon strip sensors, with each plane containing 512 individual strips. The 512 strips with $66 \mu\text{m}$ pitch are oriented at an angle of $+45^\circ$ on half of the planes and -45° for the other half with respect to the detector edge facing the beam. The 210F RP has a resolution of about $12 \mu\text{m}$. The 220F stations were composed by 6 planes, each with a $1.6 \times 2.4 \text{ cm}^2$ silicon 3D pixel sensor array read out by six PSI46dig ReadOut Chips (ROCs). Each ROC reads 52×80 pixels with dimensions $150 \times 100 \mu\text{m}^2$. The 220F RP has a x-coordinate resolution of about $15 \mu\text{m}$ and a y-coordinate resolution of about $30 \mu\text{m}$.

The schematic representation of the PPS detector and the LHC beam line at sector 56, with the technologies used for each year, is presented in figure 12. The detectors in sector 45 are symmetric with respect to IP5. The silicon strips in an RP are represented in Figure 14. A silicon 3D pixel picture is shown in Figure 13.

2.3.1 Alignment procedure

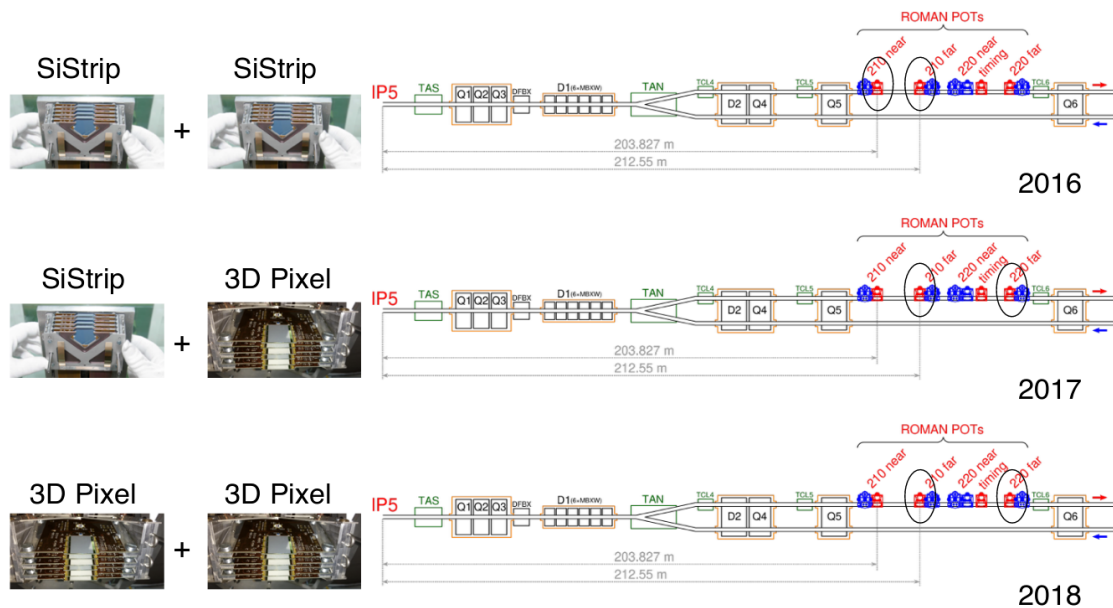
The fractional momentum loss of the proton is computed by the beam proton in the interaction as a function of the proton impact point in the RPs. Alignment of PPS is required to determine the relative position of the detector with respect to one another, the beam and the rest of CMS. An overview of the alignment procedure is given here; more details are available in (KASPAR, 2017) and (CMS AND TOTEM COLLABORATIONS, 2018).

The procedure consists basically of two parts:

- A low-luminosity calibration fill, called alignment fill, where RPs are inserted about $5\sigma^1$ to the beam;

¹ Standard deviation of the beam transverse dimension at the RP position.

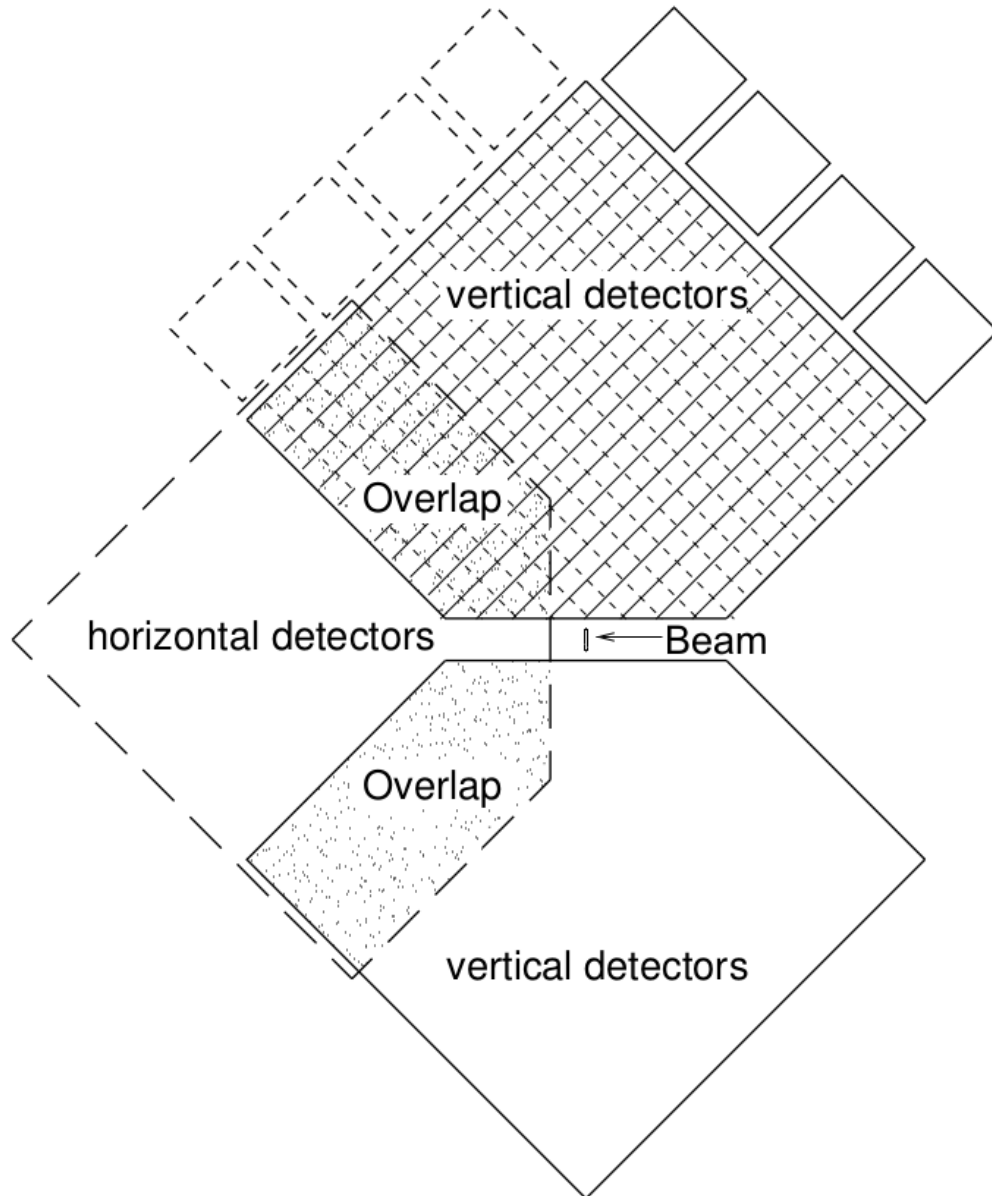
Figure 12 - Layout of PPS in LHC sector 56.



Legend: PPS detector layout in the LHC beam line in sector 56 as seen from above (not to scale), with the technologies used for each year. The stations with PPS detectors installed are marked in red. The following elements are indicated: the magnet dipoles (D1, D2), the quadrupoles (Q1-Q6), the collimators (TCL4-TCL6), the absorbers (TAS, TAN), the quadrupole feedboxes (DFBX), the TOTEM RPs (in blue), the PPS RPs (in red), the incoming beam (blue arrow) and the outgoing beam (red arrow).

Source: CMS COLLABORATION, 2020.

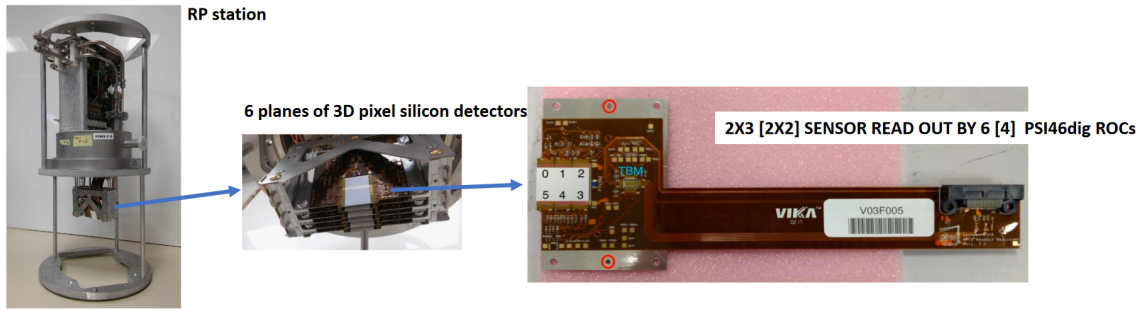
Figure 13 - Layout of PPS silicon strip sensors.



Legend: Schematic representation of silicon strip detectors approaching the beam from the top and bottom, and horizontally.

Source: CMS AND TOTEM COLLABORATIONS, 2018, p.4.

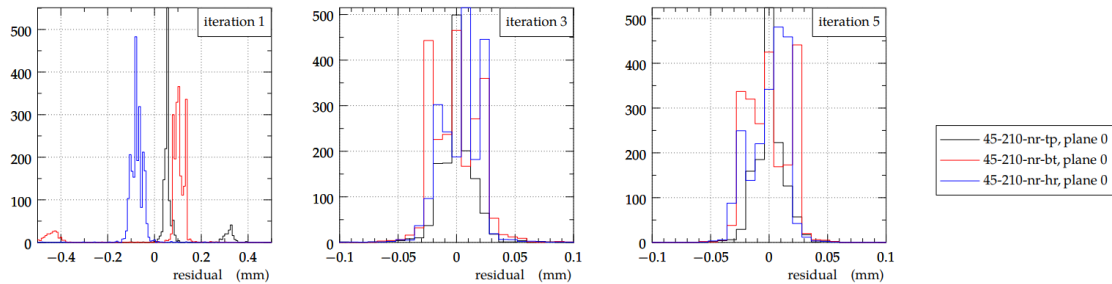
Figure 14 - PPS silicon 3D pixel sensors.



Legend: Picture of silicon 3D pixel detectors inside a RP.

Source: CMS COLLABORATION, 2019, p.3.

Figure 15 - Residual distributions for the RP relative alignment procedure.



Legend: Track-hit residual distributions with different sensors. Distribution before optimization (left), after shift optimization (middle) and after shift and rotation optimization (right).

Source: KASPAR, 2017, p.3.

- A high-luminosity physics fill, where the alignment information is transferred to the standard.

The beam is first scraped with the collimators so that it develops a sharp edge. An RP slowly approaches the beam; when the RP had contact with the edge of the beam and it has the same position as the collimator, a rapid increase in the rate is observed in the beam-loss monitors close to PPS. The alignment uses this position.

The next step consists of determining the relative position of all the RPs on each side of CMS using the data from the alignment fill, achieved by minimizing the residuals between hits and fitted tracks in each RP, optimizing position and rotation. Figure 15 shows an example of the procedure.

The alignment of PPS with respect to the beam is performed using samples of elastic scattering events, the process $pp \rightarrow pp$. The LHC optics causes the elastic hit

distribution in any vertical RP to have an elliptical shape centered on the beam position. The position of the RP with respect to the beam is determined utilizing this symmetry. The uncertainties in the results of the presented procedure are $50\ \mu\text{m}$ for horizontal shifts, $75\ \mu\text{m}$ for vertical shifts and $5\ \text{mrad}$ for rotations

Since the beam and RPs positions can change, the position of PPS with respect to the beam needs to be redetermined for each fill.

Since the RPs move, and the beam position can change, the position of PPS with respect to the beam needs to be redetermined for each fill. In the high-luminosity physics fills, contrary to alignment fills, only the horizontal RPs are inserted, and at a distance of around 15σ to the beam. The horizontal alignment is based on the assumption that the scattered protons from a pp collision at the IP have the same kinematic distributions in the two types of fills. The alignment is then performed matching these distributions from the physics fill with those in the alignment fill. An example of this procedure is shown in Figure 16. The uncertainty for the horizontal alignment in the physics fills is about $150\ \mu\text{m}$.

2.3.2 Proton reconstruction

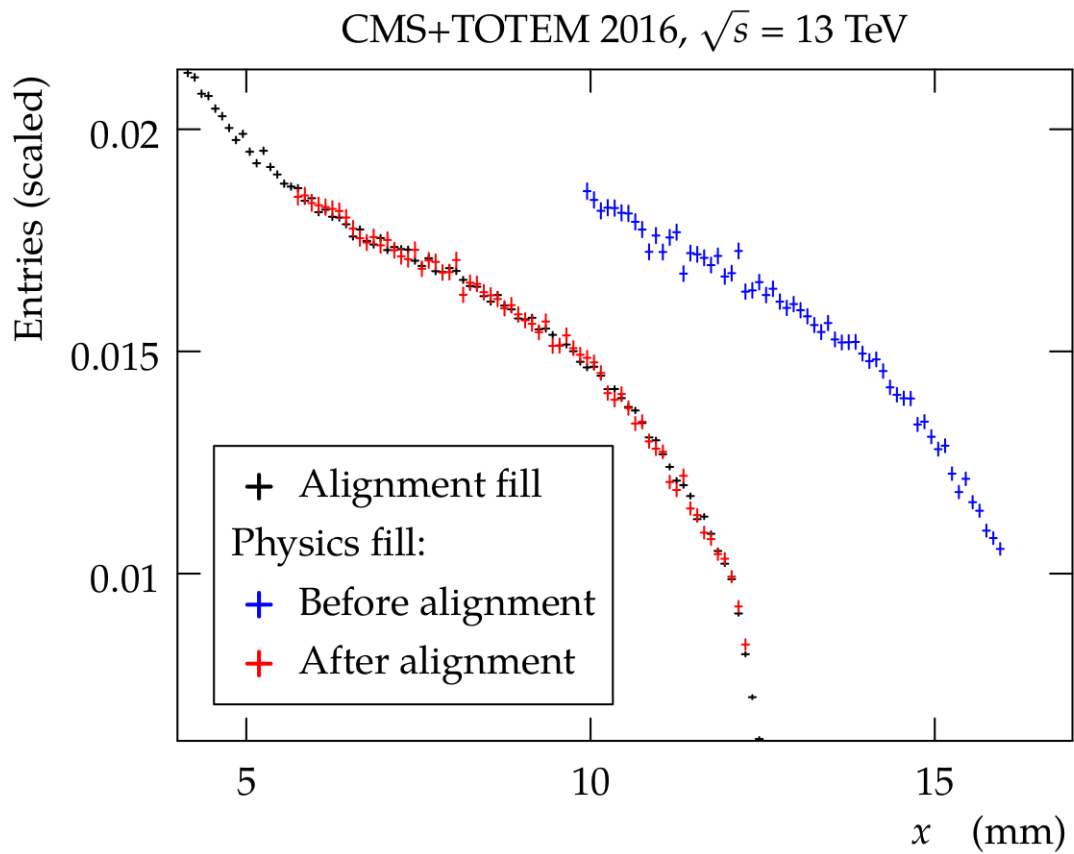
Reconstruction of the scattered protons depends on the track reconstruction in the RP and on the LHC beam optics. The latter parametrises the LHC magnet lattice and describe the proton transport from the IP to the RPs. The beam optics relates the proton kinematics at the IP and the hit position in the RP. An overview of the reconstruction is given here; more details are available in (NEMES, 2017).

2.3.2.1 Track reconstruction in the Roman Pots

The trajectory of the protons in the RP can be considered as a straight line since there is no significant magnetic field there. The track reconstruction requires hits in at least 3 planes and search for linear patterns along z among the detected hits. A fitted track produces a “track impact point”, with x and y coordinates, at the center of the RP (z direction). Figure 17 shows an example of the track impact point distribution measured in the 220F RP stations for 2017 data. The cyan band on the right-hand side of the sector 45 plot reflects the interaction of the protons with the upstream collimation system.

Two proton track reconstruction methods are recommended by the CMS Collaboration’s Proton Physics Object Group (POG), with the respective pros and cons for each method:

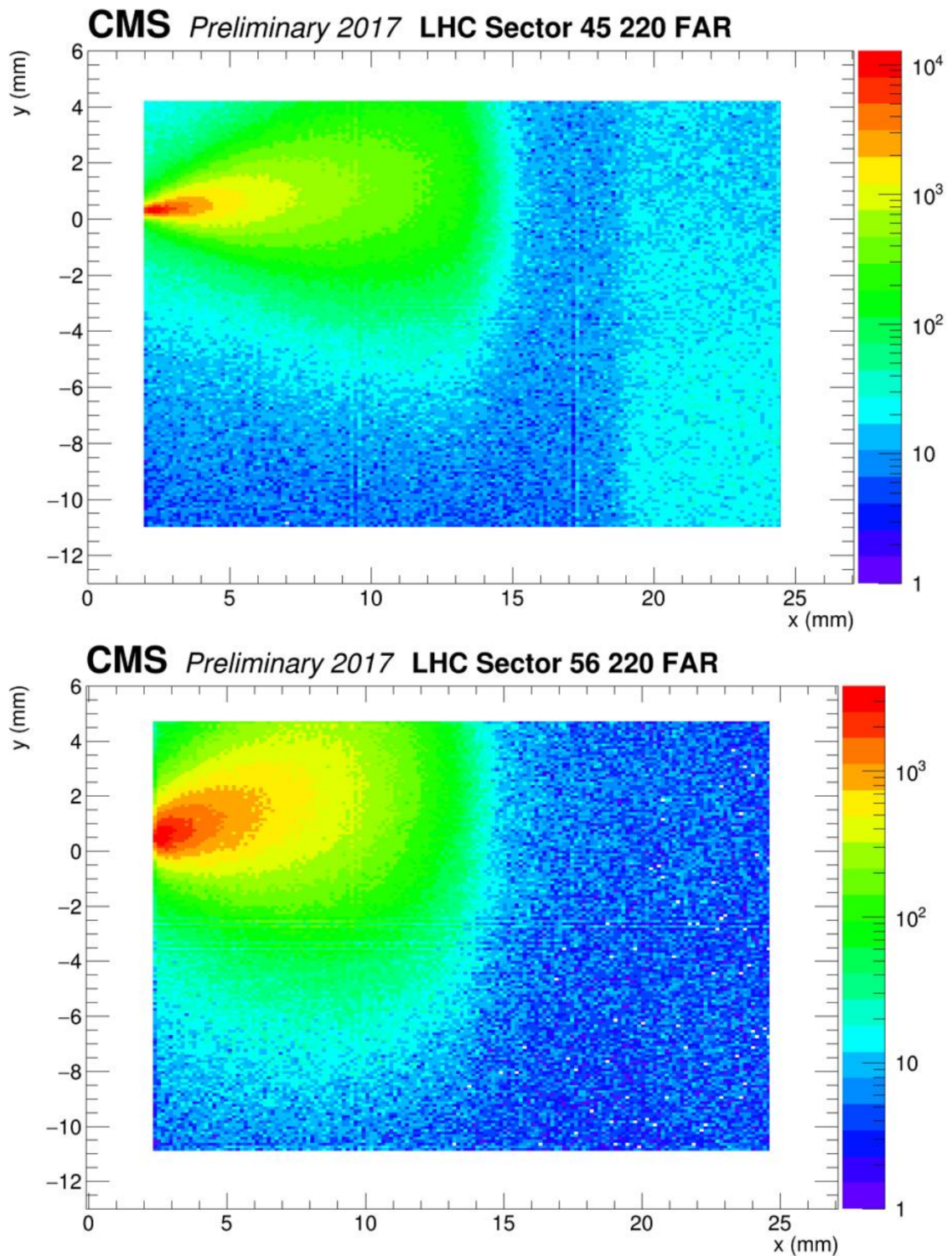
Figure 16 - Alignment procedure for physics fills.



Legend: Distribution of the track impact points as a function of the horizontal coordinate for the alignment fill (in black), a physics fill before alignment (in blue), and after alignment (in red).

Source: CMS AND TOTEM COLLABORATIONS, 2018, p.5.

Figure 17 - Track impact point distribution.



Legend: Distribution of the track impact points measured in sector 45 (top) and sector 56 (bottom) 220F stations. The beam center is at $x = y = 0$.

Source: CMS COLLABORATION, 2019, p.5. Adapted by the author.

- **Single-RP:** This method treats each tracking RP in a given arm as a separate detector, reconstructing tracks locally in each.
 - Neglects all but leading term in transport matrix (equation 7);
 - Individual results per RP (2 per arm). Simpler derivation and systematics, maximizes efficiency/acceptance;
 - ξ reconstruction only. Does not give full proton kinematics;
 - Resolution degrades especially for larger proton angles (θ_x) and larger ξ , due to neglected terms.
- **Multi-RP:** This method combines measurements of both tracking RPs in a given arm if both have one or more single-RP tracks reconstructed and these tracks are matched in coordinates between the two tracking RPs. The result is a global track.
 - Global fit from measurements in both RP stations;
 - Reconstructs full proton kinematics at IP;
 - Much better resolution/uncertainties at high ξ ;
 - Lower efficiency especially in configurations with SiStrip detectors (multiple tracks, radiation damage).

The RPs housing strip detectors can only reconstruct protons in events where only one proton hits the detector, otherwise ambiguities appear which turns impossible to associate the hits to the corresponding track. For high pileup events, there are presence of multiple tracks caused by the arrival of many scattered protons in the RP. Thereat, there is an inefficiency in the track reconstruction related to that in the strip detectors.

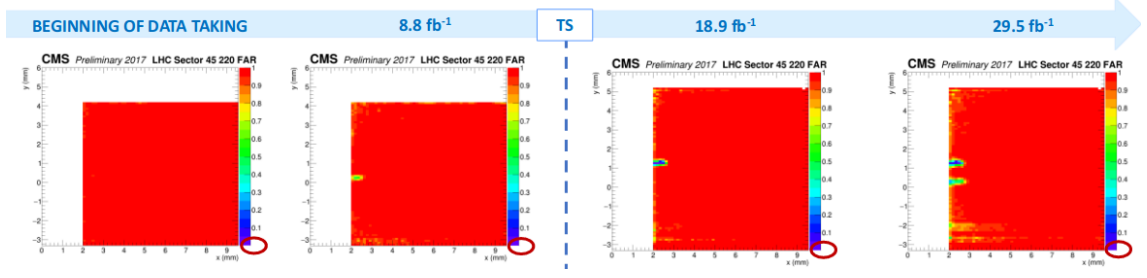
The radiation damage effect is another important inefficiency to take into account in the track reconstruction. The strip sensors are not designed to be exposed to high radiation doses. While the pixel sensors are radiation resistant, the pixel ROCs are not optimized for non-uniform radiation, as is the case of PPS. The analog signal of highly irradiated pixels drifts in time such that it may exceed the 25 ns acquisition window, after a dose corresponding to about 8 fb^{-1} . Figure 18 illustrates the radiation damage evolution in the pixel detector station.

To mitigate this effect, the tracking detectors were lifted during LHC technical stops during data taking, moving the maximum occupancy region close to the beam away from the damaged area. After the technical stop, when the detector was shifted, a second radiation damaged region appears.

For the pixel RPs, only the radiation damage inefficiency is taken into account, since the pixel RPs have the ability to disambiguate multiple tracks in the same event.

The inefficiencies are discussed again in light of the current analysis in section 4.6.3.

Figure 18 - Radiation damage evolution.



Legend: Evolution of the RP efficiency map in the detector region closest to the beam for LHC sector 45 in 2017.

Source: CMS COLLABORATION, 2019, p.10.

2.3.2.2 LHC beam optics

The reconstruction of the scattered proton momentum from the tracks measured in the RPs has a dependence on the magnetic field between IP5 and the RPs (NEMES, 2017). The description of this dependence can be parameterized in terms of the beam optics using the optical functions to determine the proton path, in which the elements of the beam line are treated as optical lenses. The proton trajectory can be described by:

$$\mathbf{d}(s) = T(s, \xi) \cdot \mathbf{d}^* , \quad (6)$$

where $\mathbf{d} = (x, \theta_x, y, \theta_y, \xi)$, s is distance from the IP, (x, y) are the transverse vertex position and (θ_x, θ_y) are the horizontal and vertical components of scattering angle. The asterisk (*) denotes the proton variables in the IP and $T(s, \xi)$ is the single-pass transport matrix, whose elements are the optical functions, given by:

$$T = \begin{pmatrix} v_x & L_x & m_{13} & m_{14} & D_x \\ \frac{dv_x}{ds} & \frac{dL_x}{ds} & m_{23} & m_{24} & \frac{dD_x}{ds} \\ m_{31} & m_{32} & v_y & L_y & D_y \\ m_{41} & m_{42} & \frac{dv_y}{ds} & \frac{dL_y}{ds} & \frac{dD_y}{ds} \\ 0 & 0 & 0 & 0 & 1 \end{pmatrix} \quad (7)$$

where $L_{x,y}$ is the effective length, $v_{x,y}$ is the magnification, $D_{x,y}$ is the dispersion and m_{ij} are the coupling coefficients that are zero for the LHC nominal optics by design. The optical functions are extracted with the analysis of elastic scattering data (TOTEM COLLABORATION, 2014). The horizontal dispersion can be written as:

$$D_x = \frac{\partial x}{\partial \xi} . \quad (8)$$

The transverse position of the proton traversing an RP with respect to the beam centre can be written as:

$$x(s_{RP}) = v_x \cdot x^* + L_x \cdot \theta_x^* - D_x \cdot \xi , \quad (9)$$

$$y(s_{RP}) = v_y \cdot y^* + L_y \cdot \theta_y^* - D_y \cdot \xi . \quad (10)$$

At high instantaneous luminosity, the leading terms for Equations 9 and 10 are:

$$x \approx |D_x| \cdot \xi , \quad (11)$$

$$y \approx L_y \cdot \theta_y^* . \quad (12)$$

In the horizontal direction, the dispersion D_x has a mild dependence on ξ , and the $L_x \cdot \theta_x^*$ term introduces fluctuations around the mean for a given value of ξ . The vertical dispersion D_y is considerably smaller than D_x . By combining the measurements from both tracking RPs in a detector arm and the calculated transport matrix, the full proton kinematics can be obtained.

2.3.2.3 Determination of ξ

The fractional momentum loss (ξ) is the main proton variable for CEP. With PPS, can be determined from the track impact point in a single RP, measuring x and correlating it to the value of ξ , using Equation 11. The main uncertainty in this procedure is related to the dispersion (D_x) calibration and the neglected terms in Equation 11, with respect to Equation 9. In the analysis using 2016 data (CMS AND TOTEM COLLABORATIONS, 2018) the uncertainty in the dispersion calibration was found to be around 5.5 %. The uncertainty in the horizontal alignment is estimated as 150 μm .

3 DATASETS AND SIMULATED SAMPLES

For a good understanding of the behavior of signal and background processes, a set of simulated events was used to reproduce the data as realistically as possible.

The event simulation can be basically divided into three steps: generation, simulation and reconstruction. The event generator has to be able to produce high energy collision processes with a set of conditions. An event can be generated using different Monte Carlo (MC) techniques.

Once the events are generated, the next step is to simulate the interaction of the particles passing through matter and electronic response of the detector. The simulated events have the same structure and are reconstructed in the same way as the data.

3.1 Datasets

The CMS datasets are often denominated by runs, which are the data collecting periods. These periods are divided in eras (A, B, C, etc).

During the 2017 data taking, pixel RPs sometimes took data in a different data acquisition (DAQ) setting in which 3 sensor planes out of 6 in the detector package were recording hits associated with the following bunch crossing. This was a countermeasure for the inefficiency caused by the radiation damage and was used only in the periods labelled 2017C2, 2017D, 2017F2, and 2017F3. In this DAQ setting, the standard method used for computing the efficiency cannot be used.

For this dissertation, the data taking periods, defined based on the PPS operation conditions, are listed below:

- **2017B:** From run 297020 (June 16, 2017) to run 299329 (July 18, 2017).
- **2017C1:** From run 299337 (July 18, 2017) to run 300785 (August 9, 2017).
- **2017C2:** From run 300806 (August 9, 2017) to run 302029 (August 30, 2017).
- **2017D:** From run 302030 (August 30, 2017) to run 303434 (September 20, 2017).
- **2017E:** From run 303435 (September 20, 2017) to run 304826 (October 12, 2017).
- **2017F1:** From run 304911 (October 13, 2017) to run 305114 (October 16, 2017).
- **2017F2:** From run 305178 (October 16, 2017) to run 305902 (October 31, 2017).
- **2017F3:** From run 305965 (October 31, 2017) to run 306462 (November 10, 2017).

The periods colored in green are used in the present analysis, while those in red were excluded.

For that reason, only a part of the total integrated luminosity for the 2017 data (Run II) collected by CMS (37.19 fb^{-1}) was used in this analysis, corresponding to an integrated luminosity of 18.34 fb^{-1} .

3.2 Simulated samples

3.2.1 Event generators

Different event generators were used in this analysis:

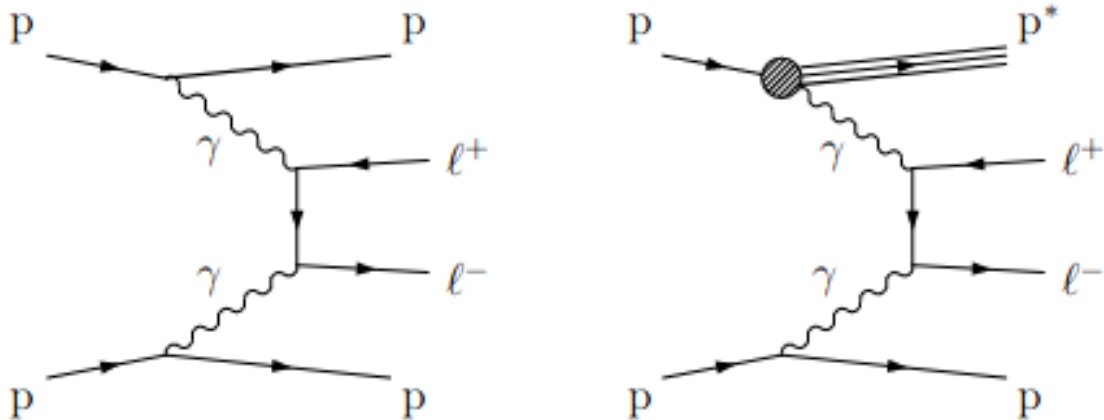
- **LPAIR** (BARANOV et al., 1991) is a event generator created to study processes of electromagnetic production of a lepton pair in lepton-lepton, lepton-hadron and hadron-hadron interactions, via $\gamma\gamma$ fusion. The LPAIR generator is based on a numerically stable formula for the matrix element of the $\gamma\gamma$ production of a pair of fermions, in which the beam particles can have arbitrary structure functions.
- **Pythia 8** (SJOSTRAND; MRENNNA; SKANDS, 2008) can be used either as a matrix element generator or to produce parton showers and hadronization when interfaced with other matrix element generators. It can generate Standard Model and Beyond Standard Model processes.
- **MadGraph5** (ALWALL et al., 2011) is a tool for automatically generating matrix elements for High Energy Physics (HEP) processes, such as decays and $2 \rightarrow n$ scatterings.

3.2.2 The Detector simulation

After the generation step, the components of each sub-detector have to be simulated to represent the traversing final state particles interaction with the detector material. The central detector information is passed through the standard **GEANT4** (AGOSTINELLI et al., 2003) simulation of the CMS detector and reconstructed in the same way as the collision data. For the PPS simulation, a more recent development has been created, as detailed in (SOUZA, 2017).

The simulation should be able to describe the interaction of the particles with the different detector materials and their response, as well as the active and dead material regions, the geometry, the magnet field, and finally the electronic signal. More details are presented in section 2.3.2 for the protons.

Figure 19 - Signal diagrams.



Legend: The exclusive (left) and single proton dissociation or semi-exclusive (right) topologies are shown. The processes result in at least one intact final-state proton.

Source: CMS AND TOTEM COLLABORATIONS, 2018, p.1. Adapted by the author.

3.3 The signal and background processes

3.3.1 The Signal

The signal consists of lepton pair production by photon exchange in the central (semi)exclusive production topology. For this dissertation, the lepton pair considered was $\mu^+\mu^-$ and it was simulated by the LPAIR generator.

The signal diagrams are shown in Figure 19. The signal samples used in the analysis are listed in Table 4 with their cross sections, the number of generated events and the rapidity gap survival probability (MARTIN; KHOZE; RYSKIN, 2008).

3.3.2 The Background

The main background considered in this analysis consists of the overlap of a pp collision and a track measured in the RP stations originating mainly from a pileup interaction, or a beam halo particle. The following processes are simulated:

- **Drell-Yan:** lepton pair production by quark-antiquark annihilation, via a virtual Z/γ^* decay. For the present analysis, the process has additional jets from the proton fragmentation and initial state radiation. It is generated by MadGraph5 in conjunction with Pythia 8.

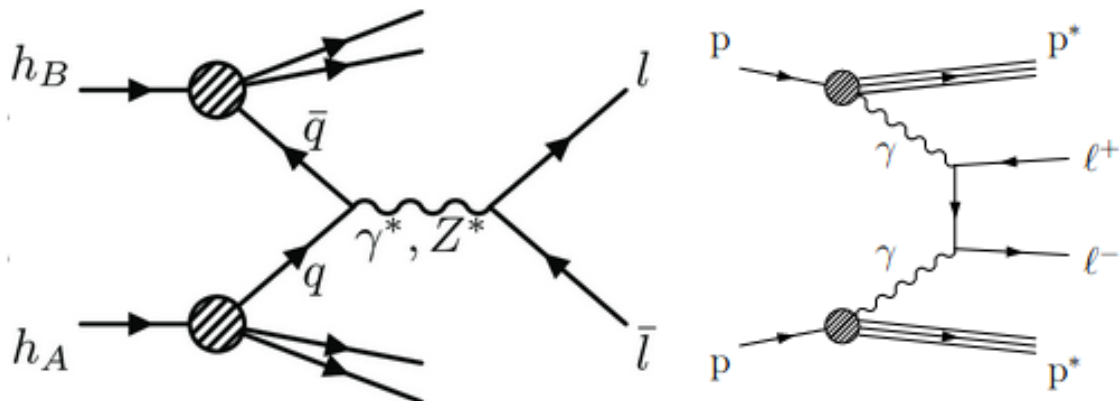
Table 4 - List of signal samples.

Sample	Cross Section (pb)	Number of Events	Rapidity Gap Survival Probability
LPAIR $\gamma\gamma \rightarrow \mu\mu$ $p_T(\mu) > 50 \text{ GeV}/c$ Exclusive 13 TeV	0.017	200000	89%
LPAIR $\gamma\gamma \rightarrow \mu\mu$ $p_T(\mu) > 50 \text{ GeV}/c$ Semi-exclusive 13 TeV	0.026	200000	76%

Legend: Summary of the signal samples used for the analysis, cross section, number of generated events and rapidity gap survival probability.

Source: The author, 2020.

Figure 20 - Background diagrams.



Legend: The Drell-Yan (left) and double proton dissociation (right) processes are shown.

Source: Drell-Yan diagram: BECHTEL, 2009, p.6; double proton dissociation diagram: CMS AND TOTEM COLLABORATIONS, 2018, p.1. Adapted by the author.

- **Double proton dissociation:** the process $pp \rightarrow p^* + \mu^+ \mu^- + p^*$, where both final state protons dissociate into a low-mass state. They cannot be measured by the PPS detector. The rapidity gap survival probability for the double proton dissociation is 13%.

The background diagrams are shown in Figure 20.

The Drell-Yan simulated sample is described in table 5, along with its cross section and number of generated events. Events are simulated with invariant mass of the lepton pair system $M > 50 \text{ GeV}/c^2$. The TuneCP5 underlying event tune was used in Pythia8. While the present analysis considers only muon pair final states, all lepton flavours are simulated in the Drell-Yan sample. The double proton dissociation simulation was not ready until the conclusion of this dissertation.

Using the results obtained from (CMS AND TOTEM COLLABORATIONS, 2018), the double proton dissociation events represent, approximately, 9.3% of the total background contribution, with the other 90.7% due to Drell-Yan events.

Table 5 - List of background sample.

Sample	Cross Section (pb)	Number of Events
MadGraph5 and Pyhtia8 DY + jets $\rightarrow \ell\ell$ $M(\ell\ell) > 50 \text{ GeV}/c^2$ TuneCP5 13 TeV	5.334	48675378

Legend: The background sample used for the analysis, cross section and number of events.

Source: The author, 2020.

4 DATA ANALYSIS

In this chapter the analysis of lepton pair production with protons measured in the PPS detectors is presented. The data were collected during the 2017 data taking, from proton-proton collisions at 13 TeV center-of-mass energy. The datasets corresponding to periods when the PPS detectors were operational are listed in section 3.1. Table 6 lists the integrated luminosity for each data taking period, where the *DoubleMuon* term means a muon pair in the final state.

The analysis and selection criteria followed those of (CMS AND TOTEM COLLABORATIONS, 2018). Efficiency and resolution scale factors are applied to the simulated samples, as explained in this chapter.

4.1 Trigger

The data used in this analysis are required to be triggered by one of the following HLT conditions (CMS COLLABORATION, 2017)):

- **HLT_DoubleMu43NoFiltersNoVtx_***: requires a muon pair with $p_T > 43$ GeV/c and no additional requirements on the isolation of the muons, their invariant mass and vertex position.
- **HLT_Mu17_TrkIsoVVL_Mu8_TrkIsoVVL_DZ_Mass3p8_***: requires one muon with $p_T > 17$ GeV/c and a second muon with $p_T > 8$ GeV/c. The HLT muon candidates are required to satisfy a loose isolation criteria defined by the ratio between the scalar sum of p_T of tracks around a cone of radius $\Delta R = 0.3$ around the muon and the muon p_T smaller than 0.4. The distance between the longitudinal impact parameter and the leading primary vertex is required to be less than 0.2 cm,

Table 6 - 2017 data samples used in the analysis.

Dataset	$\mathcal{L}(\text{fb}^{-1})$
2017RunB <i>DoubleMuon</i>	2.36
2017RunC1 <i>DoubleMuon</i>	5.31
2017RunE <i>DoubleMuon</i>	8.96
2017RunF1 <i>DoubleMuon</i>	1.71
Total	18.34

Legend: Data samples and their integrated luminosities.

Source: The author, 2020.

and the muon pair invariant mass is required in the range $M > 3.8 \text{ GeV}/c^2$.

- **HLT_Mu17_TrkIsoVVL_Mu8_TrkIsoVVL_DZ_Mass8_***: analogous to the previous trigger, in the muon pair invariant mass range $M > 8 \text{ GeV}/c^2$.

The measured efficiency of the trigger is not constant, therefore the Monte Carlo samples were corrected with scale factors (SF) binned in p_T and η , obtained from the Muon POG Twiki (CMS COLLABORATION, 2019).

4.2 Muons

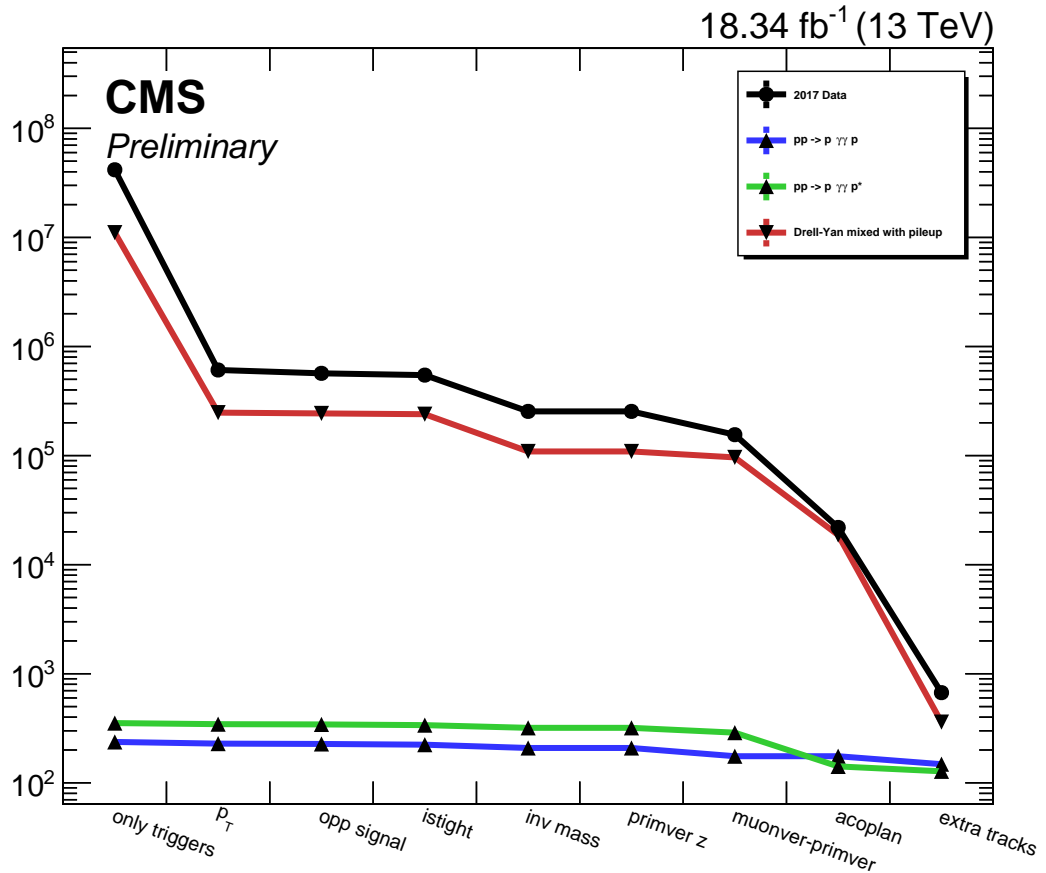
Events with oppositely charged muons passing the *tight* muon identification criteria were selected. The muon has to pass the requirements $p_T > 50 \text{ GeV}/c$; $M_{\mu^+\mu^-} > 110 \text{ GeV}/c^2$ (invariant mass of the pair), suppressing the region around the Z boson mass, which is expected to be dominated by Drell–Yan production; primary vertex position between $-15 < z < 15 \text{ cm}$; distance between $\mu^{+(-)}$ and primary vertex position $< 0.012 \text{ cm}$; and $a < 0.009$ (acoplanarity of the pair), where acoplanarity stands for $a = 1 - |\Delta\phi(\mu^+\mu^-)|/\pi$, consistent with the two muons being back-to-back in azimuth ϕ . As explained in section 4.6.1, the number of extra tracks in the vertex corresponding to the muon pair is required to be at most three, to select exclusive events where only the muon pair is expected and then, suppress non-prompt muons. Since the muon identification selection has different efficiencies in the data and simulation, scale factors to improve the description of the data by the simulation were applied.

4.3 Protons

Two distinct proton reconstruction categories were analysed. Events were selected with only one proton in a given detector arm and without restrictions, in the considered Roman Pots. The single-RP distributions use only the pixel RPs (220F), while the multi-RP uses all RPs (210F and 220F). Radiation damage inefficiencies are applied to the exclusive and semi-exclusive MC samples, as described later in this chapter. The full set of calculated multi-RP efficiencies is not yet available, and in this case only the data and the simulated background by mixing pileup protons are shown.

When using the selection without restrictions on the number of protons, a signal-induced background was studied by mixing pileup protons to the signal simulated data.

Figure 21 - “Cutflow” of the muon selections.



Legend: Comparison between 2017 data (black) and MC exclusive (blue), semi-exclusive (green) and DY mixed with pileup (red). Each x coordinate represents a selection, applied cumulatively towards the right. The MC samples are normalized.

Source: The author, 2020.

4.4 Baseline Event Selection

The muon related set of selections and the respective number of events used is summarized in Table 7. A “cutflow” of the muon selections is shown in Figure 21, following the same order of Table 7. The MC samples are normalized to respective cross-sections, luminosities, and rapidity gap survival probabilities.

Table 7 - Muon selection criteria list and number of events.

	2017 Data	pp \rightarrow p $\gamma\gamma$ p	pp \rightarrow p $\gamma\gamma$ p	pp \rightarrow p $\gamma\gamma$ p*	Drell-Yan mixed with pileup
only triggers	41730838	239	356	356	11171015
$p_T(\mu) > 50 \text{ GeV}/c$	609334	231	348	348	228086
oppositely charged muons	567759	229	346	346	224479
<i>tight</i> muon identification	546773	226	341	341	220848
$M_{\mu^+\mu^-} > 110 \text{ GeV}/c^2$	254223	211	322	322	107318
$ z $ of the primary vertex $< 15 \text{ cm}$	254213	211	322	322	107314
$ z(\mu^{+(-)}) - z(\text{PV}) < 0.012 \text{ cm}$	155469	177	291	291	94808
acoplanarity < 0.009	21943	177	143	143	19139
number of extra tracks on the primary vertex ≤ 3	671	150	129	129	341

Legend: Number of events after each muon selection criteria. The MC samples are normalized.

Source: The author, 2020.

Table 8 - Contributions of different crossing angles.

Crossing Angle (μrad)	Percentage
100	0.3
110	2.5
120	24.2
130	31.5
140	18.2
150	23.3

Legend: Fraction of events collected with each crossing angle value during the 2017 data taking.

Source: The author, 2020.

4.5 Data and MC Comparison

After the muon selection criteria discussed above, comparisons between data and MC is observed in the distributions of the muon pair mass, p_T and η , as shown in the top, middle and bottom figures of Figure 22, respectively.

4.5.1 Crossing Angle

The crossing angle is the angle between two opposite colliding beams. It is used to avoid unwanted collisions in machines with many bunches, like the LHC. The high collision rate with high pileup reduces the luminosity over the time and changing the crossing angle can help recovering some of the luminosity, as shown in Figure 23.

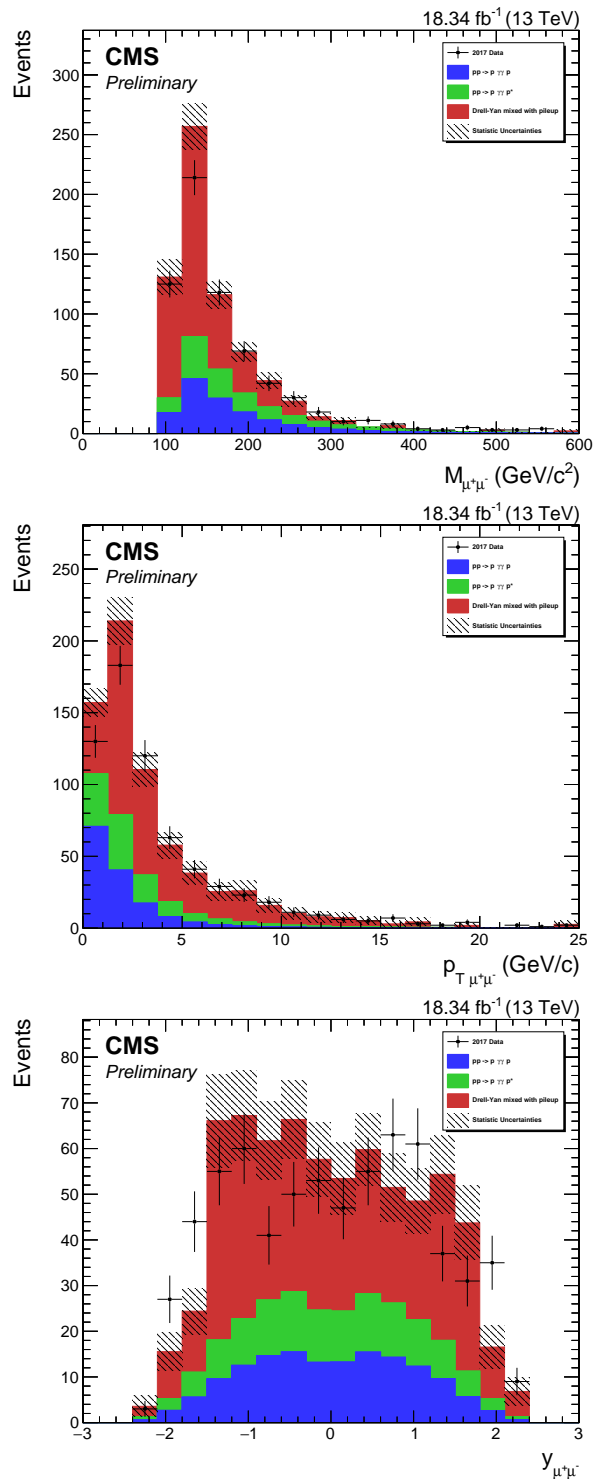
The signal event samples are simulated with *half* crossing angle values from 100 to 150 μrad , in steps of 10 μrad as in the data. They are normalized by the luminosity of the data collected with each crossing angle value. The contributions from each crossing angle are illustrated in Figure 24, which shows the same muon pair kinematic distributions for the data and simulated samples from Figure 22.

The luminosity collected with each crossing angle value is shown in Table 8.

4.5.2 Pileup reweighting

Monte Carlo samples and data do not have the same pileup conditions. The simulated samples are reweighted to match the pileup distribution in the data. More details in the section 4.6.1.

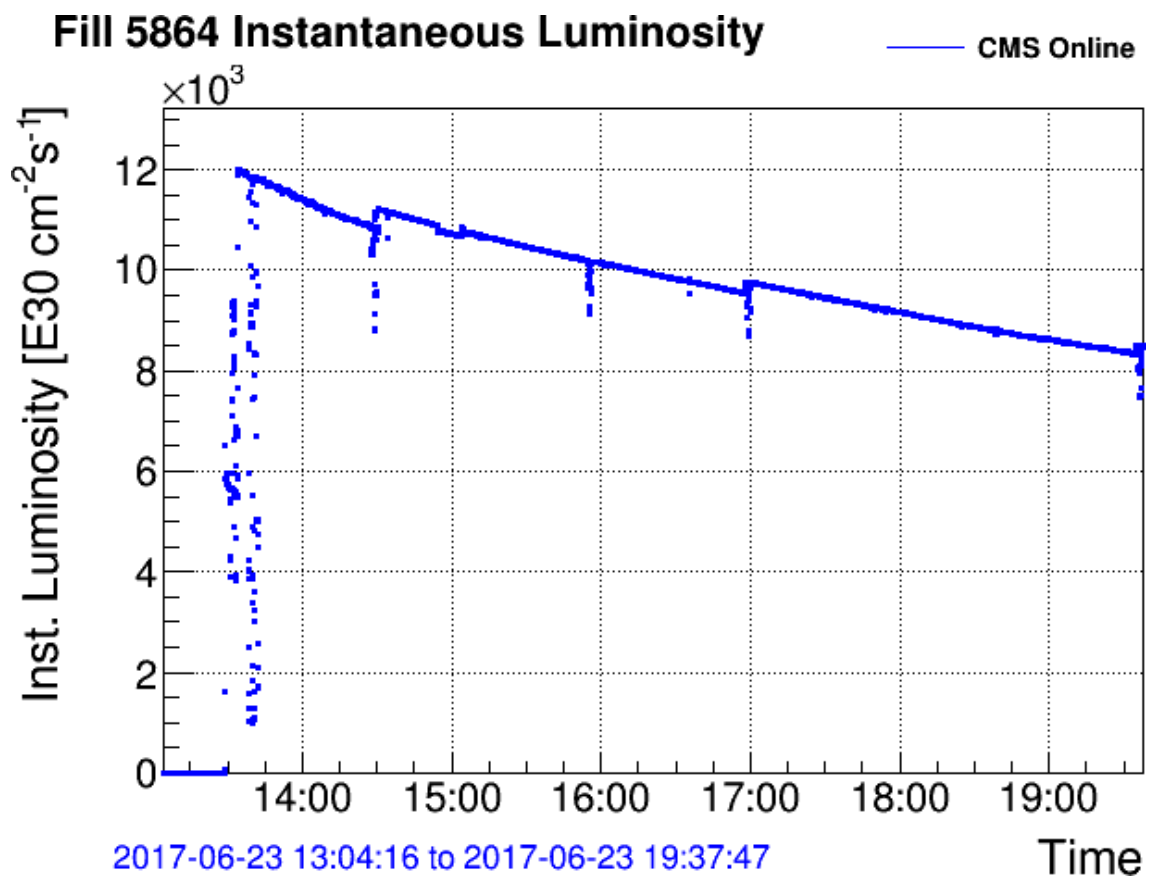
Figure 22 - Muon pair kinematic distributions for data and MC.



Legend: Comparison between data (black dots), exclusive (green histograms), semi-exclusive (blue histograms) samples, and DY simulated sample mixed with pileup (red histograms). Top: muon pair invariant mass. Middle: muon pair p_T . Bottom: muon pair rapidity. The hatched bands indicate the MC statistical uncertainty.

Source: The author, 2020.

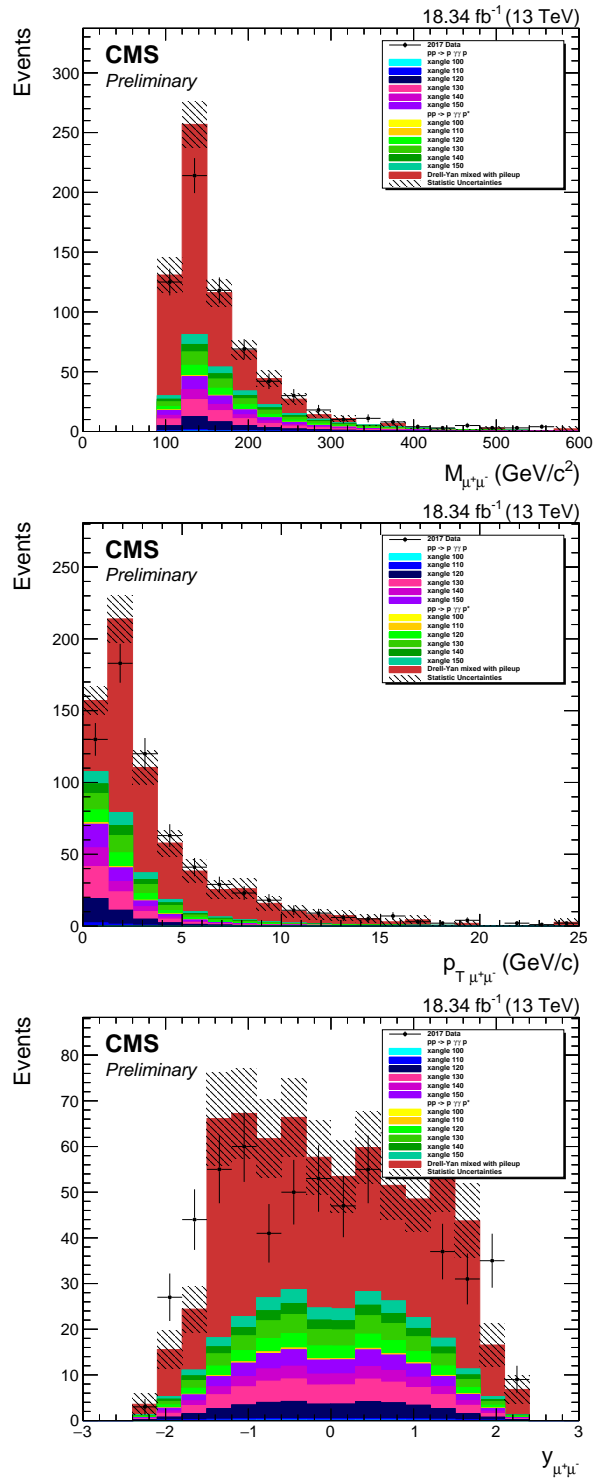
Figure 23 - Fill 5864 instantaneous luminosity.



Legend: Instantaneous luminosity for fill 5864 during the 2017 data taking. Each discontinuity in the luminosity distribution represents the change to a different crossing angle.

Source: CMS COLLABORATION, 2019.

Figure 24 - Muon pair kinematic distributions for data and MC and different crossing angles.



Legend: Comparison between data (black dots), exclusive and semi-exclusive samples separately for each crossing angle value (coloured histograms), and DY simulated sample mixed with pileup (red histograms). Top: muon pair invariant mass. Middle: muon pair p_T . Bottom: muon pair rapidity. The hatched bands indicate the MC statistical uncertainty.

Source: The author, 2020.

4.5.3 Drell-Yan resampling

The proton information from pileup events was added to the Drell-Yan simulated events. Events that were triggered by L1+HLT trigger paths selecting electrons and photons were used, aiming an unbiased pileup dataset. Combinations were produced by reusing each DY event several times with different pileup events, to increase the statistical significance of the background estimate. An C++ script was formulated to ensure the creation of different mixed DY+pileup events by adding an increment factor whenever the pileup sample completes a loop, making an offset between the two samples to be mixed.

4.6 **Central (Semi)Exclusive Production**

To discriminate signal and background, the multiplicity of extra tracks on the interaction vertex and the values of ξ reconstructed from the lepton pair and those reconstructed in the PPS detectors were used as follows.

4.6.1 Track Multiplicity

An extra track is defined as a track originating from the primary vertex and not corresponding to the muon pair. The signal region is defined as having at most 3 extra tracks. Figure 27 shows a comparison between the data and MC extra track distributions. A considerable discrepancy is observed between data and MC.

A study on the dependence of this discrepancy with the distance between the track and the primary vertex in the z coordinate was performed and no significant correlation was found. Figures 25 and 26 show the extra track multiplicity distributions when applying two different selections to associate a track to the event leading primary vertex (PV), respectively, for different values of the maximum track longitudinal impact parameter (dz). More details about the (CMS COLLABORATION, 2019).

Two track categories are defined, as described below:

- *PVUsedInFit*: if the track is used in the PV fit;
- *PVTight*: if the track is not used in the fit of any of the other PVs, and is closest in z to the PV;

When using *PVUsedInFit*, the simulated signal and background show better separation in the extra track multiplicity distribution, with respect to the selection using *PVTight*. The different dz selections do not significantly alter the distributions. The value of $dz < 0.3$ cm was used in the analysis.

With the *PVUsedInFit* selection and $dz < 0.3$ cm, the majority of the simulated signal events have 0—2 extra tracks. The selection of *PVUsedInFit* tracks was chosen as the nominal in the analysis.

The background simulated events were reweighted taking into account the extra track distribution to correctly describe the data, as illustrated in the bottom panel of Figure 27. The reweighting correction factors were calculated taking the ratio between the background simulated and the data events after subtracting the signal contribution, estimated from the simulated ones. An eighth order polynomial fit was performed to describe the ratio, as shown in Figure 28.

4.6.2 The fractional momentum loss of the scattered protons

As mentioned before, the value of the fractional momentum loss of the scattered proton is estimated from the leptons as:

$$\xi_{\ell^+\ell^-} = \frac{1}{\sqrt{s}} [p_T(\ell^+)e^{\pm\eta(\ell^+)} + p_T(\ell^-)e^{\pm\eta(\ell^-)}] , \quad (13)$$

where the two solutions for $\pm\eta$ correspond to the protons moving in the $\pm z$ direction.

To be considered as signal candidates, events are further required to have a value of $\xi_{\ell^+\ell^-}$ within the PPS coverage. For the left RP (220F, sector 45), $\xi_{RP} > 0.02$ and for the right RP (220F, sector 56), $\xi_{RP} > 0.03$. The ξ coverage difference between the sectors 45 and 56 is due to the asymmetric beam optics.

As the selection criteria are being applied, the selection efficiency is very low for DY events mixed with pileup, which show large statistical fluctuations. The resampling of the DY mixed with pileup protons samples helps with this matter. For the proton related distributions, the DY samples were resampled 100 times. An example of the resampling effect is presented in Figure 29, showing the ξ distribution for events in the pixel detector station in sector 56.

Finally, the signal region is defined by requiring that $\xi_{\ell^+\ell^-}$ and the corresponding value measured with PPS, ξ_{RP} , agree within 2σ , where σ is computed from $\sigma(\xi_{\ell^+\ell^-})$ and $\sigma(\xi_{RP})$ using the Equation 14:

$$\sigma = \sqrt{\sigma(\xi_{\ell^+\ell^-})^2 + \sigma(\xi_{RP})^2} . \quad (14)$$

The ξ resolution, $\sigma(\xi)$, is obtained from the simulation using residual distributions, $\left(\frac{\text{reconstructed} - \text{generated}}{\text{reconstructed}} \right)$. Figure 30 shows the residual ξ_{RP} distributions, relative to the simulated ξ . The absolute residual $\xi_{\ell^+\ell^-}$ distributions, obtained from the muon pair, are shown in Figure 31.

The ξ resolution was computed, using Gaussian fitting, in bins of ξ , considering a

Figure 25 - Extra track multiplicity distribution for tracks selected in category 2.

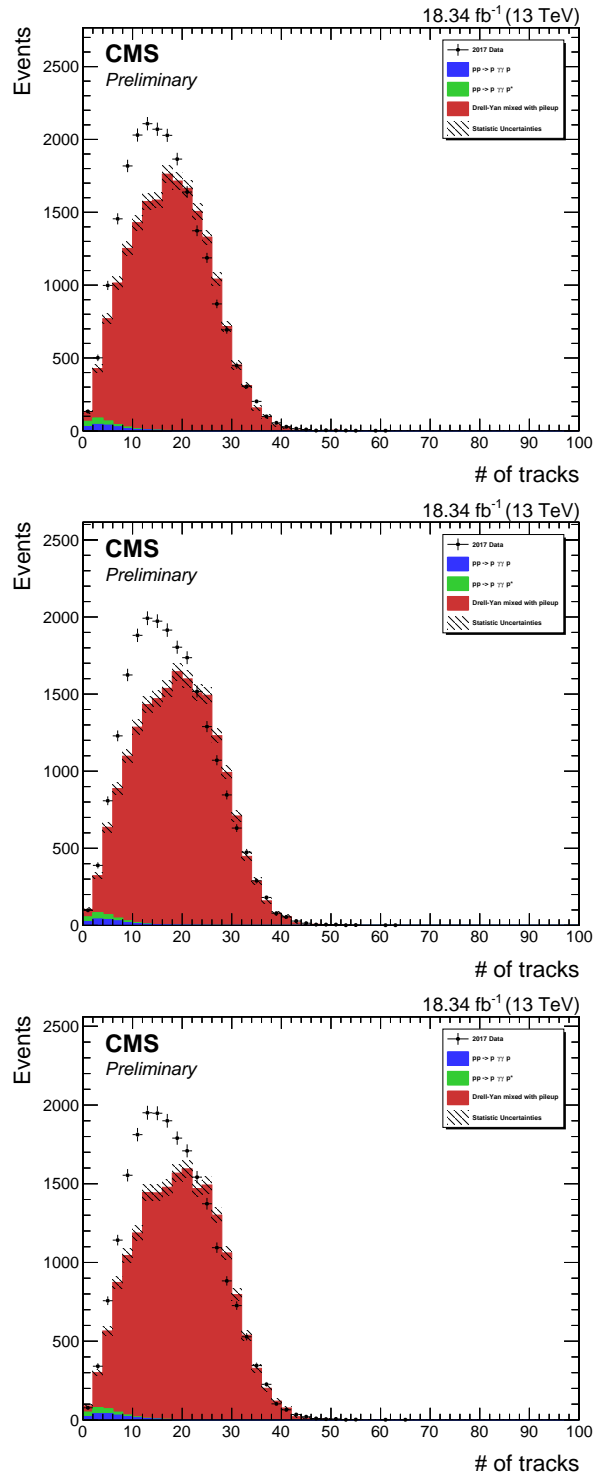
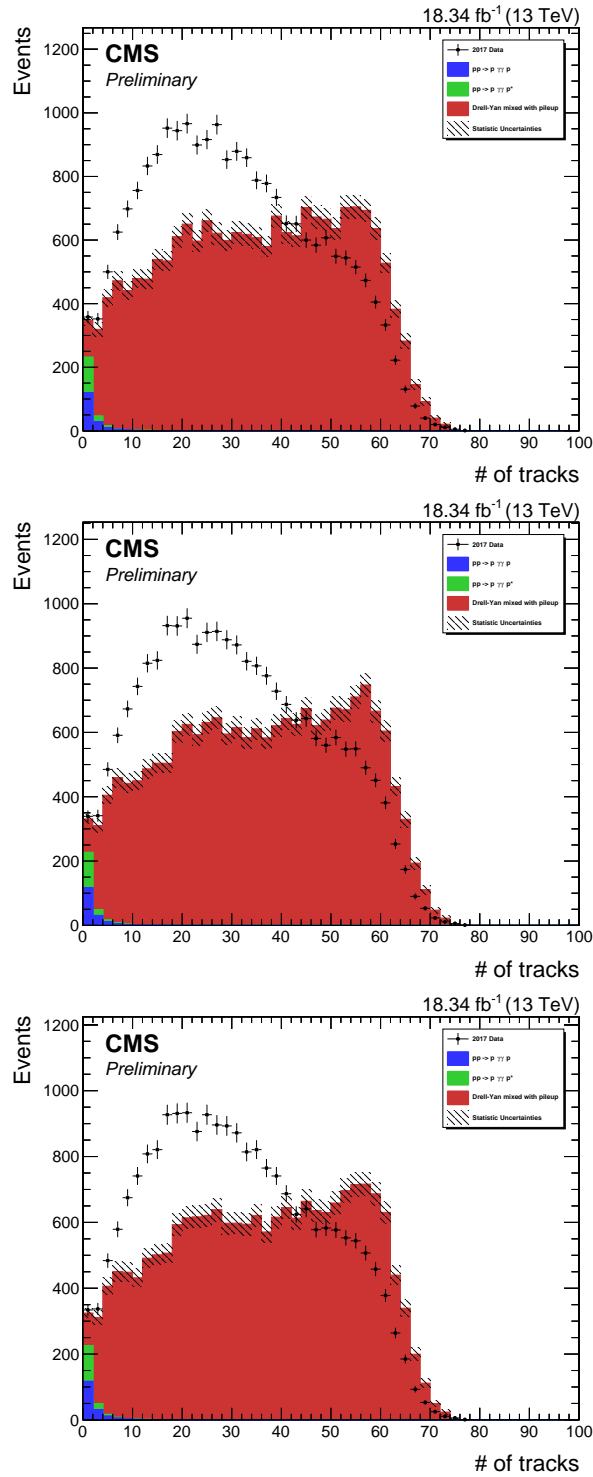


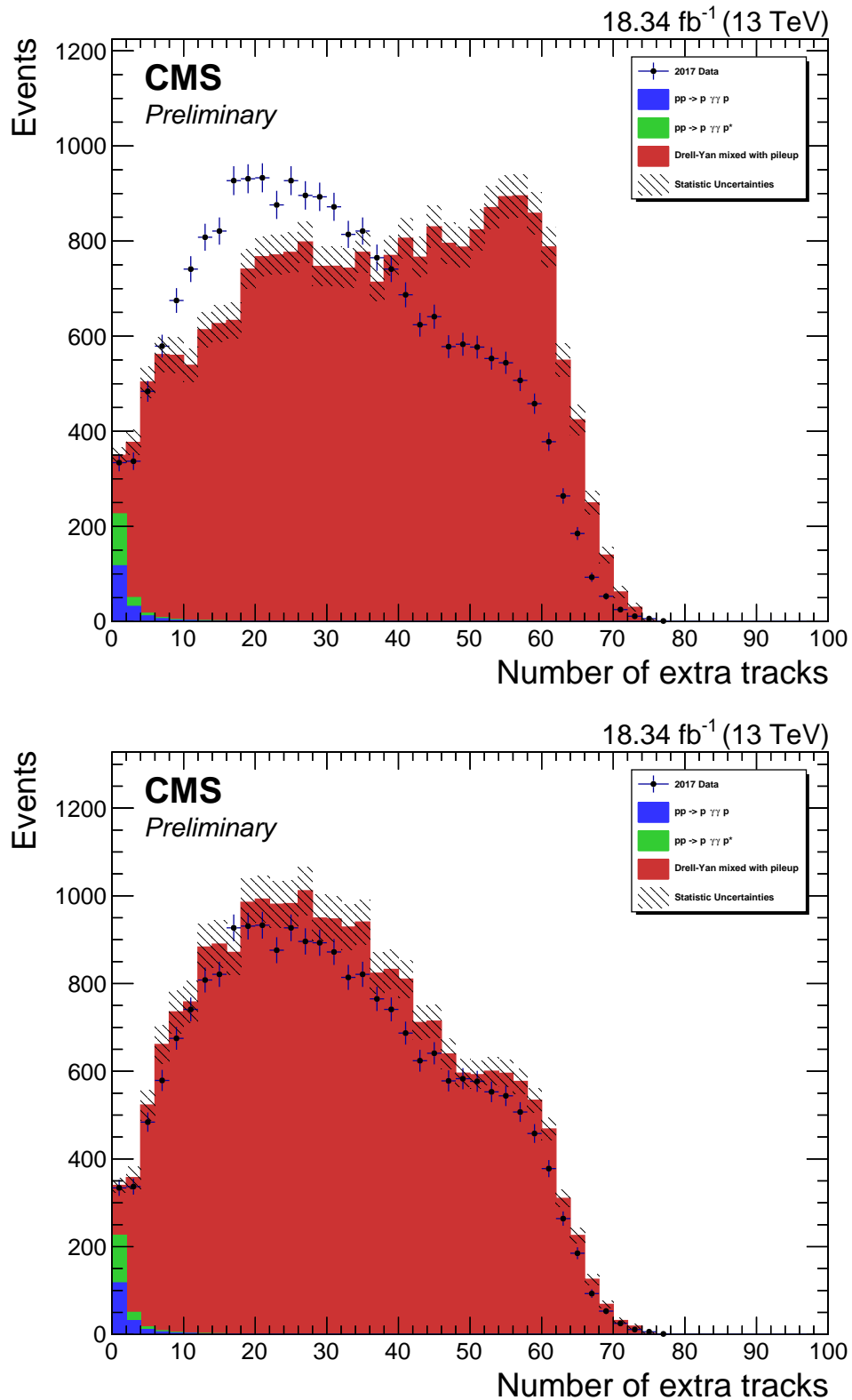
Figure 26 - Extra track multiplicity distribution for tracks selected in category 3.



Legend: Distribution of extra track multiplicity with tracks selected in category 3, with $dz < 0.1$ cm (top), $dz < 0.2$ cm (middle) and $dz < 0.3$ cm (bottom).

Source: The author, 2020.

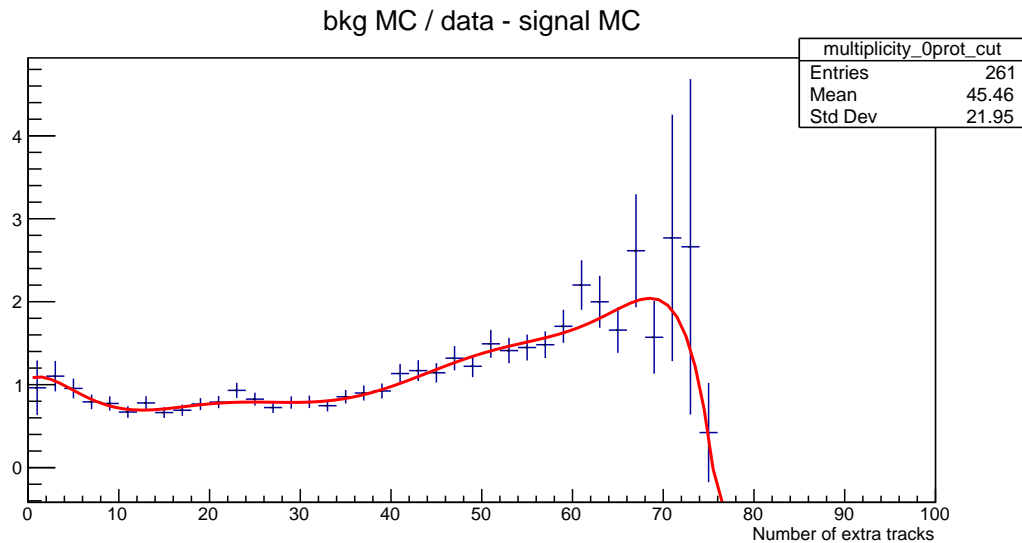
Figure 27 - Data and MC extra track distributions.



Legend: Comparison between the data and MC extra track distributions, before (top) and after (bottom) the reweighting correction factors are applied.

Source: The author, 2020.

Figure 28 - Extra track reweighting correction factors.



Legend: Ratio between the background MC and the data after subtracting the signal contribution. The ratio is described by a high-order polynomial fit.

Source: The author, 2020.

linear dependence of $\sigma(\xi)$ versus ξ , as shown in Figure 32 for ξ_{RP} and in Figure 33 for $\xi_{\ell+\ell-}$. As the MC samples have low statistics at large ξ values, only the range between 0.02 and 0.10 was considered.

With $\sigma(\xi_{\ell+\ell-})$ and $\sigma(\xi_{RP})$ obtained from the method explained above, the 2σ signal region can be defined, as shown in the $\xi_{\ell+\ell-}$ versus ξ_{RP} distributions in the case of protons reconstructed with the single-RP method, in figure 34 when the selection requires only one proton in the PPS detector and in Figure 35 when no restriction is applied in the number of reconstructed protons. Figure 36 shows the $\xi_{\ell+\ell-}$ versus ξ_{RP} distributions for multi-RP protons.

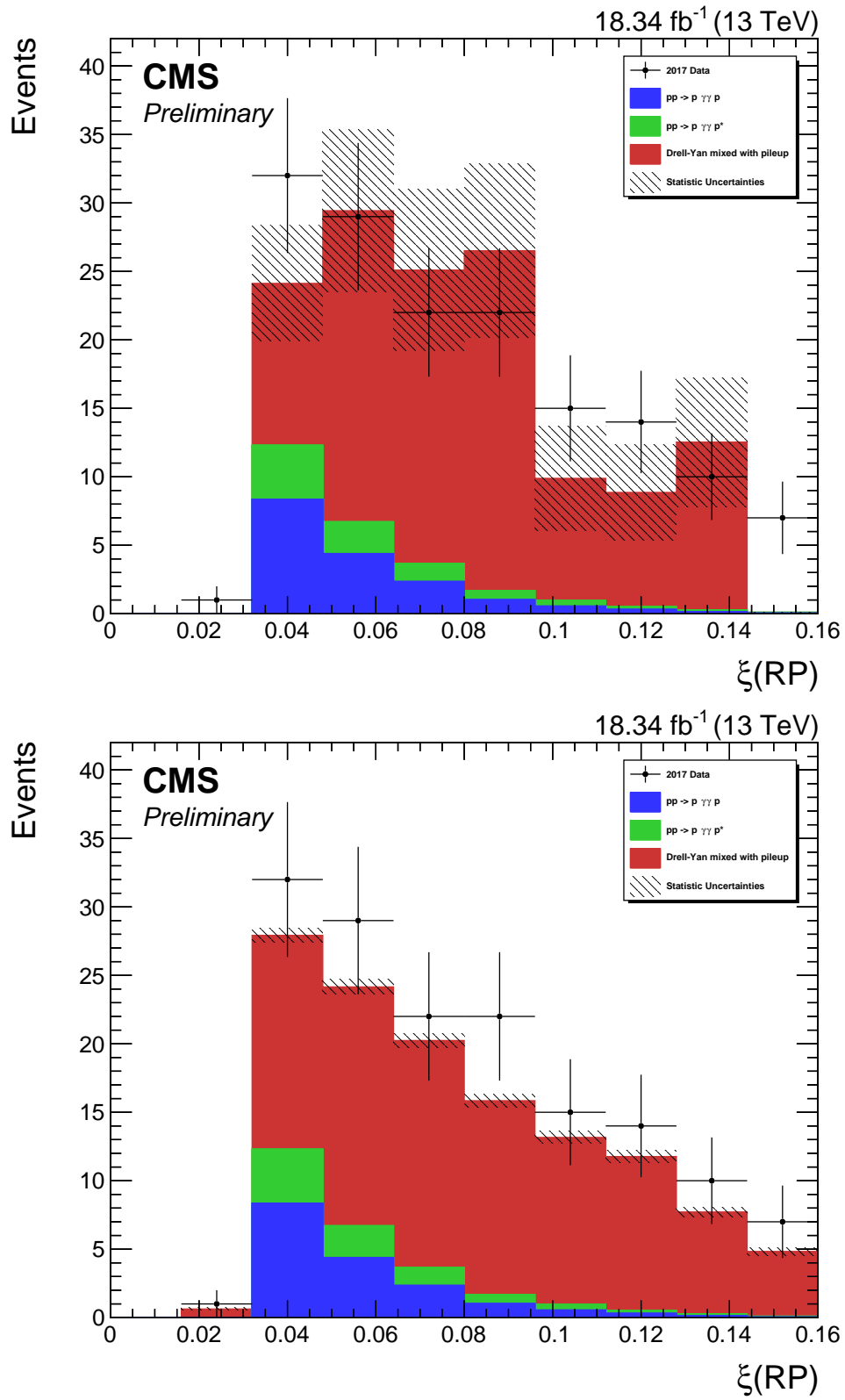
When no selection is applied on the number of reconstructed protons, a larger event sample in the signal region is observed, when comparing to the selection requiring only one proton in the PPS detector.

As expected, the multi-RP reconstruction provides better resolution than the single-RP case. The multi-RP efficiency is considerably lower, especially in the dataset used in this analysis, with a combination of strip and pixel detector stations.

4.6.3 Inefficiencies and scale factors

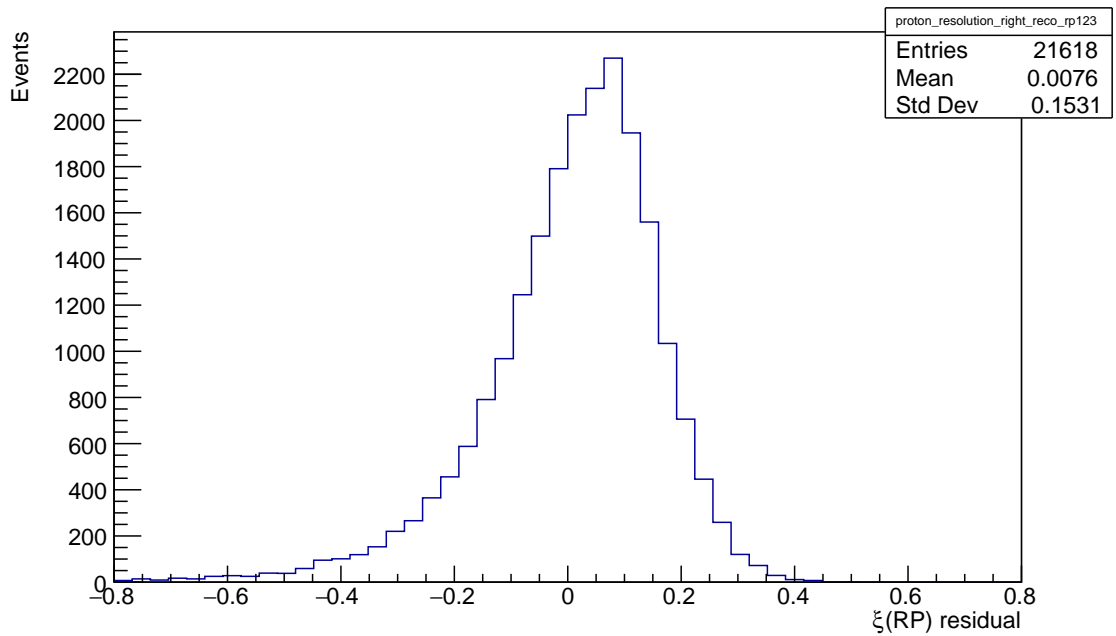
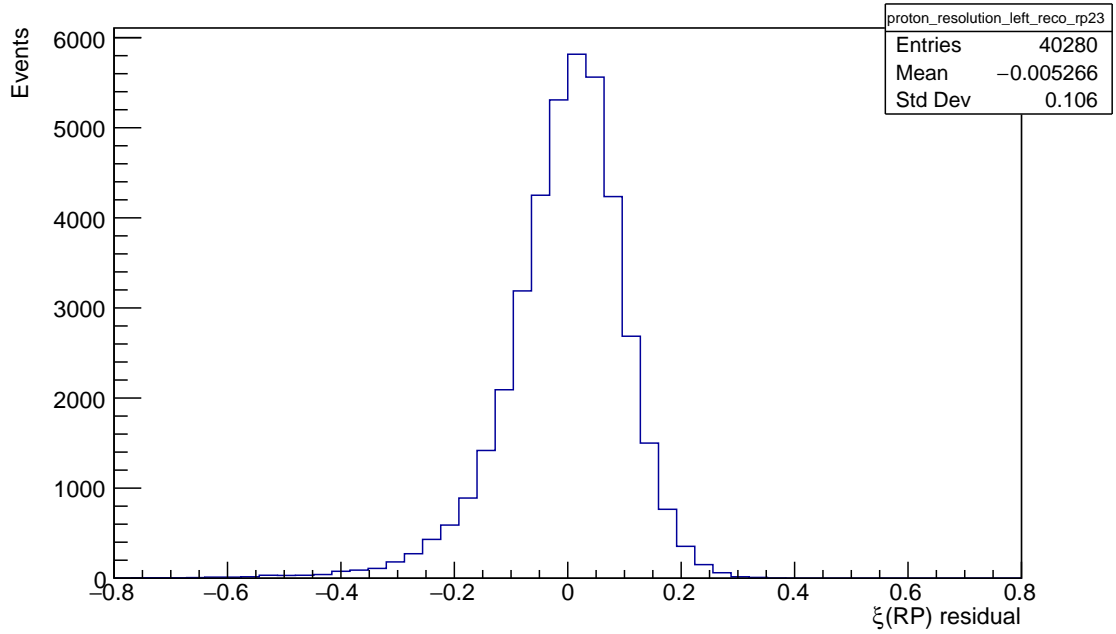
As mentioned in section 2.3.2.1, some inefficiencies have to be taken into account:

Figure 29 - Resampling effect in the mixing of DY events and pileup protons.



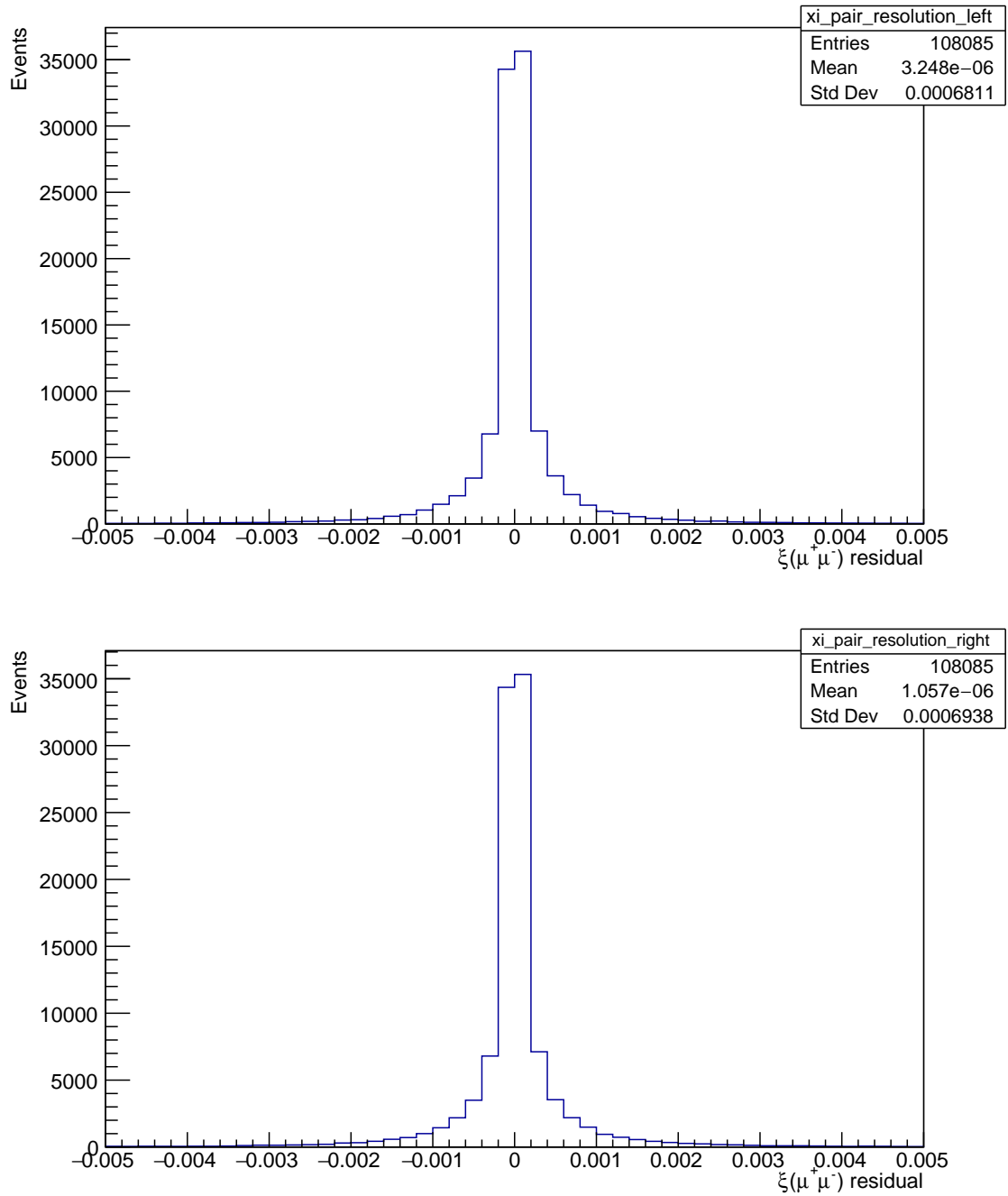
Legend: Single-RP ξ distribution in the pixel detector in sector 56 without (top) and when resampling 100 times (bottom).

Source: The author, 2020.

Figure 30 - Proton ξ resolution.

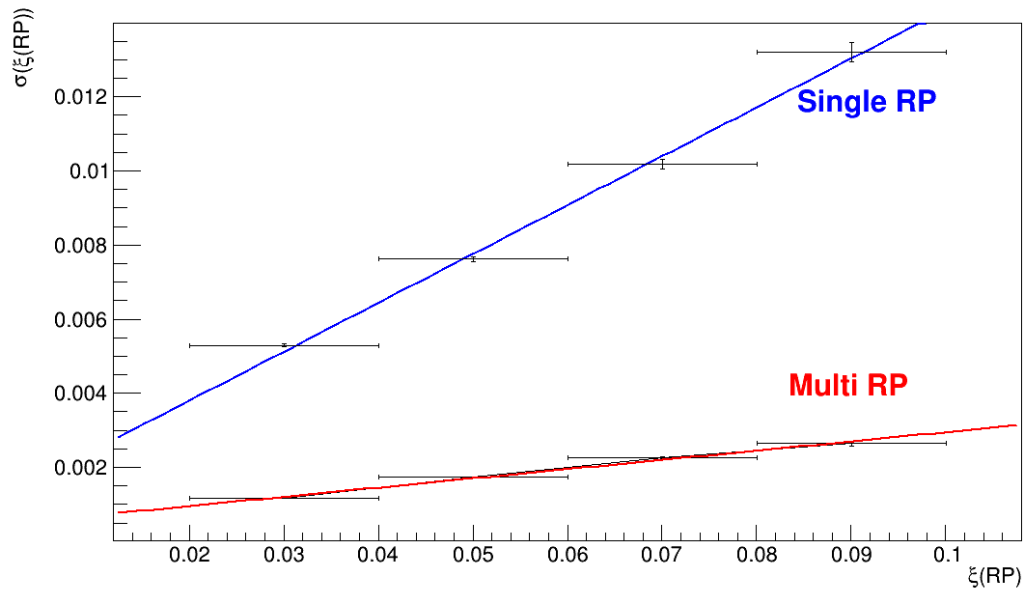
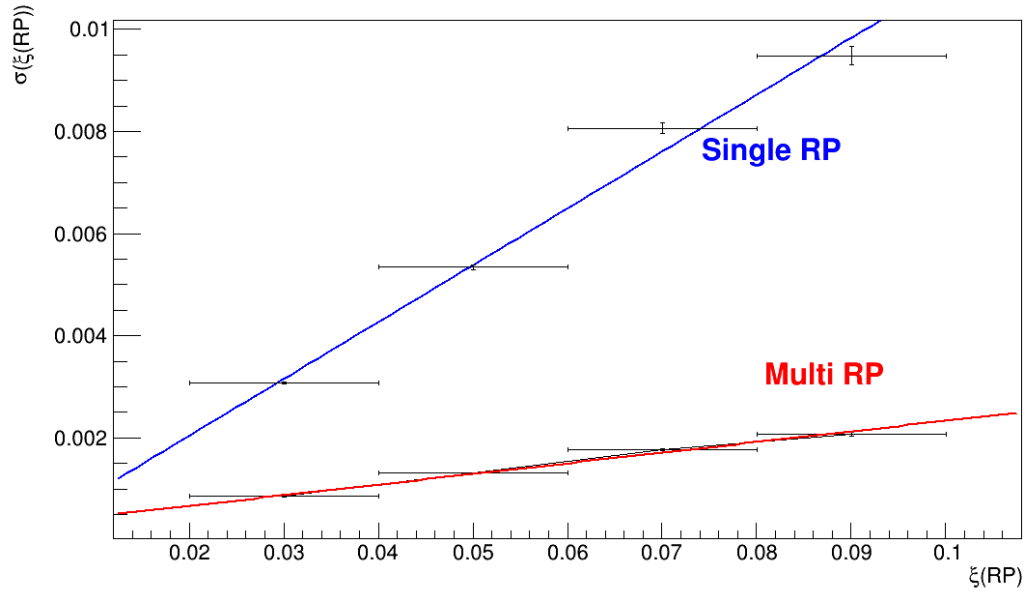
Legend: Residual ξ_{RP} distributions, relative to the simulated ξ , for single-RP protons in sector 45 (top) and sector 56 (bottom).

Source: The author, 2020.

Figure 31 - Muon pair ξ resolution.

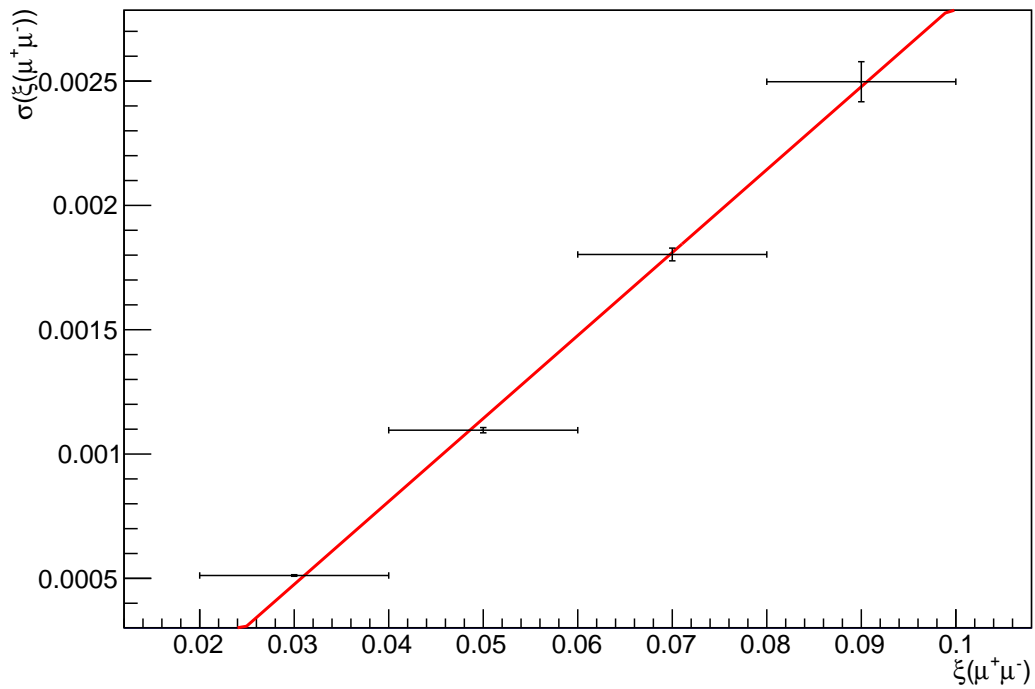
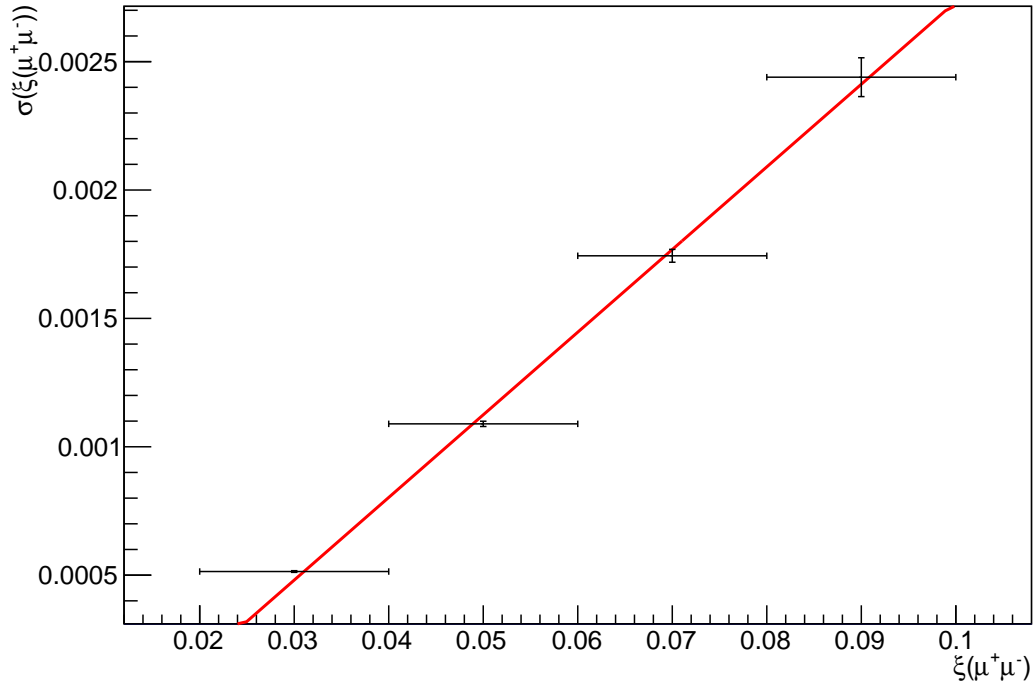
Legend: Residual $\xi_{\ell+\ell^-}$ distributions, obtained from the muon pair, for events with protons scattering to the negative z direction (top) and positive z direction (bottom).

Source: The author, 2020.

Figure 32 - ξ_{RP} resolution.

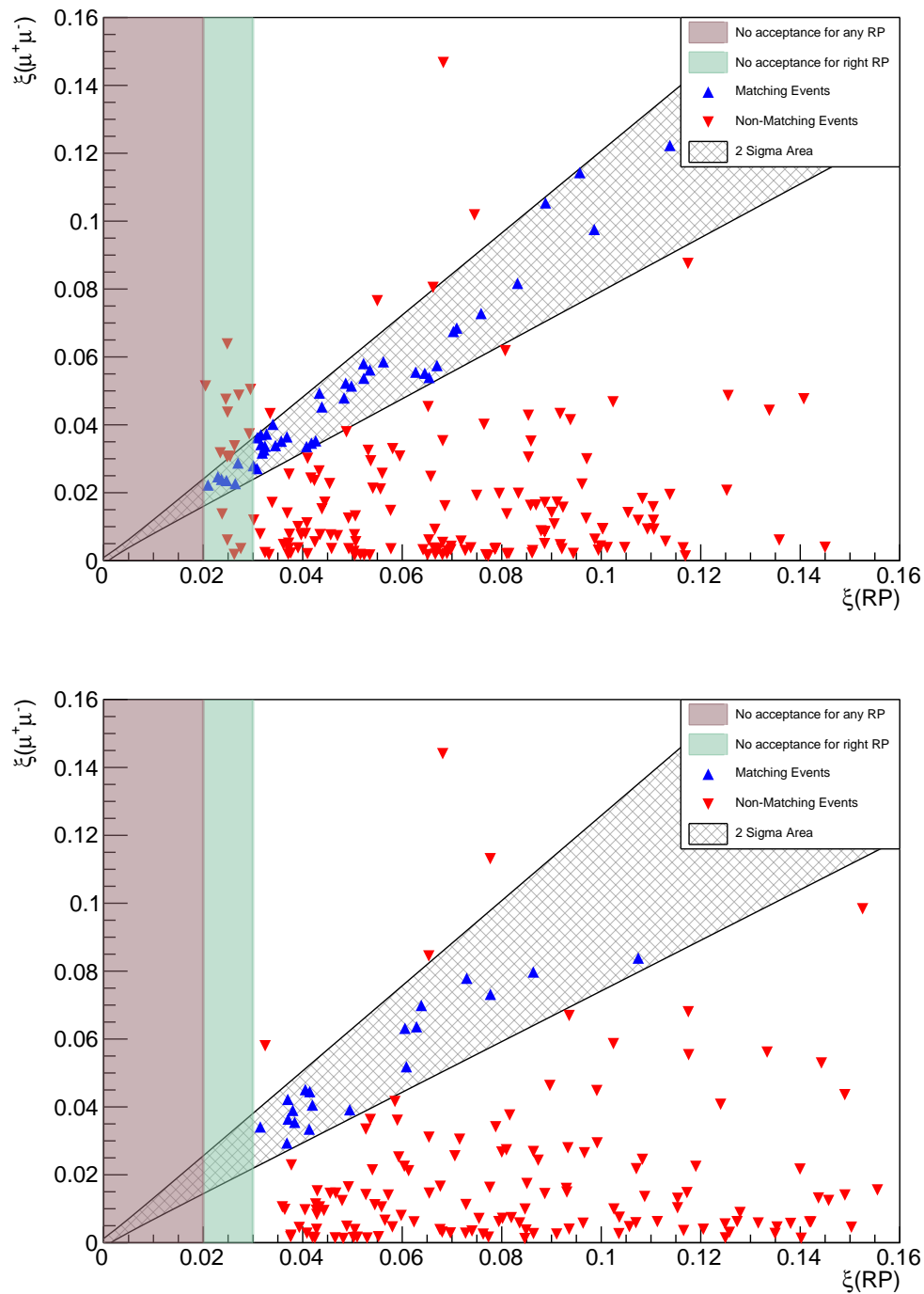
Legend: $\sigma(\xi_{RP})$ versus ξ_{RP} for single- and multi-RP protons in sector 45 (top) and sector 56 (bottom).

Source: The author, 2020.

Figure 33 - $\xi_{\ell^+\ell^-}$ resolution.

Legend: $\sigma(\xi_{\ell^+\ell^-})$ versus $\xi_{\ell^+\ell^-}$ for events with protons scattering to the negative z direction (top) and positive z direction (bottom).

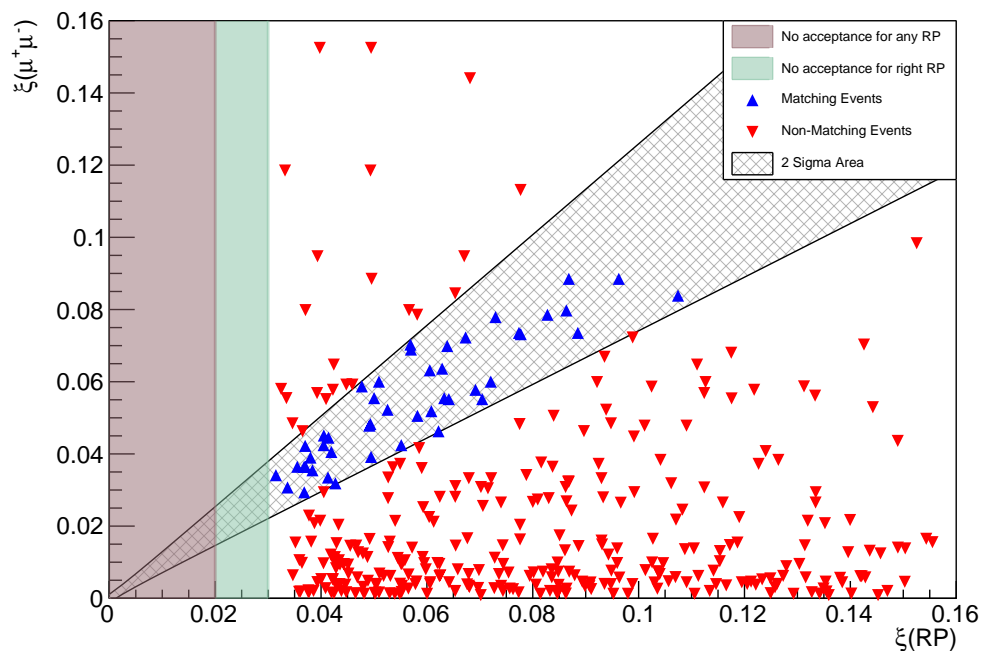
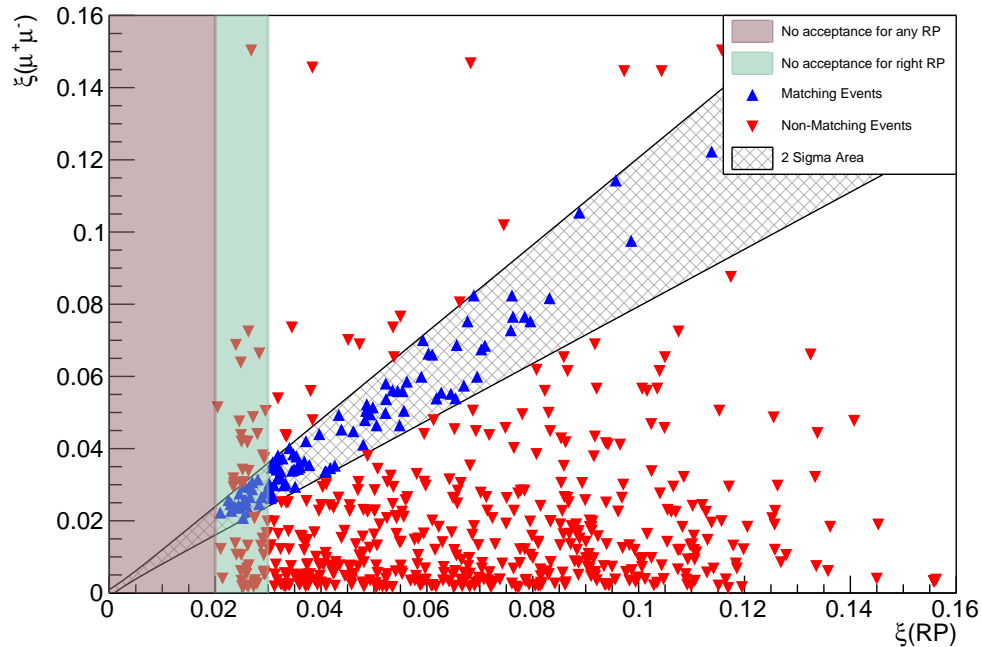
Source: The author, 2020.

Figure 34 - $\xi_{\ell^+\ell^-}$ versus ξ_{RP} correlation (single-RP) in events with only one proton.

Legend: $\xi_{\ell^+\ell^-}$ versus ξ_{RP} distributions with protons in sector 45 (top) and sector 56 (bottom), when requiring only one proton in the corresponding PPS detector. Protons are reconstructed with the single-RP method. The signal region is shown as the hatched band. The matching events are marked in blue, while the non-matching events are marked in red. The purple and green areas represent the out-of-acceptance kinematical region for any RP and for the right RP, respectively.

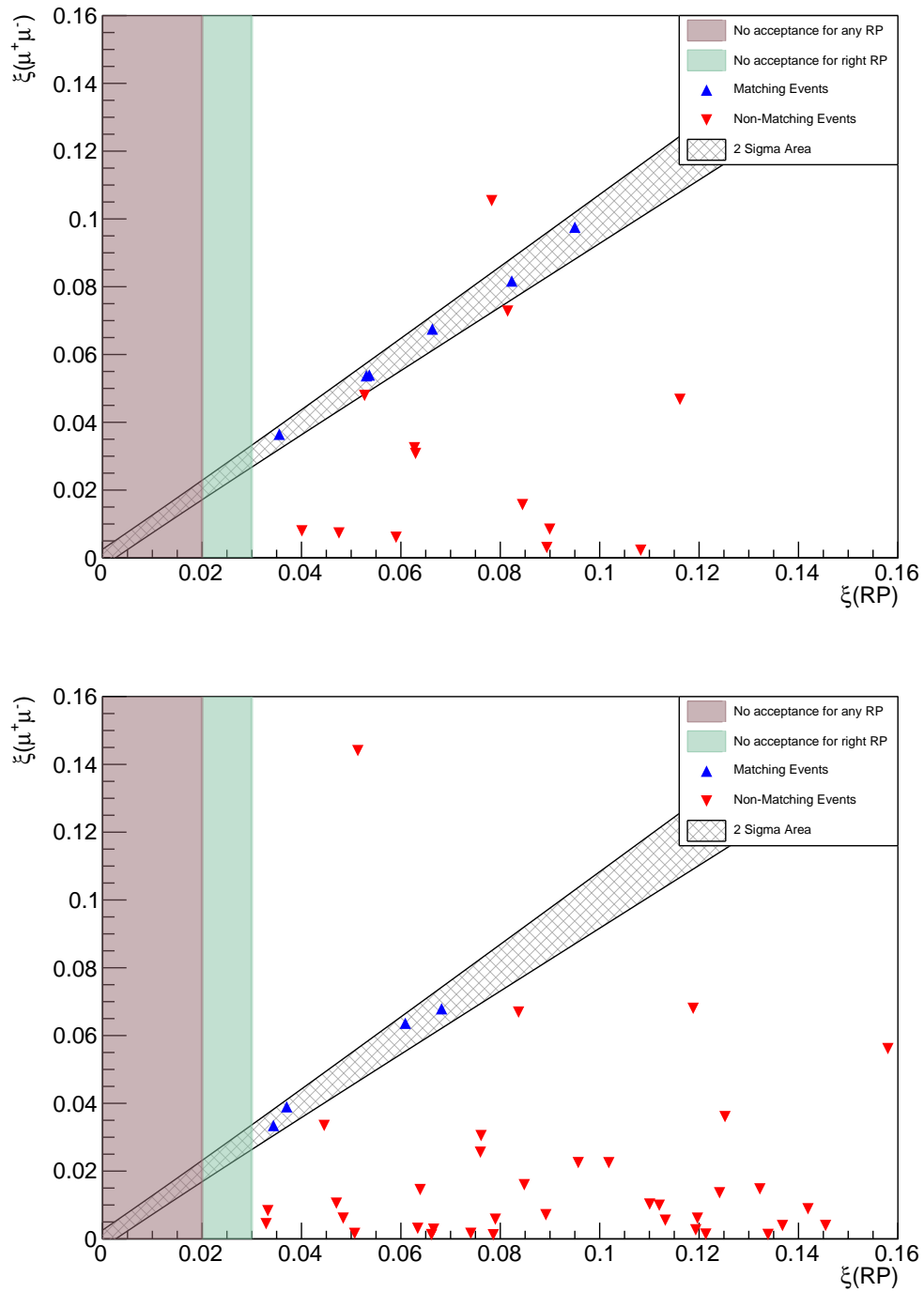
Source: The author, 2020.

Figure 35 - $\xi_{\ell^+\ell^-}$ versus ξ_{RP} correlation (single-RP) when no selection is applied on the number of protons.



Legend: $\xi_{\ell^+\ell^-}$ versus ξ_{RP} distributions with protons in sector 45 (top) and sector 56 (bottom), when no restriction is applied in the number of protons in the PPS detectors. Protons are reconstructed with the single-RP method. The signal region is shown as the hatched band. The matching events are marked in blue, while the non-matching events are marked in red. The purple and green areas represent the out-of-acceptance kinematical region for any RP and for the right RP, respectively.

Source: The author, 2020.

Figure 36 - $\xi_{\ell^+\ell^-}$ versus ξ_{RP} correlation (multi-RP).

Legend: $\xi_{\ell^+\ell^-}$ versus ξ_{RP} distributions with protons in sector 45 (top) and sector 56 (bottom), with protons reconstructed with the multi-RP method. The signal region is shown as the hatched band. The matching events are marked in blue, while the non-matching events are marked in red. The purple and green areas represent the out-of-acceptance kinematical region for any RP and for the right RP, respectively.

Source: The author, 2020.

- **Multitracking:** Due to the inability of the strip RPs to disambiguate multiple tracks in the same event.
- **Radiation damage:** The strip sensors are not designed to be exposed to high radiation doses and, while the pixel sensors are irradiation resistant, the pixel ROCs are not optimized for non-uniform radiation. This loss in efficiency needs to be taken in account in the analysis of the collected data.

In addition, a set of fiducial cuts is applied in order to restrict the analysis to a detector region with large acceptance. The lower limit of the fiducial cuts is dictated by the study of edge effects of the sensors, while the upper cut is derived from LHC collimator aperture studies. The values for x_{\min} , x_{\max} , y_{\min} , y_{\max} for the pixel RPs for each 2017 era are listed in Table 9.

The muon efficiency and resolution scale factors are described in section 2.2.3.2.

Everything cited above was applied following the Muon and Proton POG recommendations (CMS COLLABORATION, 2019); (CMS COLLABORATION, 2020), respectively.

4.6.4 Distributions in signal region

Figure 37 shows the muon pair invariant mass, p_T and η distributions for events with single-RP protons in sector 45 (220F) and Figure 38 for events with protons in sector 56 (220F).

The ξ distributions in the signal region are shown in Figures 39, 40 and 41 for single- and multi-RP protons. The signal MC distributions are not shown in the multi-RP case since not all correction factors are currently available.

The horizontal and vertical components of the scattering angle in the signal region are shown in figures 42 and 43.

4.7 Results

The numbers of data and MC signal and background events expected with protons reconstructed with the single- and multi-RP methods are shown in Tables 10, 11 and 12 with the respective statistical uncertainty.

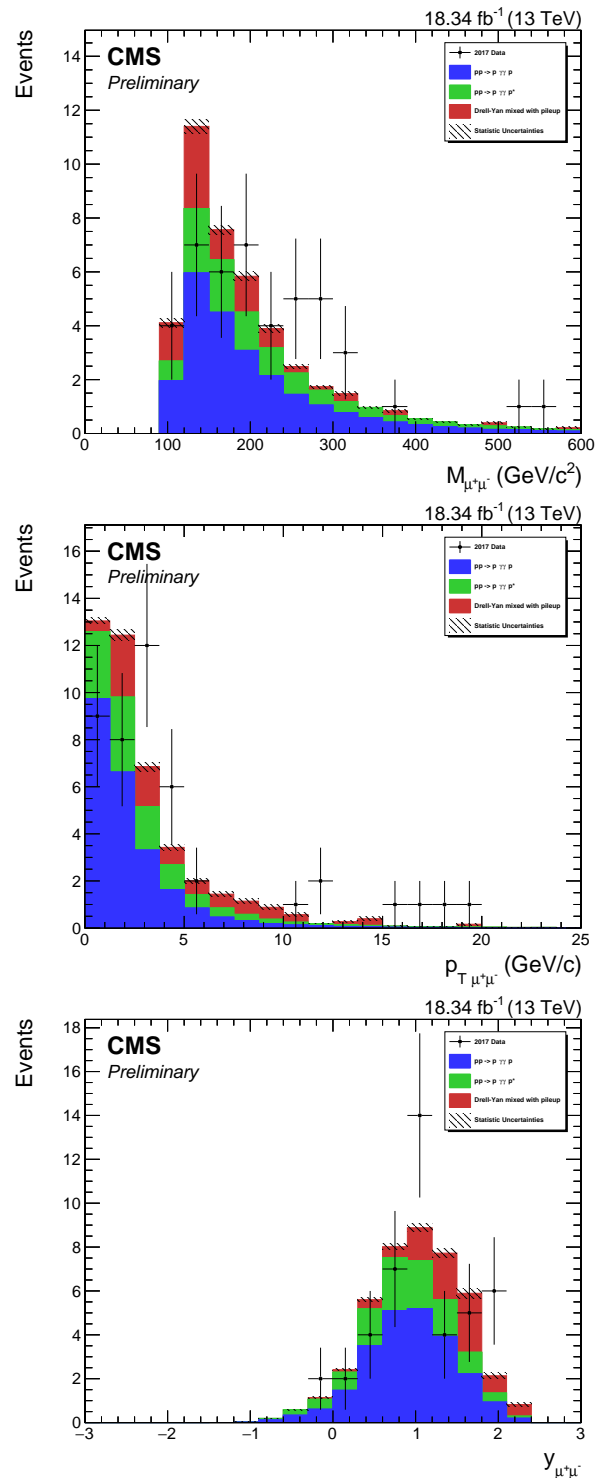
Table 9 - Fiducial cuts.

Era	45-220F	x_{\min} (mm)	45-220F	x_{\max} (mm)	45-220F	y_{\min} (mm)	45-220F	y_{\max} (mm)
2017B	1.995		24.479		-11.098		4.298	
2017C1	1.860		24.334		-11.098		4.298	
2017E	1.995		24.479		-10.098		4.998	
2017F1	1.995		24.479		-10.098		4.998	
Era	56-220F	x_{\min} (mm)	56-220F	x_{\max} (mm)	56-220F	y_{\min} (mm)	56-220F	y_{\max} (mm)
2017B	2.422		24.620		-10.698		4.698	
2017C1	2.422		24.620		-10.698		4.698	
2017E	2.422		24.620		-9.698		5.498	
2017F1	2.422		24.620		-9.798		5.398	

Legend: Fiducial cuts for the 2017 data for the detector station in sector 45 (top rows) and in sector 56 (bottom rows).

Source: The author, 2020.

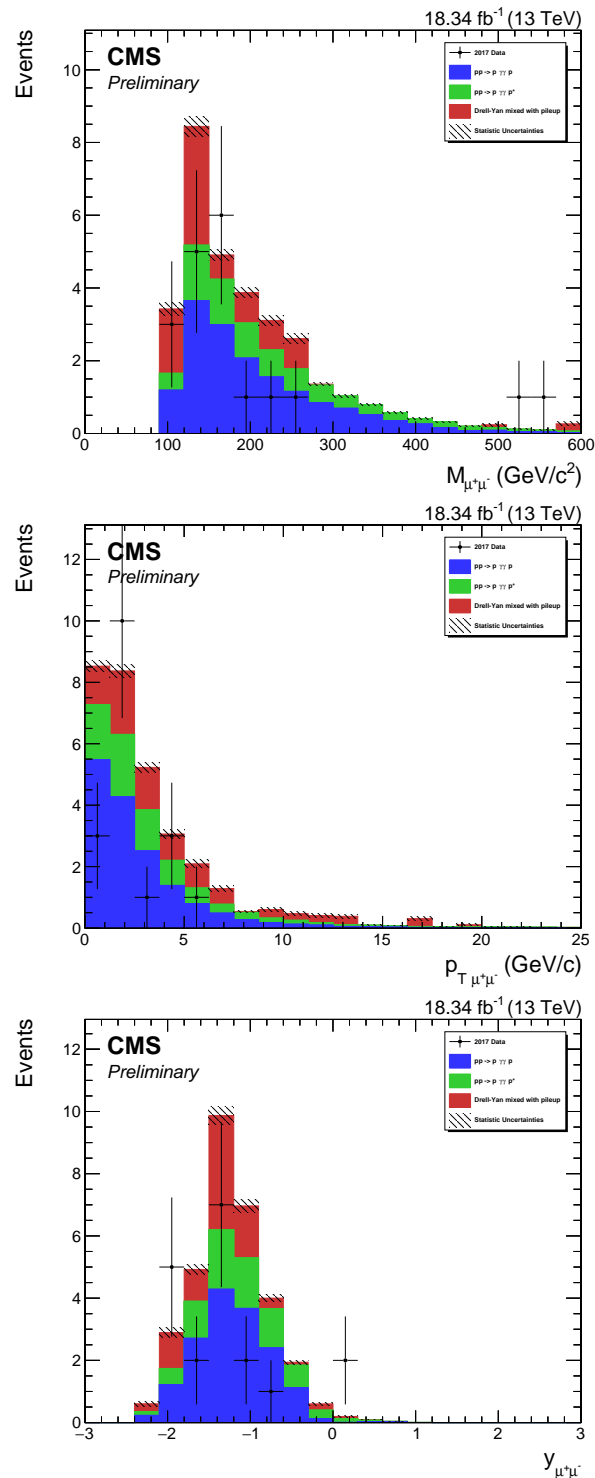
Figure 37 - Muon pair kinematic distributions in signal region for data and MC, for protons detected in sector 45 (220F).



Legend: Comparison between data (black dots), exclusive (green histograms), semi-exclusive (blue histograms) simulated samples, and DY simulated sample mixed with pileup (red histograms). Top: muon pair invariant mass. Middle: muon pair p_T . Bottom: muon pair rapidity. The hatched bands indicate the MC statistical uncertainty.

Source: The author, 2020.

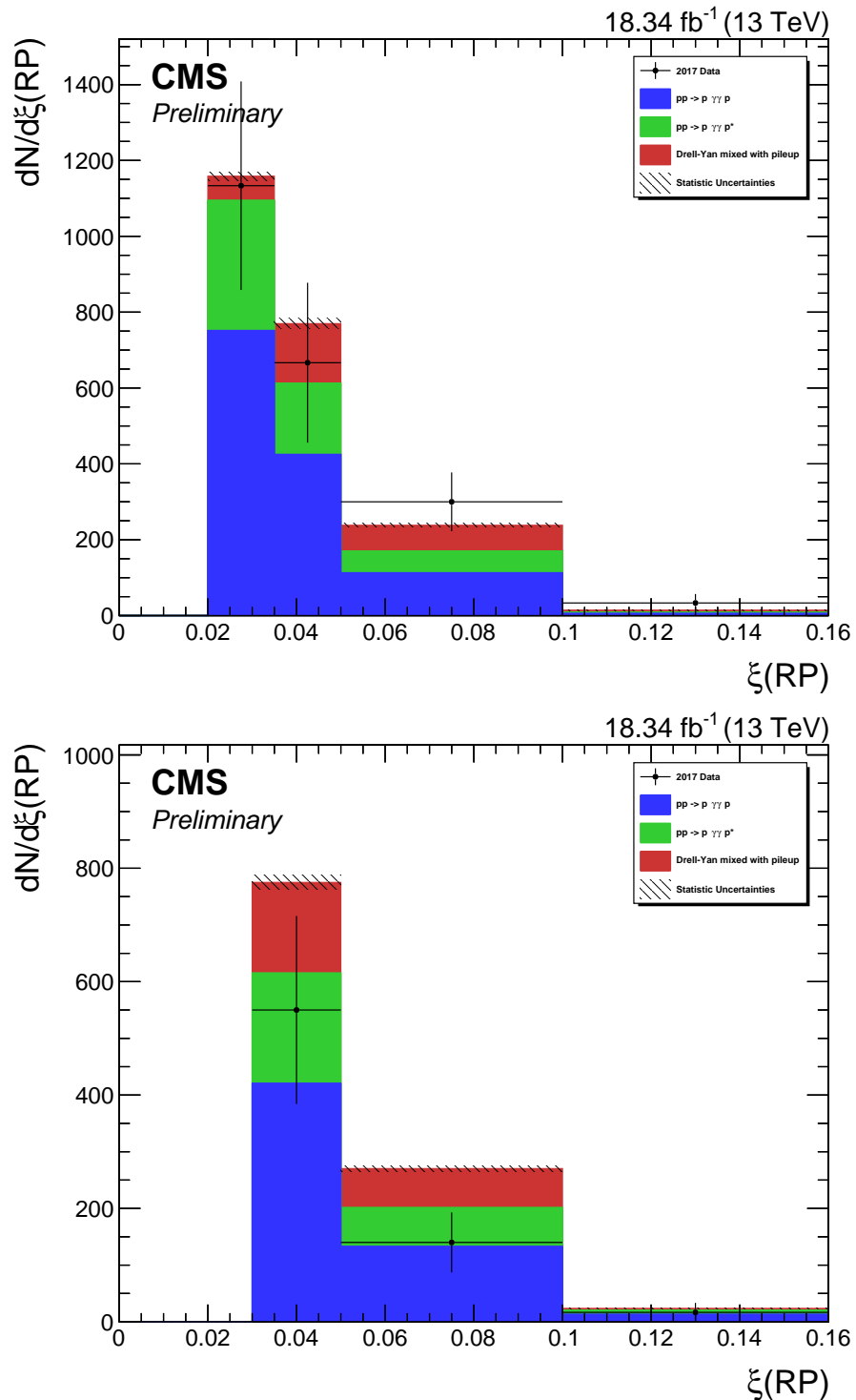
Figure 38 - Muon pair kinematic distributions in signal region for data and MC, for protons detected in sector 56 (220F).



Legend: Comparison between data (black dots), exclusive (green histograms), semi-exclusive (blue histograms) simulated samples, and DY simulated sample mixed with pileup (red histograms). Top: muon pair invariant mass. Middle: muon pair p_T . Bottom: muon pair rapidity. The hatched bands indicate the MC statistical uncertainty.

Source: The author, 2020.

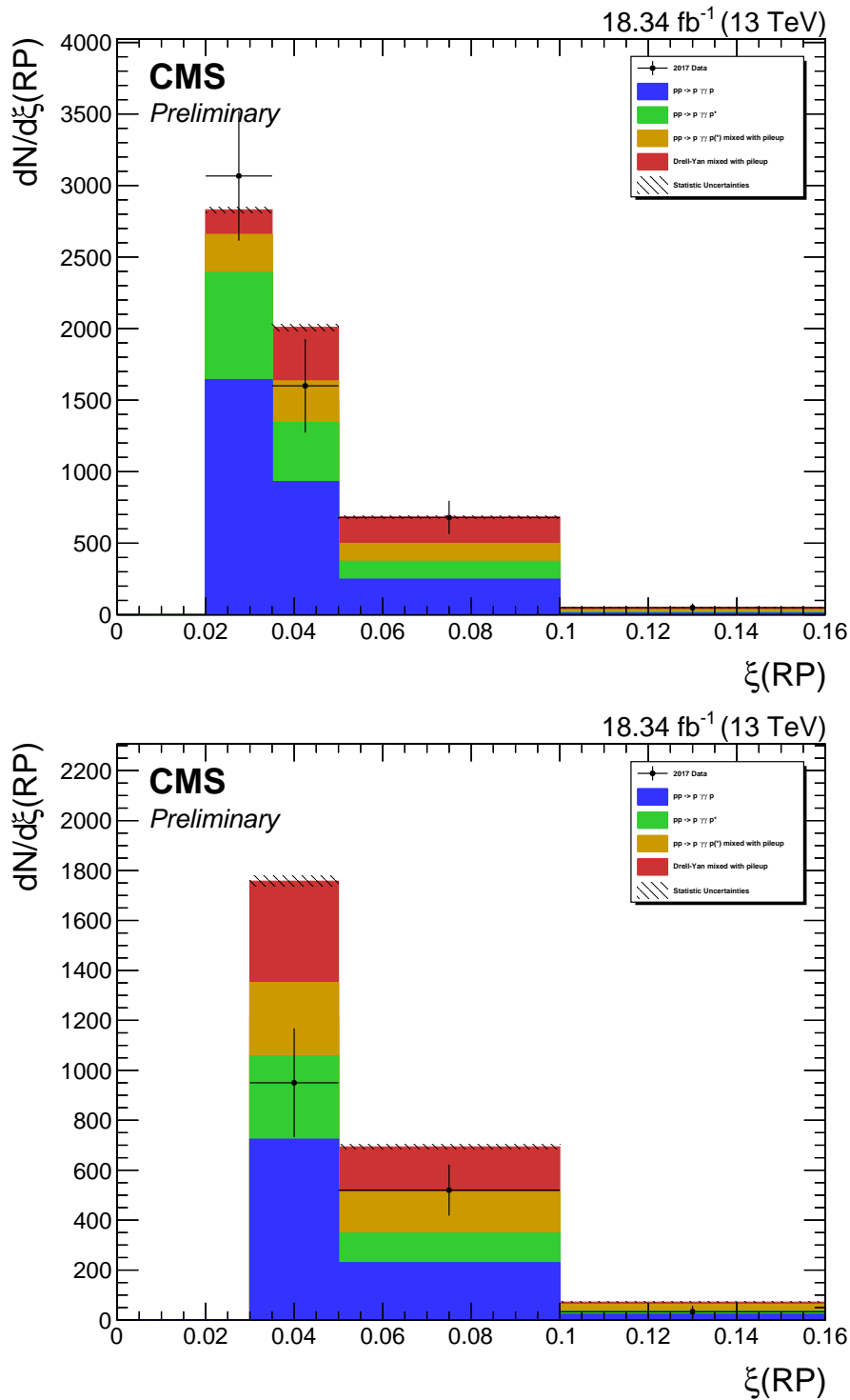
Figure 39 - ξ distributions in signal region for single-RP protons, in events with a single proton detected.



Legend: ξ_{RP} distributions in the signal region in sector 45 (top) and sector 56 (bottom). The data are indicated by black dots, exclusive muon pair simulated events by the green histograms and semi-exclusive simulated events by the blue histograms. The DY background mixed with pileup is indicated by the red histograms. The hatched bands indicate the MC statistical uncertainty.

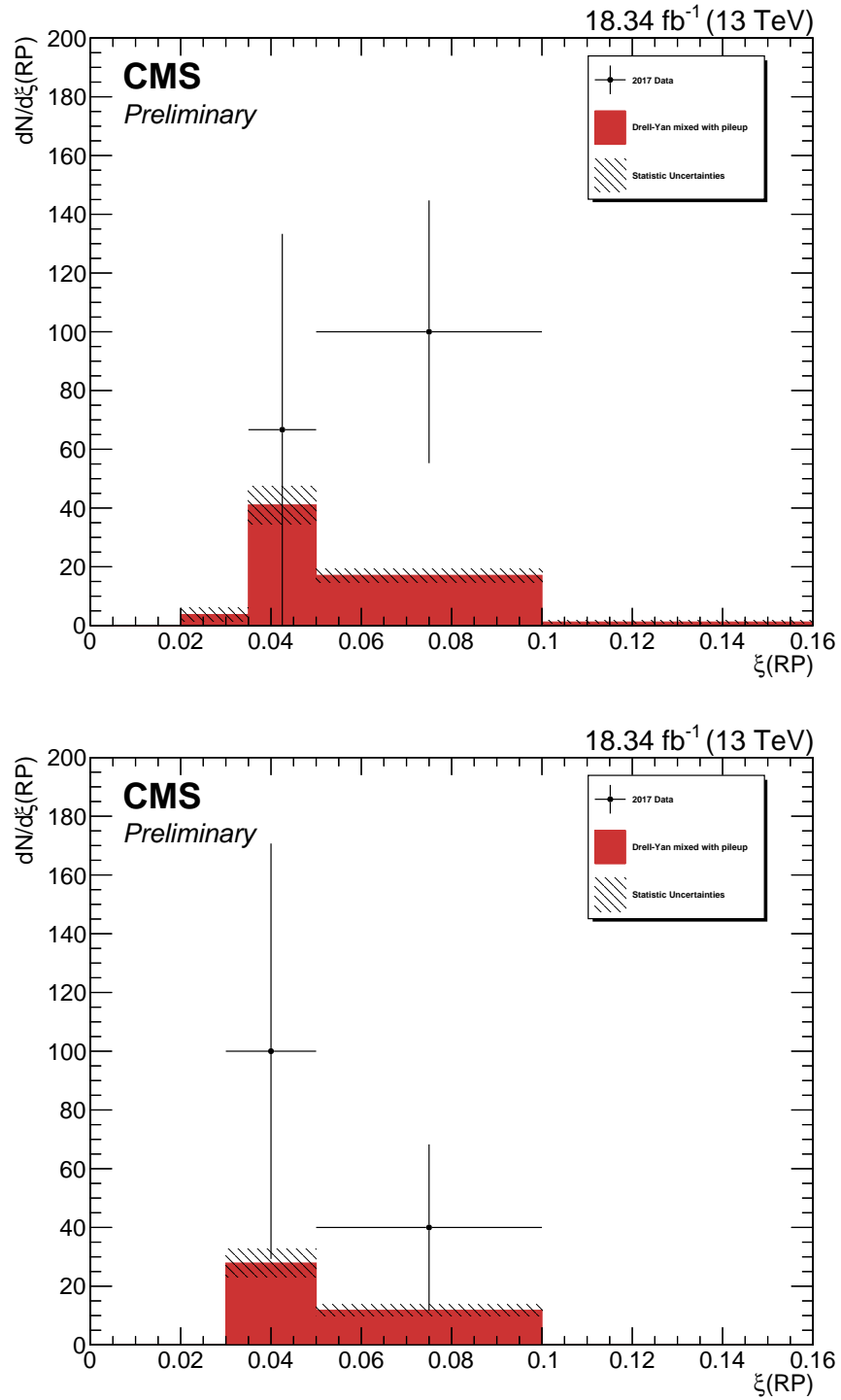
Source: The author, 2020.

Figure 40 - ξ distributions in signal region for single-RP protons, in events without restrictions on the number of protons.



Legend: ξ_{RP} distributions in the signal region in sector 45 (top) and sector 56 (bottom). The data are indicated by black dots, exclusive muon pair events by the green histograms and semi-exclusive events by the blue histograms. The signal MC mixed with pileup is indicated by the orange histograms. The DY background mixed with pileup is indicated by the red histograms. The hatched bands indicate the MC statistical uncertainty.

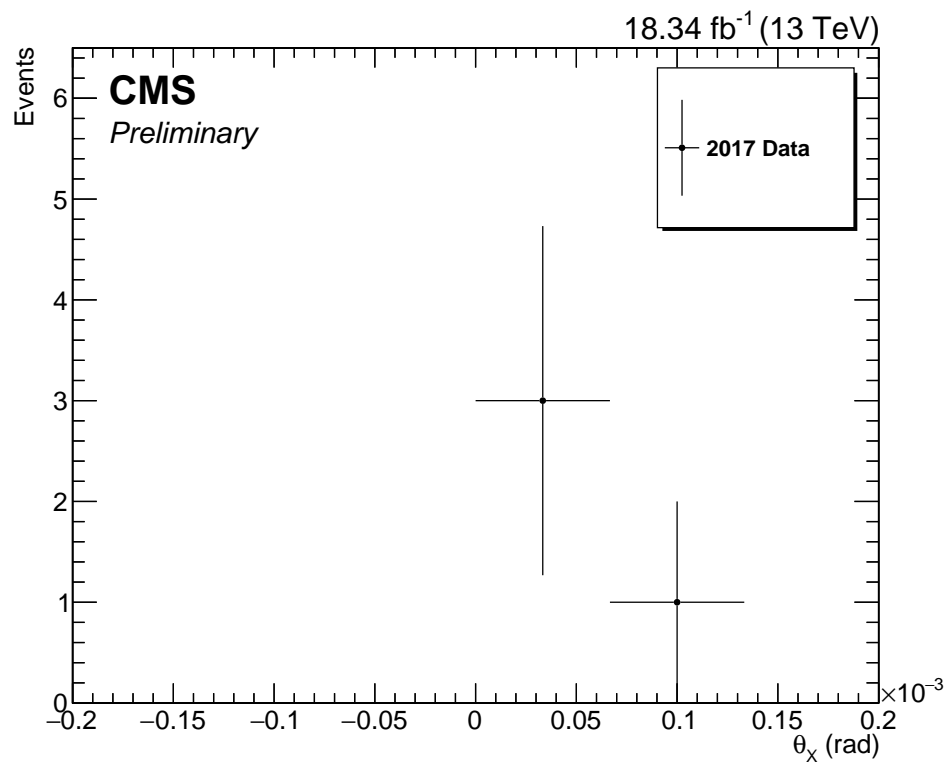
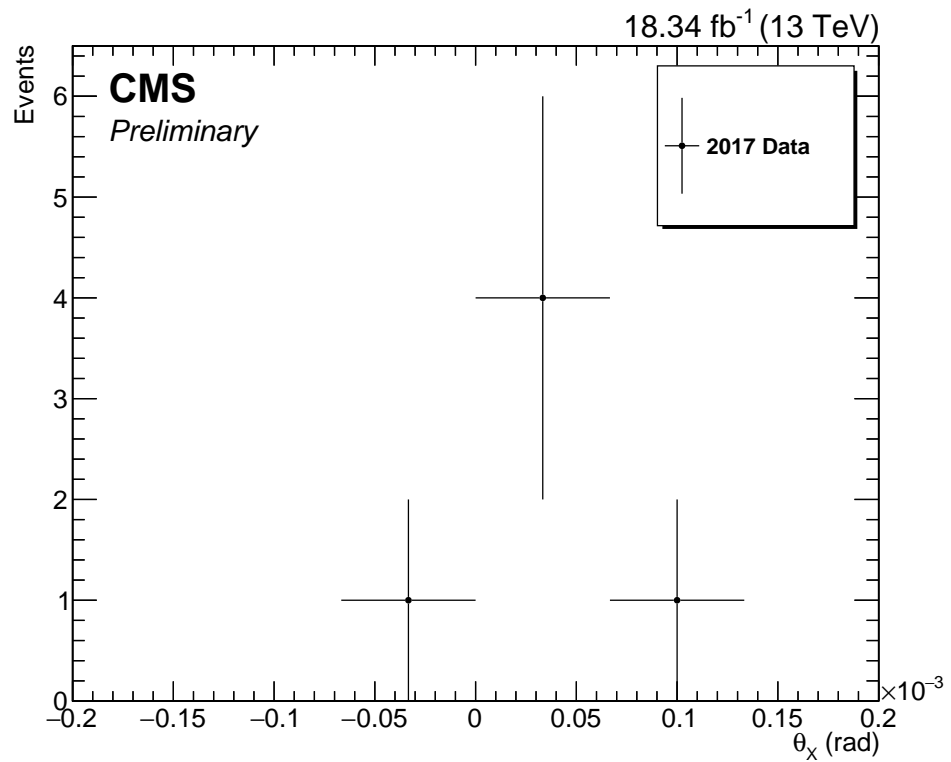
Source: The author, 2020.

Figure 41 - ξ distributions in signal region for multi-RP protons.

Legend: ξ_{RP} distributions in the signal region for multi-RP protons in sector 45 (top) and sector 56 (bottom). The data are indicated by black dots and the red histograms indicate the mixture of the DY simulation with pileup. The hatched bands indicate the statistical uncertainty of the DY simulation mixed with pileup.

Source: The author, 2020.

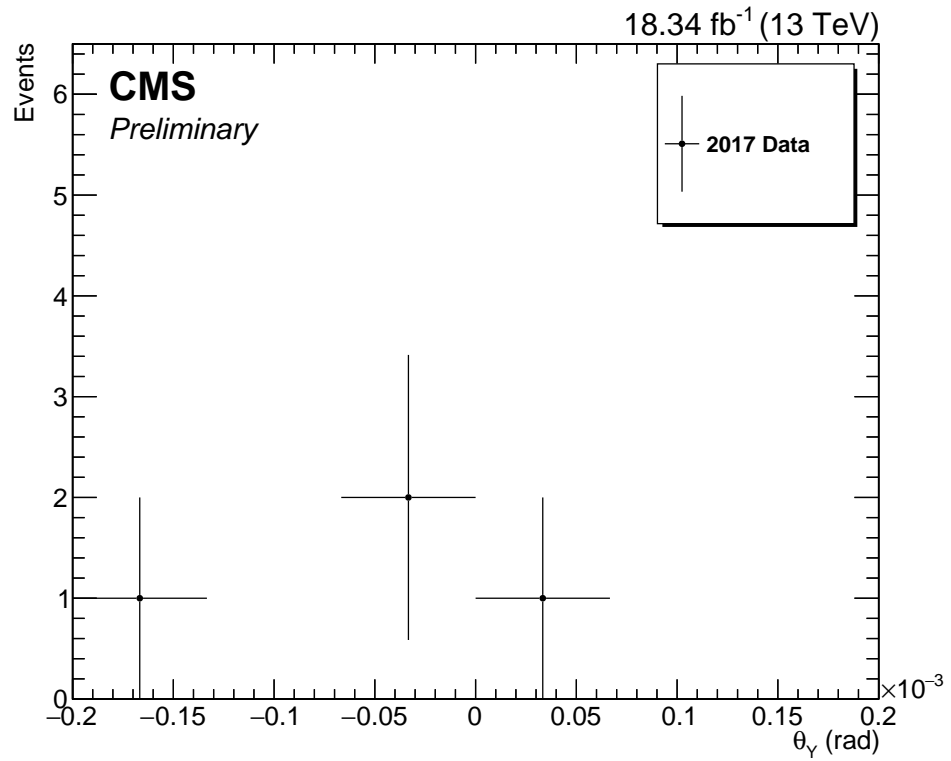
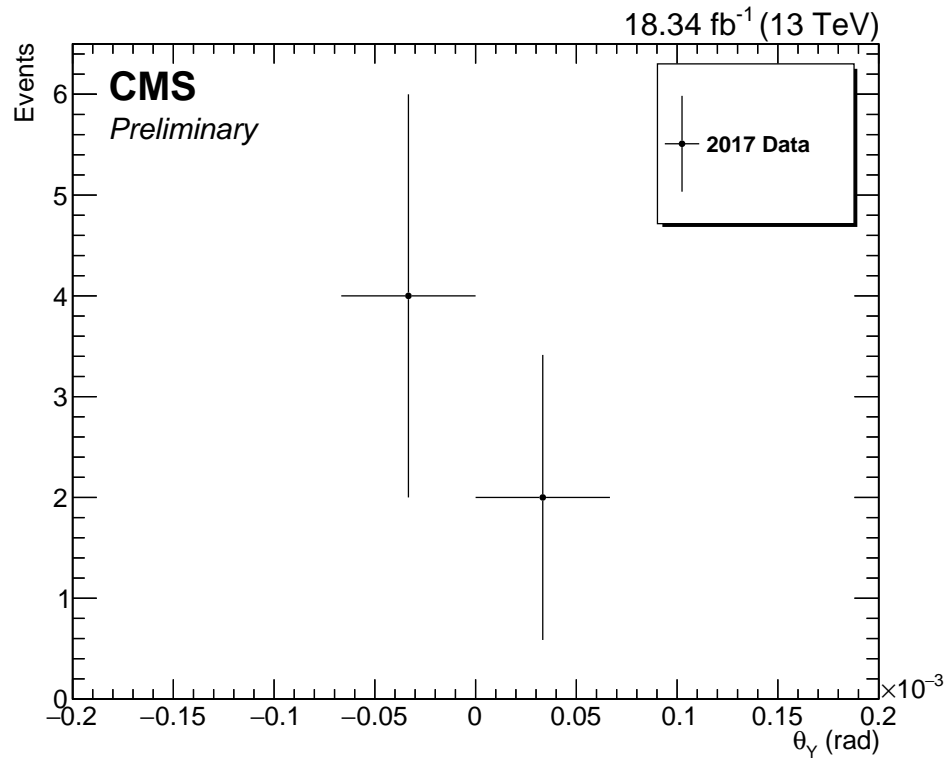
Figure 42 - Horizontal component of the scattering angle in signal region for multi-RP protons.



Legend: Horizontal component of the scattering angle in signal region for multi-RP protons in sector 45 (top) and sector 56 (bottom). The data are indicated by black dots.

Source: The author, 2020.

Figure 43 - Vertical component of the scattering angle in signal region for multi-RP protons.



Legend: Vertical component of the scattering angle in signal region for multi-RP protons in sector 45 (top) and sector 56 (bottom). The data are indicated by black dots.

Source: The author, 2020.

Table 10 - Number of events in signal region for the single-RP case, in events with a single proton detected.

Single-RP	2017 Data	pp \rightarrow p $\gamma\gamma$ p	pp \rightarrow p $\gamma\gamma$ p*	Drell-Yan mixed with pileup
45-220F	44.00 \pm 6.63	23.85 \pm 0.13	11.15 \pm 0.10	7.07 \pm 0.33
56-220F	19.00 \pm 4.36	15.97 \pm 0.12	7.87 \pm 0.10	6.88 \pm 0.33

Legend: Number of data events in the signal region, estimated number of exclusive and semi-exclusive events, and estimated background from DY events mixed with pileup for the single-RP case, in events with a single proton detected.

Source: The author, 2020.

Table 11 - Number of events in signal region for the single-RP case, in events without restrictions on the number of protons.

Single-RP	2017 Data	pp \rightarrow p $\gamma\gamma$ p	pp \rightarrow p $\gamma\gamma$ p*	Drell-Yan mixed with pileup	Signal MC mixed with pileup
45-220F	107.00 \pm 10.34	51.66 \pm 0.28	24.14 \pm 0.22	18.51 \pm 0.54	7.85 \pm 0.11
56-220F	47.00 \pm 6.86	27.25 \pm 0.21	13.42 \pm 0.16	17.76 \pm 0.54	7.99 \pm 0.11

Legend: Number of data events in the signal region, estimated number of exclusive and semi-exclusive events, and estimated background from DY events mixed with pileup and from signal MC events mixed with pileup for the single-RP case, in events without restrictions on the number of protons.

Source: The author, 2020.

Table 12 - Number of events in signal region for multi-RP.

Multi-RP	2017 Data	pp \rightarrow p $\gamma\gamma$ p	pp \rightarrow p $\gamma\gamma$ p	p $\gamma\gamma$ p*	Drell-Yan mixed with pileup
Left	6.00 ± 2.45	-	-	-	1.61 ± 0.16
Right	4.00 ± 2.00	-	-	-	1.16 ± 0.14

Legend: Number of data events in the signal region, estimated number of exclusive and semi-exclusive events, and estimated background from DY events mixed with pileup for the multi-RP case. The estimated number of exclusive and semi-exclusive events are not shown.

Source: The author, 2020.

For the tables and histograms, the comparison between data and simulation is not ideal. This is occurring for some reasons, but mainly because of the missing contributions on the efficiency corrections.

Another important factor is that only half of 2017 Data was used in this analysis, decreasing the overall statistics. Also, the double dissociation simulation (approximately 9.3% of the total background contribution) not being used helps even more on the discrepancy.

CONCLUSION

A study of lepton pair central (semi)exclusive production by photon-photon fusion using the PPS detector system with the CMS experiment, using data from 2017 period and corresponding to an integrated luminosity of 18.34 fb^{-1} was presented. In the present study, only muons were considered in the central lepton pair system.

This study confirmed the feasibility of the usage of a near-beam spectrometer at a high-luminosity hadron collider on a regular basis. The study updates the 2016 data analysis presented in (CMS AND TOTEM COLLABORATIONS, 2018) with the larger 2017 dataset, featuring for the first time the 3D pixel detectors installed as part of the PPS system.

In addition to the muon channel, we aim to analyze events with a pair of final state electrons, as in (CMS AND TOTEM COLLABORATIONS, 2018). The simulated background contribution due to double-dissociation, in combination with protons from pileup, and the systematic errors, will also be included.

The methodology developed in this study will be useful for future analyses of measurements of high-mass states and searches for anomalous couplings and new physics with tagged protons, as in (THIEL, 2019). In such future analyses, we aim to use machine learning tools to enhance the classification power of central exclusive or semi-exclusive processes.

REFERENCES

- ABBIENDI, G. The CMS muon system in Run2: preparation, status and first results. **Proceedings of Science**, Vienna, EPS-HEP2015, p. 237, 2015.
- AGOSTINELLI, S. et al. Geant4—a simulation toolkit. **Nuclear Instruments and Methods in Physics Research Section A: Accelerators, Spectrometers, Detectors and Associated Equipment**, Amsterdam, v. 506, n. 3, p. 250 – 303, 2003. ISSN 0168-9002. Available at: <http://www.sciencedirect.com/science/article/pii/S0168900203013688>. Access on: 16 dez. 2019.
- AKER, M. et al. Improved Upper Limit on the Neutrino Mass from a Direct Kinematic Method by KATRIN. **Physical Review Letters**, Maryland, v. 123, p. 221802, 2019.
- ALICE COLLABORATION. The ALICE experiment at the CERN LHC. **Journal of Instrumentation**, London, v. 3, n. 08, p. S08002–S08002, 2008. Available at: <https://doi.org/10.1088%2F1748-0221%2F3%2F08%2Fs08002>. Access on: 10 dez. 2019.
- ALWALL, J. et al. MadGraph 5 : Going Beyond. **Journal of High Energy Physics**, Berlin, v. 06, p. 128, 2011.
- ATLAS COLLABORATION. The ATLAS experiment at the CERN Large Hadron Collider. **Journal of Instrumentation**, London, v. 3, n. 08, p. S08003–S08003, 2008. Available at: <https://doi.org/10.1088%2F1748-0221%2F3%2F08%2Fs08003>. Access on: 10 dez. 2019.
- ATLAS COLLABORATION. Observation of a new particle in the search for the Standard Model Higgs boson with the ATLAS detector at the LHC. **Physics Letters B**, Amsterdam, v. 716, n. 1, p. 1 – 29, 2012. ISSN 0370-2693. Available at: <http://www.sciencedirect.com/science/article/pii/S037026931200857X>. Access on: 12 dez. 2019.
- ATLAS COLLABORATION. Measurement of exclusive $\gamma\gamma \rightarrow W^+W^-$ production and search for exclusive Higgs boson production in pp collisions at $\sqrt{s} = 8$ TeV using the ATLAS detector. **Physical Review**, Maryland, D94, n. 3, p. 032011, 2016.
- ATLAS COLLABORATION. Measurement of the exclusive $\gamma\gamma \rightarrow \mu^+\mu^-$ process in proton-proton collisions at $\sqrt{s} = 13$ TeV with the ATLAS detector. **Physics Letters**, Amsterdam, B777, p. 303–323, 2018.
- BAHR, M. et al. Herwig++ Physics and Manual. **European Physical Journal**, Berlin, C58, p. 639–707, 2008.
- BARANOV, S. P. et al. LPAIR: A generator for lepton pair production. In: **HERA. Workshop on Physics at HERA Hamburg, Germany, October 29-30, 1991**. Hamburg, 1991. p. 1478–1482.
- BECHTEL, F. **The underlying event in proton-proton collisions**. 2009. Tese (Doutorado em Física) — Hamburg University, Hamburg, 2009.

CHATRCHYAN, S. et al. Description and performance of track and primary-vertex reconstruction with the CMS tracker. **Journal of Instrumentation**, London, v. 9, n. 10, p. P10009, 2014.

CMS AND TOTEM COLLABORATIONS. **CMS-TOTEM Precision Proton Spectrometer**. Geneva, 2014. Available at: <https://cds.cern.ch/record/1753795>. Access on: 16 dez. 2019.

CMS AND TOTEM COLLABORATIONS. Observation of proton-tagged, central (semi)exclusive production of high-mass lepton pairs in pp collisions at 13 TeV with the CMS-TOTEM precision proton spectrometer. **Journal of High Energy Physics**, Berlin, v. 2018, n. 7, p. 153, 2018. ISSN 1029-8479. Available at: [https://doi.org/10.1007/JHEP07\(2018\)153](https://doi.org/10.1007/JHEP07(2018)153). Access on: 12 dez. 2019.

CMS COLLABORATION. **CMS Physics: Technical Design Report Volume 1: Detector Performance and Software**. Geneva, 2006. Available at: <https://cds.cern.ch/record/922757>. Access on: 16 dez. 2019.

CMS COLLABORATION. The CMS experiment at the CERN LHC. **Journal of Instrumentation**, London, v. 3, n. 08, p. S08004–S08004, 2008. Available at: <https://doi.org/10.1088%2F1748-0221%2F3%2F08%2Fs08004>. Access on: 10 dez. 2019.

CMS COLLABORATION. Exclusive $\gamma\gamma \rightarrow \mu^+\mu^-$ production in proton-proton collisions at $\sqrt{s} = 7$ tev. **Journal of High Energy Physics**, Berlin, v. 2012, p. 1–39, jan. 2012.

CMS COLLABORATION. Observation of a new boson at a mass of 125 GeV with the CMS experiment at the LHC. **Physics Letters B**, Amsterdam, v. 716, n. 1, p. 30 – 61, 2012. ISSN 0370-2693. Available at: <http://www.sciencedirect.com/science/article/pii/S0370269312008581>. Access on: 12 dez. 2019.

CMS COLLABORATION. Evidence for exclusive $\gamma\gamma \rightarrow W^+W^-$ production and constraints on anomalous quartic gauge couplings in pp collisions at $\sqrt{s} = 7$ and 8 TeV. **Journal of High Energy Physics**, Berlin, v. 08, p. 119, ago. 2016.

CMS COLLABORATION. Particle-flow reconstruction and global event description with the CMS detector. **Journal of Instrumentation**, London, v. 12, n. 10, p. P10003–P10003, 2017. Available at: <https://doi.org/10.1088%2F1748-0221%2F12%2F10%2Fp10003>. Access on: 16 dez. 2019.

CMS COLLABORATION. The CMS trigger system. **Journal of Instrumentation**, London, v. 12, n. 01, p. P01020–P01020, 2017. ISSN 1748-0221. Available at: <http://dx.doi.org/10.1088/1748-0221/12/01/P01020>. Access on: 16 dez. 2019.

CMS COLLABORATION. Performance of the CMS muon detector and muon reconstruction with proton-proton collisions at $\sqrt{s} = 13$ TeV. **Journal of Instrumentation**, London, v. 13, n. 06, p. P06015, 2018.

CMS COLLABORATION. **CMS Luminosity - Public Results**. 2019. Available at: <https://twiki.cern.ch/twiki/bin/view/CMSPublic/LumiPublicResults>. Access on: 16 dez. 2019.

- CMS COLLABORATION. **Efficiency of the Pixel sensors used in the Precision Proton Spectrometer: radiation damage.** Geneva, 2019. Available at: <http://cds.cern.ch/record/2697291>. Access on: 16 dez. 2019.
- CMS COLLABORATION. **Fill Reports.** 2019. Available at: <https://cmswbm.cern.ch/cmsdb/servlet/FillReport>. Access on: 16 dez. 2019.
- CMS COLLABORATION. **MiniAOD Analysis Documentation.** 2019. Available at: <http://twiki.cern.ch/twiki/bin/view/CMSPublic/WorkBookMiniAOD2017>. Access on: 18 dez. 2019.
- CMS COLLABORATION. **Reference Muon ID, Isolation and Trigger Efficiencies for 2017 Data.** 2019. Available at: <https://twiki.cern.ch/twiki/bin/view/CMS/MuonReferenceEffs2017>. Access on: 18 dez. 2019.
- CMS COLLABORATION. **Tagged protons: getting started.** 2020. Available at: <https://twiki.cern.ch/twiki/bin/viewauth/CMS/TaggedProtonsGettingStarted>. Access on: 18 dez. 2019.
- DAVIS, S. R. **Interactive Slice of the CMS detector.** 2016. Available at: <http://cds.cern.ch/record/2205172>. Access on: 16 dez. 2019.
- GREINER, W.; REINHARDT, J. **Quantum Electrodynamics.** Berlin: Springer, 2008. ISBN 9783540875611. Available at: <https://books.google.com.br/books?id=5Kd3dBL8a64C>. Access on: 10 dez. 2019.
- HALZEN, F.; MARTIN, A. **Quarks & Leptons: An Introductory Course in Modern Particle Physics.** New York: John Wiley & Sons, 1984.
- KASPAR, J. **Alignment of CT-PPS detectors in 2016, before TS2.** 2017. Available at: <http://cds.cern.ch/record/2256296>. Access on: 16 dez. 2019.
- LEFÈVRE, C. **The CERN accelerator complex. Complexe des accélérateurs du CERN.** 2008. Available at: <https://cds.cern.ch/record/1260465>. Access on: 16 dez. 2019.
- LHCB COLLABORATION. The LHCb detector at the LHC. **Journal of Instrumentation**, London, v. 3, n. 08, p. S08005–S08005, 2008. Available at: <https://doi.org/10.1088%2F1748-0221%2F3%2F08%2Fs08005>. Access on: 10 dez. 2019.
- MANS, J. et al. **CMS Technical Design Report for the Phase 1 Upgrade of the Hadron Calorimeter.** Geneva, 2012. Available at: <https://cds.cern.ch/record/1481837>. Access on: 16 dez. 2019.
- MARTIN, A. D.; KHOZE, V. A.; RYSKIN, M. G. Rapidity gap survival probability and total cross sections. In: HERA. **Proceedings, HERA and the LHC Workshop Series on the implications of HERA for LHC physics: 2006-2008.** Hamburg, 2008. p. 488–494.
- NEMES, F. **LHC optics determination with proton tracks measured in the CT-PPS detectors in 2016, before TS2.** 2017. Available at: <http://cds.cern.ch/record/2256433>. Access on: 16 dez. 2019.

- SAKUMA, T. **Cutaway diagrams of CMS detector**. 2019. Available at: <https://cds.cern.ch/record/2665537>. Access on: 16 dez. 2019.
- SALAM, A. Weak and Electromagnetic Interactions. **Conference Proceedings C**, Lerum, v. 680519, p. 367–377, 1968.
- SJOSTRAND, T.; MRENNNA, S.; SKANDS, P. Z. A Brief Introduction to PYTHIA 8.1. **Computer Physics Communications**, Amsterdam, v. 178, p. 852–867, 2008.
- SOUZA, S. F. **Development and Integration of the CT-PPS Fast Simulation in the CMS Software**. Geneva, 2017. Available at: <https://cds.cern.ch/record/2289246>. Access on: 16 dez. 2019.
- TANABASHI, M. et al. Review of Particle Physics. **Physical Review**, Maryland, D98, n. 3, p. 030001, 2018.
- TELES, P. R. **Searches for New Physics in the Standard Model’s Electroweak Sector: Quartic Anomalous Couplings with Vector Boson Fusion and Flavor Changed Neutral Current in the $SU(3)_C \otimes SU(3)_L \otimes U(1)_X$ model**. 2013. 146 p. Tese (Doutorado em Física) — Universidade Federal do ABC, São Paulo, 2013.
- THIEL, M. **Study of WW Central Exclusive Production in the semileptonic channel with tagged protons at CMS detector**. 2019. 108 p. Tese (Doutorado em Física) — Universidade do Estado do Rio de Janeiro, Rio de Janeiro, 2019.
- TOTEM COLLABORATION. LHC Optics Measurement with Proton Tracks Detected by the Roman Pots of the TOTEM Experiment. **New Journal of Physics**, London, v. 16, n. CERN-PH-EP-2014-066. CERN-PH-EP-2014-066, p. 103041. 20 p, 2014. Available at: <http://cds.cern.ch/record/1693528>. Access on: 16 dez. 2019.